UNIVERSITÉ DU LUXEMBOURG

PhD-FSTM-2022-104
The Faculty of Science, Technology and Medicine

DISSERTATION

Defence held on 09/09/2022 in Esch-Sur-Alzette

to obtain the degree of

DOCTEUR DE L'UNIVERSITÉ DU LUXEMBOURG

EN PHYSIQUE

by

Nikhar KHANNA
Born on 13 February 1994 in Dehradun, (India)

METAMATERIAL DESIGN AND ELABORATIVE APPROACH FOR EFFICIENT SELECTIVE SOLAR ABSORBER

Dissertation defence committee

Dr Emanuele BARBORINI, dissertation superviser
PhD, Luxembourg Institute of Science and Technology

Dr Mohamed EL HACHEMI,
PhD, Luxembourg Institute of Science and Technology

Prof. Dr Andreas MICHELS, Chairman
Professor, Université du Luxembourg

Prof. Nicholas FANTUZZI
Professor, University of Bologna, Italy

Prof. Ali DAOUADJI, Vice Chairman
Professor, Institut National des Sciences Appliquées, Lyon, France

Under the supervision of Dr. Mohamed El Hachemi and Dr. Emanuele Barborini

Acknowledgments

A lot of people have supported my efforts to complete this PhD thesis, and hence I take this opportunity to thank all those without whom this project would not have been possible. I would like to begin with thanking my PhD supervisor Dr. Emanuele Barborini for his exceptional guidance throughout the thesis. His constant support and motivation drove me to where I am today. I cannot imagine this journey without his perfect supervision. I would then like to express my heartfelt gratitude towards Dr. Mohamed El. Hachemi, my CET member, for having given me the opportunity to work in this project at MRT department of LIST. Throughout my research, he has been my pillar of strength. He is a man with infinite perseverance, and I walked into his office countless times without the fear of being judged. He made sure that he was available for me at all times. I not only benefited from his wealth of knowledge but also felt appreciated even when I knew I had made blunders. He has always been extremely supportive of my life outside my professional world too. Taking care if I am taking regular time off and not stressed with work, and at the same time advising me to visit the only the safe areas in Luxembourg by literally pointing google maps. I thank him for believing in me in every aspect of this journey. If I ever look forward to being like someone, that would be him.

Next, I would like to thank the jury members, Prof Nicholas Fantuzzi and Prof. Dr. Ali Daouadji, for accepting to review and evaluate my thesis work and participating in my defense. Prof. Dr Andreas Michels, thank you for being a part of my CET.

I would like to express my thanks to other people who were directly and indirectly involved with my project, for their steady inputs. Thank you Noureddine Adjeroud for helping me with thin film depositions, Marc Michel and Sivashankar Krishnamoorthy for advising me with the chemistry associated with the project, and later for always asking if I am doing well. Didier Arl and Petru Lunca Popa for assisting me with the optical characterizations, Torsten Granzow for electrical characterizations, Chistele Vergne and Jerome Guillot for XPS characterizations.

I would also like to express my appreciation to Prof. Dr. Suzzane Siebentritt for allowing me to work with the instruments associated with the University of Luxembourg. Thomas Weiss, Mohit Sood and Damilola Adeleye for lending a helping hand with the optical measurements. I would like to express my sincere gratitude to the team in Swansea University, UK for always being present and contributing to my project, and the team in Institute Lafayette, France for their collaboration and agreeing to take e-beam lithography challenge and making it possible with their expertise.

I acknowledge, the financial support FNR for funding this project.

Thanks to my present and former office mates for making this workplace cheerful and lively with your presence. Tai, Rishabh, Raoul, Marco, Anthony, Elisa, Antoine, Julian, Lauriane, I am much obliged that I had you all around during this journey of mine.

I would take this opportunity to express my gratitude to my amazing friends cum family in Luxembourg. Special thanks to Sangita and Ahilan for understanding me so

well. They were always there to lend an ear and a shoulder to lean on. Life without them would have never been the same here. I am grateful to Rutuja for holding up with me during the initial phase of my PhD, when I knew no one around. Gratitude to Mohit and Rutuja for being kind and co-operative flatmates and friends. My sincere thanks to them for taking care of me and the house while I was so ignorant. I am much obliged to Arpan, Shreyasi, Rohan, Sweta, Sachin, Richa, Darshit, Puneeth, Deb and Vita for always bringing a smile to my face. Aman, Rajan and Sudanshu, I appreciate their willingness to provide me with their advice and encouragement whenever it was needed. I am so grateful to Annu and Jaya, my box of treasure, they make my soul shine and heart spark. I acknowledge Vinay for proof-reading my thesis, and for those deep meaningful conversations over the video calls.

Its now time to respect my parents for believing in me and never stopping me to do anything in life. All their hard work and determination is the reason for who I am today. I adore my grandmother for always being so practical and modern. Without her prayers I would not have been where I am today. Love to my grandfather for blessing me from heaven. Special thanks to my brother and sister-in-law for encouraging me in all paths of life. They are my role-models and I am fortunate to have them both around. I fondly thank my partner in life, Akshay, for believing in my dreams. He has been my biggest cheerleader who never lets me stop believing in myself. Though we were never together during this journey but it was always so comforting knowing that he was there. Last but not the least I would like to thank God for throwing these opportunities on my way.

Abstract

The thesis is focused on developing spectral selective coatings (SSC) composed of multilayer cermets and periodic array of resonating omega structures, turning them to behave like metamaterials, while showing high thermal stability up to1000°C. The developed SSC is intended to be used for the concentrated solar power (CSP) applications. With the aim of achieving highest possible absorbance in the visible region of the spectrum and highest reflectance in the infrared region of the spectrum. The thesis highlights the numerical design, the synthesis and optical characterization of the SSC of approximately 500 nm thickness. A bottom-up approach was adopted for the preparation of a stack with alternate layers, consisting of a distribution of Titanium Nitride (TiN) nanoparticles with a layer of Aluminum Nitride (AlN) on top. The TiN nanoparticles, laid on a Silicon substrate by wet chemical method, are coated with conforming layer of AlN, via Plasma-enhanced Atomic Layer Deposition (PE-ALD). The control of the morphology at the nanoscale is fundamental for tuning the optical behaviour of the material. For this reason, two composites were prepared. One starting with TiN dispersion made with dry TiN powder and deionized water, and the other with ready-made TiN dispersion. Nano-structured metamaterial based absorbers have many benefits over conventional absorbers, such as miniaturisation, adaptability and frequency tuning. Dealing with the current challenges of producing the new metamaterial based absorber with optimal nanostructure design along with its synthesis within current nano-technological limits, we were capable of turning the cermets into metamaterial. A periodic array of metallic omega structures was patterned on top of both the composites I and II, by using e-beam lithography technique.

Parameters, such as the size of TiN nanoparticles, the thickness of AlN thin film and the dimensions of the omega structure were all revealed by the numerical simulations, performed using Wave-Optics module in COMSOL Multiphysics. The work showcased clearly compares the two kinds of composites, using scanning electron microscope, X-ray photoelectron spectroscopy(XPS) and electrical conductivity measurement. The improvement in the optical performance of the SSC after the inclusion of metallic omega structures in the uppermost layer of the two composites has been thoroughly investigated for light absorption boosting. In addition, the optical performance of the two prepared composites and the metamaterial is used as a means of validating the computational model.

Contents

List of Figures

List of Tables

Chapter 1

Introduction

1.1 Current trends in the field of Solar Concentrated Power

The connection between energy and mankind is running for over centuries now, where the availability of energy has changed the path of humanity in every possible way. Not only have advanced sources of energy been unfastened, first fossil fuel, then diversification to nuclear and hydro-power, and now renewable technologies- but also in the capacity we can supply and demand. Here in section 1.1 of the introduction, we concentrate on the total consumption and production of the global energy, and its share from the renewable energy. Also focusing in brief the proportion of energy from a sector of renewable sources especially Concentrated Solar Power (CSP). Whereas, later in this section of introduction we talk about understanding CSPs - the global use of CSPs, the installed and production capacity of energy from CSP systems, their advantages in the field of renewables, and the fields of operation they are currently lacking in.

Renewable energies comes from the sources that are constantly replenished. These sources of energy are wind energy, solar energy, geothermal energy, hydroelectric power and biomass. The declination on the dependence of fossil fuels for energy has made renewable energy an important topic of discussion. World's power needs in 1990 was about 1 billion gigawatts, which now has approached 10 billion gigawatts[5]. Talking of global energy consumption by fuel type, the demand of petroleum rose from 38% in 1950 to 45% in 1975, and then dropping to about 40% during energy crisis in 1970s. About 40% of the consumed energy in the United States is supplied by petroleum, and this proportion has been consistent since 1950. The global consumption of coal was 35% in 1950, a decade later it was declined to about 20%, and this proportion has remained constant since then. Considering natural gas, its consumption increased to almost 4 times in 2007 as it was in 1950. Nuclear power that became popular in the late 1960s supplied 9% of the total electricity generation, in the midst of the oil crisis. The nuclear share of power generation increased to 20% in 1990. Currently, the global energy consumption produced by the nuclear energy is around 8.5%, and is estimated to be the same for the next 20 years [6]. To date, renewable energy is an actively growing source in electricity generation. There

is an annual increase of 2.8% in the total generation from renewable resources, and the share of global electricity generation from renewables has been estimated to increase from 21% in 2010 to 25% in 2040. An important point to note is, about 80 percent of this increase is from hydroelectric and wind power, together, followed by biowaste and biomass energy (7%), geothermal energy (2%), and solar, tidal, and wave energy (less than 1%)[7]. By comparison, solar energy, currently, is much less significant, accounting for around less than 1% of global electricity generation. According to several scenarios modelled by International Energy Agency (IEA), one of the scenarios stated that the global demand for electricity rises by 79% between 2011 and 2050, with wind, hydro, and solar supplying 66% of global generation in 2050, where solar alone would be supplying 27%. This makes the solar electricity generation increase to more than 50 times its 2013 level by 2050[8]. Out of less than 1% production of electricity by solar energy, by the end of 2013, more than 97% of global solar generation capacity was photovoltaics (PV), producing 131,434 GW h of electricity, making solar PV the leading solar electric technology, and less than 3% was CSP producing 6,186 GWh of electricity[9].

Understanding CSPs, to begin with, CSP also refers to as solar thermal power that generates electricity by using the steam produced by heating the fluid. CSP systems utilizes mirrors to direct and focus solar radiations on the heat transfer fluid. This fluid that can be a synthetic oil, steam or molten salt, generates electricity either by direct expansion through the turbine or via heat that transfers a separate fluid in the turbine. CSP is a technologically feasible solar power option in locations with high energy density of sunlight, nonetheless, CSP is currently not cost-competitive, and cannot be without government assistance and regulatory mandates. CSP has a variety of characteristics that opens a pleasant and agreeable pathway for power generation in the field of renewables. First, CSP proposes a confident way to exploit the world's vast and broadly distributed solar resource. Second, during this process of utilization of solar energy, waste water, waste gas and noise, none are produced. More importantly, it does not disturb the ecological balance. Third, solar power is economical source of energy. The initial installation cost is compensated by savings on energy bills. Along with these inherently fascinating features, CSPs also have some serious drawbacks as well. Considering from the industrial perspective, first, CSP systems can only utilize direct solar radiation. This simply means that occasional sunlight and hazy skies can affect the generation from CSP plants a lot. Second, CSP systems are highly sensitive to scale. Particularly, CSP systems need to be large enough (more than tens of megawatts) to reach their techno-economic optimum in terms of minimizing cost and maximizing efficiency. This leads to a requirement of investing enormous capital that only limited investors are capable of taking on. The third challenge is for the deployment of CSP plants with large land and water requirements. Based on the reports with recently commissioned CSP plants, Abengoa's Solana plant and NRG's California Valley Ranch plant, exploit seven to eight acres of land for per megawatt (MW) of capacity. An optimum CSP plant of hundreds of megawatts in size,

would need several thousands of acres of land. This land-use constraint for large-scale implementation is mostly due to the less availability of land with high levels of direct sunlight. Fourth and one of the biggest shortcomings of CSP system is its low efficiency. CSP systems lose huge amount of energy as radiative losses from the incident solar radiations. Considering the efficiency of a typical CSP plant, only 16% of the total incident energy is converted to net electricity energy output, and rest 84% is lost in the environment via convection and radiations.

In 1950s, Israel physicist Tabor[10] introduced the concept of solar selective absorber coatings. This is a significant innovation in the field of solar thermal utilization for it unlocked an advanced generation of high performance of solar absorber coatings. In the recent years, substantial attempts are being made by researchers all over the world, for the development and preparation of novel and outstanding weather resistant coatings. CSP power plants are experiencing rapid growth over the past decades. The first commercialized 11 MW CSP power plant was installed in Spain, designed to generate 23 GW h of electricity per year. Until 2005, the installed global solar thermal utilization power amounted to 120GW with 600 TW h electricity generated[11]. Typically for solar water heating (SWH) systems, the global consumption grew from 160 GW in 2010 to 185 GW in 2011[12, 13].

Although CSPs have the potential to play a powerful role in meeting a reasonable amount of global electricity demand, with a low-carbon future, however, beyond modest efforts and significant government policies, supporting renewables, CSPs would continue to be expensive for large-scale deployment. Therefore, to realize CSPs decent potential, large cost reductions are needed. In addition to this, as the market of solar absorbers is increasing swiftly, a rational and reliable qualification test is still lacking. Not only this, high temperature solar absorber coatings are also deprived of service life predict standard. The exposure of coatings to highly concentrated solar flux makes them undergo high thermal shocks due to the temperature differences during the day and night. Therefore, service life and thermal stability becomes two crucial parameters for high temperature solar absorber coatings.

1.2 Understanding CSPs and thermal power plants

Concentrating solar power (CSP) is established on the fundamental principle of concentrating photons that are straight coming from the sun, without being scattered by the Earth's atmosphere. It utilizes concentrating collectors to supply heat with high temperature to a conventional power cycle. Efficient and cost-effective thermal energy storage technologies can be combined with CSP systems, allowing outcomes according to the demand.

The working principle of CSP is similar to that of a magnifying glass [14] i.e., light is concentrated on a heat absorber that carries a heat transfer fluid which is heated to

high temperatures between 600°C and 1200°C, depending on the technology. As a result of such high temperatures, thermodynamic energy conversion efficiency is high. The heat transfer fluid moves in a closed circuit through the solar receiver tubes and transfers the heat to the power block. Synthetic oils and molten salts are usually used as heat transfer fluids as they have low melting point and very high boiling point. The three main types of CSP systems are: Linear concentrator, dish/engine, and power tower systems. Linear concentrator systems collects sun's energy using long rectangular and curved (U-shaped mirrors). Dish/engine systems use mirrored dish like a large satellite dish. And power tower systems use large flat areas with heliostats to focus and concentrate light on the top of the tower onto a receiver. The figure shown below show three types of CSP systems.

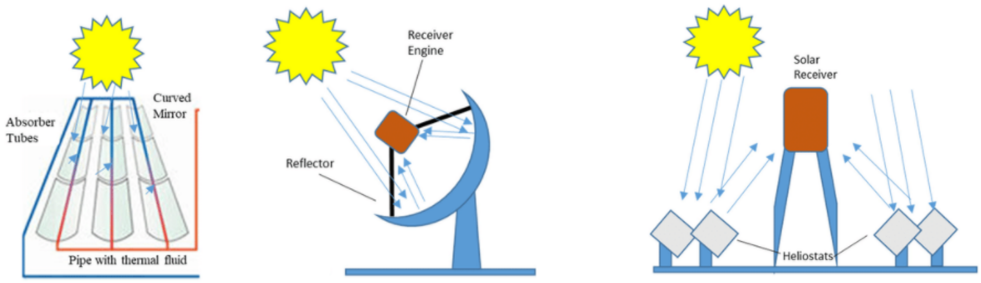

(a) Linear system (b) Dish system (c) Power tower system

Figure 1.1: Three types of CSP systems used in thermal power plants[1].

CSP with thermal energy storage is able to store energy in the form of heat for a long period of time (typically days) with minimal losses. The heat stored can then be converted into electricity and dispatched according to the demand, even during night or during cloudy days. The amount of thermal power generation in a CSP depends on a lot of factors like the area of the collector, intensity of the light falling on the collector, The angle at which the light falls, etc. Amongst these one important factor is also the type of absorber layer used in the collector.

1.3 Overview of composites and metamaterials

For almost a few decades now, composites play a crucial part in the sectors of engineering and technology. Composites have been more than successful in replacing metals and alloys that we use in our lives. In a progressing society like ours, we are highly dependent on composite materials in our daily lives. In industries, composites are the materials fabricated by combining two or more natural and artificial elements together, with distinct physical and chemical properties, and turn out stronger together compared with its individual components[15]. The component materials when blend together do not lose their original identity. They combine and assign their most effective trait to the composite for an improved outcome. The composites are usually designed with a selective use in mind,

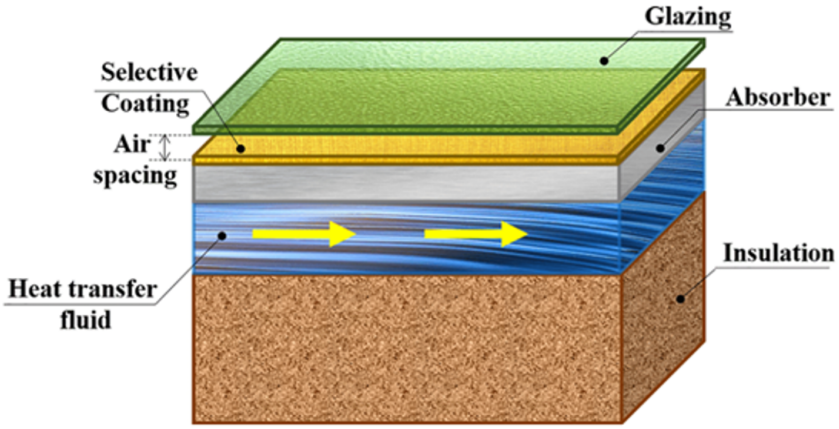

Figure 1.2: A cross-section view of a typical flat-plate solar thermal collector [2].

like improved strength, stiffness, efficiency or durability.

Besides composites, a trending class, called metamaterials have attracted researchers due to plentiful achievable applications like cloaking materials[16, 17, 18], antenna radomes [19, 20], polarization transformers[21], waveguides[22, 23, 24] and many more. Metamaterials are classified as a class of materials that is made of artificial media, that do not exist naturally, possessing amazing properties[25]. Thus, a metamaterial is considered as an artificial material where the electromagnetic properties are represented by permittivity and permeability that can be tuned according to the requirement of the user. Metamaterials are made up of periodic arrays of unit cells, and are metallic resonant elements, where both the element size and the unit cell size are relatively small compared to the wavelength. Electromagnetic materials of such kind were theoretically predicted by H. Lamb [26] in 1904 and then by Russian physicist G. Veselagoin 1968 where he thought about the effects on refraction and reflection of in materials with negative permittivity and permeability [27]. Then in 1999 Sir J. Pendry [28] suggested a theoretical method of creating a lens based on a metamaterial with perfect focus. D. R. Smith in 2000 built the first metamaterial with negative refractive index over the microwave range [29].

1.4 Aim of the study

The main purpose of this study is to introduce and demonstrate solar selective coatings (SSCs) from a three dimensional (3D) structured metal metamaterial on the Silicon (Si) substrate, along with the concept of strong solar absorptance and low infrared (IR) emittance, wavelength selectivity and thermal stability at elevated operating temperatures (close to 1000° C). For high-temperature CSP applications, one strategy is to analyse new materials, including metal inclusions and the dielectric matrix, that have high melting points, high nitriding and high oxidation resistance. Furthermore, the materials for the coatings should be chosen in such a way that another issue of diffusion is avoided. The materials that are compatible and do not diffuse with one another at high temperatures, are to be selected. In order to have the best absorptance, the multilayer cermet absorber

would be converted to a metamaterial by adding an array of metal resonator that behave as plasmonic nanostructures. This study also provides an overview of the behaviour and interaction of electromagnetic field with cermets and metamaterials, both analytically and numerically. Although various solar absorbers with varying materials and designs have been developed and demonstrated, but it is challenging to achieve the above mentioned conditions simultaneously altogether in a single stack of absorber.

In addition, deep knowledge is gained about superior solar selective absorption, flexible tunability of wavelength selective absorption, tunable optical properties, preparation of the multilayer coatings experimentally, and excellent photo-thermal performance, from the computational studies of the wave-optics module by COMSOL Multiphysics. This helps in predicting the optimal design of the absorber coatings, beginning with the interaction of light with the nanostructures, to the achieved solar to thermal conversion efficiency of the system. This work focuses on the demonstration of solar-thermal performance of SSCs by adopting a hybrid strategy (structure-based, material-based, and shape-based) in developing plasmonic metamaterials.

The ultimate aim of this project is to produce and to experimentally validate a numerical procedure that will enable the investigation of operational characteristics of solar selective absorber layers of unconventional design with the intention of boosting light absorption efficiency, over a wide solar spectrum. Although the majority of the work is dedicated to numerical modelling, experimental validation will enable us to demonstrate that the technique can be utilised for the design of general micro–scale composite absorbers.

We would now focus on the methodology that was adopted to carry out this work.

1. At Swansea University (SU), an original multi-scale numerical model including the inclusion at the nano-scale and the absorbing layer at the micro-scale, is developed.

2. At LIST, the nano-scale model developed in SU was employed for developing a new homogenization technique. This technique is used to retrieve the effective material parameters corresponding to the given geometry of the inclusion at the nano-scale. These parameters are used for the simulating the composite dielectric/absorber layer at the micro-scale.

3. At SU, a novel reduced order model technique based on proper orthogonal decomposition (POD) and machine learning algorithm based on neural network (NN) is proposed for solving the problem at nano-scale which enables the exploration of new inclusion designs. In such cases the trail and error approach is not feasible, as the geometric design space for the nano-structure inclusion is vast.

4. At LIST, utilizing this multi-scale numerical model developed at SU, the combination of materials to be used for nano-scale models is studied. This includes the appropriate selection of the materials for the composite and the metallic strip. The

materials chosen should offer a stable unit cell when exposed to elevated temperatures, atmospheric oxygen and moisture.

5. At SU and LIST, linking the models at the nano and the micro scales, an attempt to maximize the optical absorption over the visible light of the spectrum is made. The ultimate aim is the determination of the geometric design, parameters, orientation and periodicity of the inclusions for the absorber layer and the resonator.

6. At LIST, this approach is validated by comparing the optical performance predicted from micro-scale simulations with the experiments performed using facilities at LIST.

7. At SU, the entire modelling system , including the background software , will be made available in open source to allow researchers to treat and mitigate the efficiency of the designs.

1.5 Outline of the thesis

The entire thesis talks about the numerical simulations and the experimental work, altogether. Starting by introducing the current trend of CSPs followed by the physical fundamentals that explains the basics of the work carried out, the thesis proceeds with the outcomes of the numerical simulations simultaneously with the experiments.

- **Chapter 2, Physical fundamentals**

This chapter assembles a complete set of basics that are essential for understanding the thesis. This chapter presents Maxwell's equations, the corresponding boundary conditions and the basic fundamentals of light matter interaction. Characterization of a material by electric permittivity and permeability is well explained along with the details of the optical constants of refractive index and extinction coefficient. These characteristic quantities are well explained in this chapter together with their physical origin. Light matter interaction is described by the macroscopic description of Lorentz and Drude model. In the rest of the chapter the optical behaviour of metamaterials as well as the terminologies related to the metamaterials are defined.

Finally, I present the types of composites and metamaterials that have been a part of SSCs since decades. The chapter is concluded by a summary of literature survey presented through tables highlighting the materials, structures, thickness etc. for the composite and the metamaterials used.

- **Chapter 3, Design, Working and Selection of materials for Spectral Selective Coatings**

This chapter is devoted to design, working and the materials chosen for the SSCs in this work. With the aim of achieving spectral selective coatings with high efficiency and the ones that are thermally and chemically stable at elevated temperatures, we begin

this chapter by explaining the type of SSC chosen for this work along with its design. We then demonstrate the working of the picked design involving the role of individual components of the coating. At the end of the chapter we describe the reasons for choosing the materials for the individual components of SSCs.

- **Chapter 4, Numerical solutions for Maxwell's equations**

Chapter 4 defines the various methods of solving Maxwell's equations in computational electromagnetics (CEM). All the methods defined in this chapter have their own advantages and disadvantage, where one method is a benefit over the other. Since numerical simulations contributes a major part of the thesis, it is worth discussing about the best method suitable for solving the Maxwell's equations.

- **Chapter 5, Solar Selective Coatings: A Methodology for a complete design**

This chapter begins with a brief introduction of the numerical study and the interface used for it-COMSOL Multiphysics. This chapter also concentrates on the terminologies used in the modelling of the micro models(single unit cells) in COMSOL Multiphysics. The chapter overall is dedicated towards the detailed methodology acquired for the synthesis of the SSCs, starting from obeying the outcomes of the numerical simulations to implementing those in the experiments. For the numerical simulations, a multiscale approach was adopted where micro and macro models were prepared corresponding to the outcomes of the experiments to predict the behaviour of entire SSCs. After having achieved the required parameters from the numerical simulations, they are then utilized for performing the experiments.

- **Chapter 6, Results and Discussions**

This chapter is divided into two main sections. The first section talks about the overall structure of the SSCs including the parameters retrieved from the numerical simulations for the experimental synthesis of the SSCs, and the experimental synthesis of the SSCs. It also discusses about the morphological and elemental characterizations performed to better understand the structure of SSCs. The second section concentrates on the optical performance of the SSCs that covers the optical characterizations and thermal stability tests of the SSCs.

- **Chapter 7, Conclusion and Outlook**

This chapter is divided into two sections, the summary and the future scope. The first section summarizes all the results of the former chapters, and the second section outlines the possibles perspectives and applications. A clear comparison of the optical performance is provided for the experimental and numerical work. Along side a validation of the numerical study is also presented.

Chapter 2

Physical Fundamentals

This chapter presents Maxwell's equations, the corresponding boundary conditions and the basic fundamentals of light matter interaction. Other than this, the simulation of electromagnetics in dielectric materials and metamaterial would also be explained. A classic dielectric is characterized majorly by its electric permittivity and magnetic permeability, and equally by its electric and magnetic conductivities. These characteristic quantities are are well explained in this chapter along with their physical origin.

2.1 Maxwell's Equations- Interaction of radiation with matter

In the first section of the chapter we have an outline of the important laws that control the interaction of light with matter, and the approach in which these laws can be adapted to different mechanisms that arise from light matter interaction. According to elementary physics, a charge is enclosed by an electric field, and the moving charge that is an electric current, develops magnetic field. In addition to this, the accelerated charges emit electromagnetic radiations, while radiations accelerate the charged particles. Maxwell's equation summarizes all these phenomena explaining the dynamics free charges, currents, electric and magnetic fields, indicating the basics of classical electromagnetic theory, that deeply explains interaction of light and matter. These theoritical concepts were formulated primarily through experiments conducted by many scientists-Faraday, Ampere, Volta, Lenz, Coulomb, Gauss and others, in the nineteenth century. These equations were condensed into a set of vector equations by Maxwell, widely acclaimed Maxwell's equations. These equations broadly explains the nature of the charges in an electric and magnetic field, both in vaccum and in material. When the electromagnetic radiation crosses one medium to reach another in metals or dielectrics, the boundary conditions are considered. A touch of boundary conditions and its outcomes on the electric and magnetic fields is also represented. Next, TE "transverse electric" and TM "transverse magnetic" modes of the electromagnetic wave are described.

Beginning with Maxwell equations, four coupled equations explaining interactions of electric and magnetic fields with matter [30] are the principle of classical optics and

electrodynamics.

Maxwell's Equations in Differential form

$$\nabla \times \mathrm{H} = \mathrm{J_f} + \frac{\partial \mathrm{D}}{\partial \mathrm{t}} \tag{2.1}$$

$$\nabla \times \mathrm{E} = -\frac{\partial \mathrm{B}}{\partial \mathrm{t}} - \mathrm{J_m} \tag{2.2}$$

$$\nabla.\mathrm{B} = 0 \tag{2.3}$$

$$\nabla.\mathrm{D} = \rho \tag{2.4}$$

Where $\tilde{\mathrm{E}}$ is the electric field, $\tilde{\mathrm{H}}$ is the magnetic field of the electromagnetic radiation. D is the electric flux density and B is the magnetic flux density. J_f repesents the total current density which is the sum of J_e the electric current density and J the current density rising from the sources other than the conductivity. $\mathrm{J}_m = \sigma_m \mathrm{H}$ where σ_m is a non real physical quantity needed at space boundaries for artificial absorption, called magnetic conductivity, and ρ is the charge density. For ease and clarity, we ignore writing the time and spatial dependence, $\tilde{\mathrm{E}} = \tilde{\mathrm{E}}(\mathrm{r}, \mathrm{t})$. If we permit materials with isotropic and non-dispersive, where ϵ and μ are independent of the frequency of the incoming electromagnetic wave, electric losses attenuating electric fields by conversion to heat energy then the electric current density turns $\mathrm{J}_e = \sigma\tilde{\mathrm{E}}$, where σ is the conductivity.

For a simple case, a linear, isotropic and non-dispersive material would have the following constitutive relations

$$\mathrm{D} = \epsilon\tilde{\mathrm{E}} \tag{2.5}$$

$$\mathrm{B} = \mu\tilde{\mathrm{H}} \tag{2.6}$$

These are the relations of flux densities to the fields with the magnetic permeability μ and electric permittivity ϵ. Here $\epsilon = \epsilon_\mathrm{r}\epsilon_0$ and $\mu = \mu_\mathrm{r}\mu_0$ where ϵ_r is the relative electric permittivity and μ_r is the relative magnetic permeability . $\epsilon_0 = 8.854187817.10^{-12}\mathrm{As/Vm}$ is the electric permittivity of free space and $\mu_0 = 4\pi 10^{-7}\mathrm{N/A}^2$ is the magnetic permeability of free space.

2.1.1 Electromagnetic Boundary Conditions at material interface

The behaviour of the field at different interfaces are explained by the boundary conditions. The combinations of interfaces can be air-metal or metal-dielectric. The boundary conditions for two finite conductivity media is not infinite, and is defined by $\epsilon_1, \epsilon_2, \mu_1, \mu_2$. They are

$$\hat{\mathrm{n}} \times \left(\tilde{\mathrm{E}}_2 - \tilde{\mathrm{E}}_1\right) = 0 \tag{2.7}$$

$$\hat{n} \times \left(\tilde{H}_2 - \tilde{H}_1\right) = 0 \tag{2.8}$$

$$\hat{n}.\left(D_2 - D_1\right) = 0 \tag{2.9}$$

$$\hat{n}.\left(B_2 - B_1\right) = 0 \tag{2.10}$$

These boundary conditions can also be displayed in a different form

$$\tilde{E}_{2t} = \tilde{E}_{1t} \tag{2.11}$$

$$\tilde{H}_{2t} = \tilde{H}_{1t} \tag{2.12}$$

$$\tilde{E}_{2n}\epsilon_2 = \tilde{E}_{1n}\epsilon_1 \tag{2.13}$$

$$\tilde{H}_{2n}\mu_2 = \tilde{H}_{1n}\mu_1 \tag{2.14}$$

where $'n'$ refers to "normal" and $'t'$ refers to "tangential". 1 and 2 mentioned in subscript are the two different media that the light crosses. For more information on this, refer to [31] . Figure 2.1 shows the graphical representation of the boundary condition for the electric field.

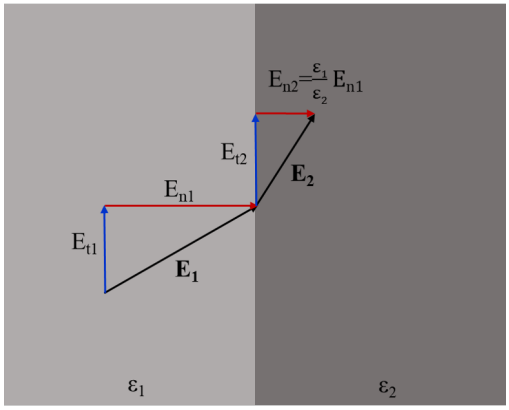

Figure 2.1: Electric field vector for boundary conditions with $\epsilon_1 < \epsilon_2$.

2.1.2 Transverse Electric (TE) and Transverse Magnetic (TM) modes

The boundary conditions are different for the normal and tangential components of the electromagnetic radiation. Therefore, the incoming wave is split into two parts by defining a plane connected by the incident and reflected wavevector k_i and k_r. The incoming electric field vector is divided into a part that is perpendicular to the plane of incidence called the s-polarised wave (TE mode) and parallel to the plane of incidence called the

p-polarised wave (TM mode). The total electric field $\tilde{E} = \tilde{E}_p + \tilde{E}_s$ is represented graphically in Figure 2.2 For the TE mode, the electric field component is perpendicular to the direction of propagation of the wave and magnetic field component is parallel to the direction of propagation of the wave. Whereas for the TM mode , the electric field component is parallel to the direction of wave propagation and the magnetic field component is perpendicular the direction of wave propagation.

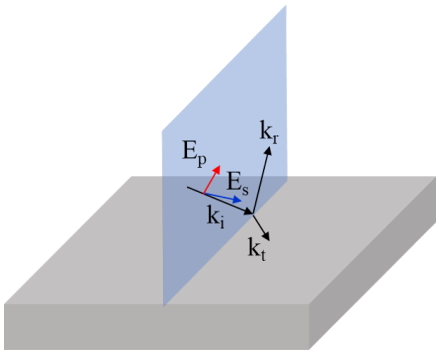

Figure 2.2: TE and TM mode of an electric field.

2.1.3 Constitutive equations

Based upon the book Advanced Engineering Electromagnetics[31] this section of the chapter describes the origin of the electric permittivity ϵ and magnetic permeability μ in dielectrics. The charges in atoms and molecules for a dielectric are held together in a place by their atomic and molecular forces. On applying an external electric field, the centroid of these confined positive and negative charges is moved slightly in position relative to each other, forming an electric dipole moment. In case of a polar material even when no electric field is applied, local dipole moments dp_i are still present amid the charges. As a result of random orientation of the dipole moments, the electric polarization vector is nil, and the local polarization vectors eliminate each other. The applied electric field results in the alignment of all the charges along the field lines. Nonetheless, all the charges between the top and the bottom surface of a dielectric omit each other. $+q_{sp}$ and $-q_{sp}$ are the only charges that remain on the surface. These remaining charges forms the polarization density vector P. This polarization do not alter the value of the applied electric field E but alters the value of the electric flux density D in the material. For a dielectric in free space $D_{freeSpace} = \epsilon_0\tilde{E}$ for same applied field and in case of the presence of P, $D_{Dielectric} = \epsilon_0\epsilon_r\tilde{E} = \epsilon\tilde{E}$ or $D_{Dielectric} = \epsilon_0\tilde{E} + P$. On assuming a relation of linear proportionality between $\tilde{E}$ and P, results in $P = \epsilon_0\chi_e\tilde{E}$ where χ_e is the electric susceptibility which is a dimensionless quantity. This results in

$$D_{Dielectric} = \epsilon_0\tilde{E} + P = \epsilon_0\tilde{E} + \epsilon_0\chi_e\tilde{E} = \epsilon_0(1 + \chi_e)\tilde{E} = \epsilon_0\epsilon_r\tilde{E} \tag{2.15}$$

A similar relation is obtained in magnetic dipoles in a dielectric under the influence of a magnetic field for the magnetic polarization vector M where $M = \mu_0\chi_m\tilde{H}$ where χ_m

is the magnetic susceptibility. Generally, susceptibilities are tensors and the relationship between the corresponding fields and the polarization is linear when the applied field is not very strong. To sum up, the permittivity (permeability) is the ability of a medium to store electric (magnetic) energy when exposed to an electric (magnetic) field.

2.1.4 Electric and Magnetic Conductivities

The amount of these free charges present in the metals is large and are free to move. Whereas, in dielectrics these charges are confined and do not move freely around. For this reason the conductivity in metals is much higher than in dielectrics. The permittivity and permeability are complex numbers and are expressed as $\epsilon = \epsilon' + \mathrm{i}\epsilon'' = \epsilon' + \mathrm{i}\sigma/\omega$, $\mu = \mu' + \mathrm{i}\mu'' = \mu' + \mathrm{i}\sigma/\omega$ where ϵ', μ' and ϵ'', μ'' are the real and the imaginary parts of permittivity and permeability respectively and ω is the angular frequency. It is noted from these formulas, that conductivity depends on the imaginary parts of ϵ and μ that represents the power loss. The materials for which $\sigma \approx 0$ are called lossless materials with conductivity $\sim 10^{-24}$S/m e.g. air or vacuum. The materials for which $\sigma > 0$, they are called lossy materials , e.g. carbon, germanium and sea water. The materials with $\sigma \approx \infty$ are characterized as metals eg, iron, silver, gold with conductivity 6.3×10^7S/m for silver. Ohm's law relates E with J via σ,

$$\mathrm{J} = \sigma \mathrm{E} = \frac{1}{\rho}\tilde{\mathrm{E}} \tag{2.16}$$

In a conductor, the electric field exists for a very short duration of time. If a positive charge is brought closer to a conductor, $\tilde{\mathrm{E}}$ would be created for a very short time due to charge separation. The created $\tilde{\mathrm{E}}$ will displace the electrons that are free to move around until the $\tilde{\mathrm{E}}$ is cancelled. For this reason, the metals are also called perfect electric conductors (PEC). Constitutive equations for isotropic linear materials are written as in equation 2.5 and 2.6These material parameters are simple scalars for frequency dependent and independent cases. For anisotropic cases they become matrices $\overline{\overline{\epsilon}}, \overline{\overline{\mu}}$.

2.2 Solar thermal radiation

As discussed in above in section 2.1 electromagnetic radiation can be stated as a wave phenomenon with a combination of electric ($\tilde{\mathrm{E}}$) and magnetic ($\tilde{\mathrm{H}}$) fields, which oscillate in a phase orthogonal to each other and orthogonal to the direction of propagation, as shown in the figure 2.3. James Clerk Maxwell in 1865, made one of the most significant contribution on the electromagnetic phenomenon, where he proved theoretically that electric and magnetic field combines into a wave equations, which supports the fact that light is an electromagnetic phenomenon classified to its wave frequency. Electromagnetic wave is a transverse wave, which is combined of the oscillating $\vec{\mathrm{E}}$ with the magnetic field $\vec{\mathrm{B}}$, and is grouped according to the wavelength (λ) of its wave. Light spectrum is classified into Electromagnetic radiations according to increasing λ in the order: gamma rays, X-rays,

ultraviolet (UV) radiation, visible light (Vis), infrared (IR) radiation, microwaves and radio waves. Thus, the range of electromagnetic spectrum starts from $10^{-9}\mu$m(gamma rays) until $10^{10}\mu$m(long radio waves).

But, if restrictions are imposed to oscillation planes of the waves, a polarized wave is obtained. Now, for a plane-polarized (linearly polarized) wave travelling in x-direction, its electric and magnetic field are given by

$$\tilde{\mathrm{E}} = \mathrm{E}_0 \sin\left[2\pi\left(\frac{\mathrm{x}}{\lambda} - \mathrm{vt}\right)\right] \tag{2.17}$$

$$\tilde{\mathrm{H}} = \mathrm{H}_0 \sin\left[2\pi\left(\frac{\mathrm{x}}{\lambda} - \mathrm{vt}\right)\right] \tag{2.18}$$

that are always in the same two orthogonal planes. Here E_0 and $\mathrm{H}_0$are the amplitudes of the electric and magnetic field respectively, λ is the radiation wavelength and v is the frequency.

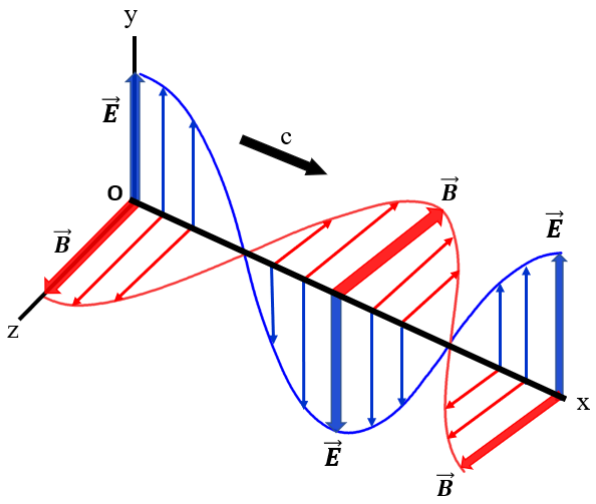

Figure 2.3: Electric and magnetic field components of the incoming electromagnetic radiation.

Now, the relation between frequency and wavelength is:

$$v = \frac{c}{\lambda} \tag{2.19}$$

where c is the velocity of propagation of the wave. In vacuum, c is equal to the speed of light (c), but in general $\mathrm{c} = \mathrm{c}_0/\mathrm{n}$, where, n is the refractive index of the medium the light is propagating through.

The inverse of wavelength is known as a wavenumber and given in units of cm^{-1}, as:

$$\tilde{v} = \frac{1}{\lambda} \tag{2.20}$$

Planck and Einstein showed that the electromagnetic wave properties of a particle, and corpuscular theory states that em radiation can be described as photons (quantum

energy packets) possessing an energy given by:

$$\mathrm{E} = \mathrm{hv} \tag{2.21}$$

where, v is the radiation frequency and h is the Planck's constant.

Then de Broglie stated that if an electromagnetic wave can possess the properties of a particle, then a particle can also showcase the wavelike properties. The wavelength of the particle acting as a wave depends on its momentum p, as:

$$\lambda = \frac{\mathrm{h}}{\mathrm{p}} = \frac{\mathrm{h}}{\mathrm{mv}} \tag{2.22}$$

where, m is the mass of the particle and v is its velocity.

Bohr established that absorption or emission of em radiation happens as a result of quantization of atomic and molecular energy levels. For a transition between state 1 and state 2 in a system, the energy of the em absorbed is equal to the difference of energy between the two states:

$$\triangle\ \mathrm{E}_{1\to 2} = \mathrm{E}_2 - \mathrm{E}_1 = \mathrm{h}v \tag{2.23}$$

On the other hand, the emission of a radiation occurs when the atomic or a molecular system comes to a lower energy state from an excited higher state. As a result, the difference in energies, of different molecular levels in the system, corresponds to em radiation of different frequency.

It has been confirmed above that when an em radiation passes through the matter, it is absorbed if the energy of the incoming radiation corresponds to the energy difference between two stationary states of atoms or molecules in the matter. If this is not the case, then the em radiations passes through the matter unaffected, and a small part of the light is scattered in all the directions in the matter. This scattering can be of two types: elastic and inelastic. Elastic scattering occurs when the wavelength of the incident beam is equal to the wavelength of the light scattered. This can be explained classically, when the oscillating incoming em wave excite the electron cloud of the atoms or the molecules in the matter, they vibrate at the same frequency as the as that of the incident beam. The system formed by the oscillating electron cloud and the positive nuclei comprise of an oscillating dipole that instantly radiates at the same frequency in all random directions[32].

Elastic scattering depends on the size of the particles that scatter radiation. If the wavelength of the incoming em radiation is larger than the size of the particle in the matter it reacts to, the intensity of scattered light, $\mathrm{I_S}$, is proportion to the wavelength of the incident beam as $\mathrm{I_S} \propto {}^{1}\!/\!_{\lambda^4}$. This relation is called Reyleigh scattering and indicates that light with shorter wavelengths are scattered more when they interact with the particles in the matter. The blue color of the sky justifies Rayleigh scattering. When the wavelength of the incident em radiation equals the size of the particle in the matter it interacts with,

then Mie scattering is observed. The intensity of Mie scattering depends partially on the incoming wavelength and becomes independent of wavelength when the size of the particles surpasses the wavelength. Clouds in the sky holding larger droplets of watter scatters white light[32][33], this is a typical example of Mie scattering.

If the incident radiation excites the atoms or molecules of the matter it falls on, to a state higher or lower than the initial state, then there is a shift in frequency of the scattered light. This process is known as inelastic scattering. Raman Spectroscopy[34][35] is the most popular technique among inelastic scattering.

All materials emit electromagnetic radiation, with an intensity and wavelength dependent on its temperature (T) and optical characteristics. For example, a black-body is a perfect absorber absorbing all incoming radiations, whose wavelength distribution of radiation emitted is given by Plank's radiation law [36, 37]:

$$\mathrm{E_{b\lambda}}(\lambda, \mathrm{T}) = \frac{2\pi \mathrm{hc}^2}{\lambda^5} \left[\frac{1}{\mathrm{e}^{\mathrm{hc}/\lambda \mathrm{k_B T}} - 1} \right] \tag{2.24}$$

where, h is Planck's constant, $\mathrm{k_B}$ is Boltzman's constant, and c is the speed of light in vacuum. $\mathrm{E_{b\lambda}}$ represents the emissive power of the black-body ($\mathrm{W/m^2}\mu$m), i.e. energy per unit area per unit time per unit wavelength interval.

Black-body being an ideal physical body absorbs all the incident radiation and emits maximum amount of energy for a given temperature, is used as a reference for the comparison of real surfaces. The wavelength corresponding to the maximum of the distribution in the black-body radiation, decreases with temperature as stated by Wien's displacement law:

$$\lambda(\mathrm{E_{b,max}})\mathrm{T} = 2897.8 \times 10^{-3} \mu\mathrm{m.K} \tag{2.25}$$

The total emissive power $\mathrm{E_{b\lambda}}$of a black-body, by Stefan-Boltzmann law, is given by:

$$\mathrm{E_{b\lambda}} = \int_0^\infty \mathrm{E_{b\lambda}}(\lambda, \mathrm{T}) \mathrm{d}\lambda = \sigma \mathrm{T}^4 \tag{2.26}$$

where, σ is the Stefan-Boltzmann constant, with the magnitude of $5.6696 \times 10^{-8} \mathrm{W/m^2K^4}$.

Thus, for any real object, the emissive power E is expressed as:

$$\mathrm{E(T)} = \mathrm{e(T)} \sigma \mathrm{T}^4 \tag{2.27}$$

where, e(T) is the emissivity of the object.

The black-body is a perfect diffuse emitter, such that the intensity of radiation I_b is constant in all directions:

$$\mathrm{E_b} = \pi \mathrm{I_b} \tag{2.28}$$

Sunlight is an electromagnetic radiation in the spectral range $0.3 - 4$ μm with the maximum intensity of about $0.5 - 0.7$ μm, corresponding to an effective black-body tem-

perature of around 5800K[38]. For solar applications, the most important wavelength ranges from UV/Vis/NIR ($\lambda = 0.3 - 2.5\mu$m) to far infrared (λ=2.5−50 μm). This range covers the solar spectral range and the spectral range of thermal radiation emitted from a surface holding an ambient temperature of up to 100°C . As defined in the American Society for Testing and Materials (ASTM) G173-03, the solar spectra irradiance distribution that reaches the surface of the Earth, for an air mass 1.5 (AM1.5), at 37° sun facing tilted surface[39], is shown in the figure 2.4. Low-intensity, terrestrial solar radiation is a variable energy of about 1367W/m^2 reaching the earth's surface. Outside the atmosphere, the spectrum denoted is AM 0, while the radiation that travels through the atmosphere is AM X, where X is given by 1/cos$\theta_z$for θ_z less than 70°. θ_z is the angle of incidence with respect to zenith[37].

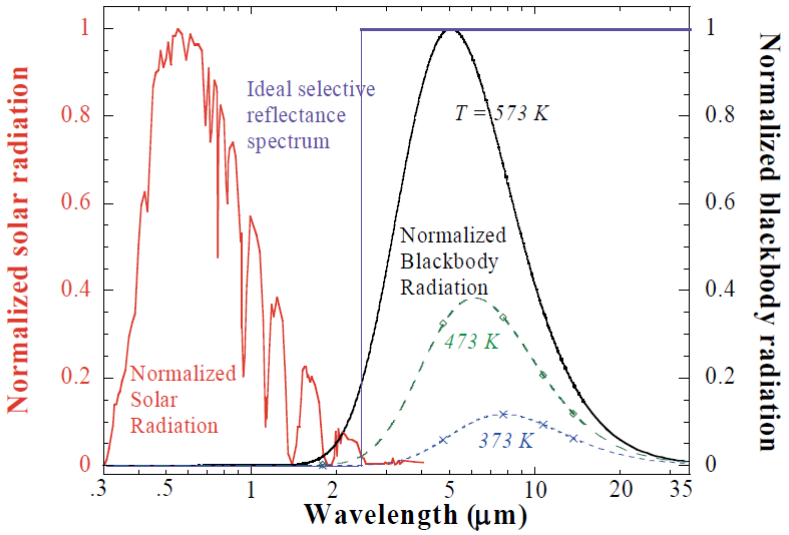

Figure 2.4: The graph depicts the normalized solar spectral irradiance for AM1.5, as well as spectral reflectance of an idealized solar selective coating and the normalised Blackbody radiation spectrum at various temperatures[3].

2.2.1 Ideal solar spectral selectivity

As the sunlight reaches a surface, a part of this incident light is reflected from the surface, and a part is of it enters the surface to be absorbed by the medium and transmitted through the medium. For solar-thermal energy conversion systems; it is advantageous to have all the incident light being absorbed by the medium, to transfer high fraction of captured energy for the application through the working fluid. Some amount of energy is inevitably lost from the heated absorber due to conduction, convection and radiation, however, this loss can be minimized by numerous methods. For instance, a thermal insulation and a glass cover used by a flat plate collector, and the vacuum in tube collector, reduces the loss due to conduction and convection[40]. The radiation loss in these two mentioned collectors can be suppressed by spectrally selective absorber surface, i.e. depending on the materials used[41].

The interaction of electromagnetic radiation with the matter can be determined by intrinsic parameters of the material. The amount of light that is reflected from the surface of the matter is quantified by coefficient of reflectance (R), and is defined as the ratio of intensities of light reflected (I_R) to the incident light (I_0). Similarly, the amount of light transmitted through the material is quantified by coefficient of transmission (T), defined by the ratio of intensities of light transmitted (I_T) to the incident light. A clear schematic for this is shown below in the figure 2.5.

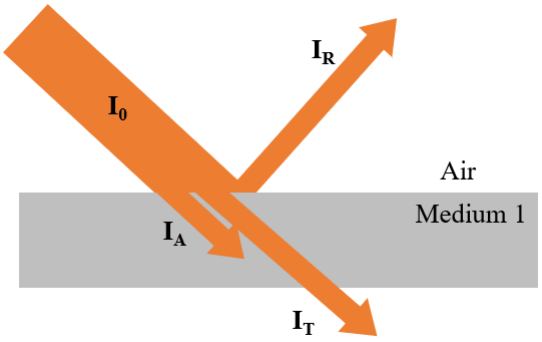

Figure 2.5: Reflection, absorption and transmission of a beam of light incident on a medium.

According to the law of conservation of energy, sum of T, R and absorption A of the incident flux, for each wavelength is equal to unity:

$$R(\lambda) + T(\lambda) + A(\lambda) = 1 \tag{2.29}$$

Where the above equation comes from the incident electromagnetic radiation (I_0) which is given by:

$$I_0 = I_R + I_T + I_A \tag{2.30}$$

The definition of emissivity, $e(\lambda)$, is the ratio between infrared light emitted from the surface to that emitted perfect black-body at same wavelength and temperature. According to the Kirchoff's law, the emissivity is equal to absorption:

$$e(\lambda) = A(\lambda) = 1 - R(\lambda) - T(\lambda) \tag{2.31}$$

Equation 2.31, for an opaque surface where transmission is zero, becomes:

$$e(\lambda) = 1 - R(\lambda) \tag{2.32}$$

An ideal absorber should have zero reflectance in the solar spectral range to seize maximum solar energy, and reflectance equal to unity in the infrared wavelength range to minimize the radiation losses. Thus, an ideal spectrally selective surface should have a sharp transition from low to high reflectance at a transition wavelength. This behaviour is known as crossover behaviour, step

function or reflectance transition behaviour, etc. by different authors. A curve with this behaviour is shown in blue in the figure 2.4. Thus, solar absorptance and thermal emittance are the two key parameters for characterizing the nature of selective solar absorbing coatings. Below equation 2.33 calculates the total solar absorptance, α_{S}, with normal angle of incidence, is a weighted average, weighted by solar spectral radiation, $\mathrm{I_S}(\lambda)$, between $\lambda_1 = 0.3\mu$m to $\lambda_2 = 4.1\mu$m.The following calculation has been done under AM 1.5 solar spectrum, defined by the ISO standard 9845-1 (1992) [42].

$$\alpha_{\mathrm{S}} = \frac{\int_{\lambda_1}^{\lambda_2}(1-\mathrm{R}(\lambda))\mathrm{I_S}(\lambda)\mathrm{d}\lambda}{\int_{\lambda_1}^{\lambda_2}\mathrm{I_S}(\lambda)\mathrm{d}\lambda} \tag{2.33}$$

Similarly, equation 2.34 shows total thermal emittance, ϵ_{t}, at normal incidence, is a weighted average, weighted by the blackbody radiation, $\mathrm{I_b}(\lambda,T)$, at a given temperature, T, where $\lambda_3$depends on the temperature and $\lambda_4 = 100\mu m$ [43]. For T = 373K, $\lambda_3$is $2\mu m$.

$$\epsilon_{\mathrm{t}} = \frac{\int_{\lambda_3}^{\lambda_4}(1-\mathrm{R}(\lambda))\mathrm{I_b}(\lambda,\mathrm{T})\mathrm{d}\lambda}{\int_{\lambda_3}^{\lambda_4}\mathrm{I_b}(\lambda,\mathrm{T})\mathrm{d}\lambda} \tag{2.34}$$

2.3 Optical properties and optical constants of materials

The absorption of light falling on the surface is related to the attenuation of light intensity I when the light travels through the material, following Beer-Lambert law 2.35:

$$\mathrm{I} = \mathrm{I_0}\mathrm{e}^{-a\mathrm{x}} \tag{2.35}$$

where, a is the attenuation coefficient (also referred as absorption coefficient) and x is the thickness of the film (also referred as propagation distance). This attenuation coefficient, a, is directly proportional to the extinction coefficient, k, of the material, which measures how fast the light disappears in a material. If the material is transparent then k becomes 0,and thus a, this means all the radiations would pass through the material. The light intensity I is related to electric field amplitude through:

$$\mathrm{I} \propto \mid \tilde{\mathrm{E}}_0 \mid \tag{2.36}$$

It can be concluded:

$$a = \frac{2\omega k}{\mathrm{c}} = \frac{4\pi k}{\lambda} \tag{2.37}$$

and

$$\ln(\frac{\mathrm{I}}{\mathrm{I_0}}) = -a\mathrm{x} = -4\pi\frac{k\mathrm{x}}{\lambda} \tag{2.38}$$

If the material is too thin i.e. $\lambda \gg k$x, then it becomes transparent[44][45][46].

The relation between the speed of light in the material (v) and the speed of light in vacuum ($\mathrm{c} \approx 3.00 \times 10^8$m/s), is expressed in terms of refractive index (n) by Snell's

law[47] as:

$$\mathrm{n} = \frac{\mathrm{c}}{\mathrm{v}} \tag{2.39}$$

Thus, reflection happens at the interface of the two materials having different refractive indices, the absorption of light takes place during the propagation of light through the material, and the transmittance entirely depends on the absorption, as unabsorbed beams are the ones that are transmitted. There are other phenomenons that take place while the light propagates through the material, such as, scattering, polarization, luminescence and diffraction[48].

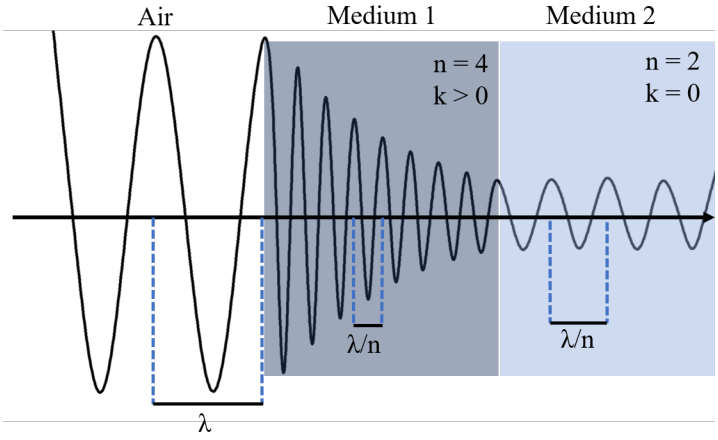

Figure 2.6: The incident light wave travels from air ($\mathrm{n} = 1; k = 0$) into an absorbing medium 1 ($\mathrm{n} = 4; k > 0$), and then into a transparent medium 2 ($\mathrm{n} = 2; k = 0$). The phase velocity and the wavelength of the wave is different in each medium depending on the index of refraction.

Both n and k are intrinsic values for a material that depends on the wavelength of the incident light. These two quantities can be incorporated into a single quantity called complex refractive index ($\tilde{\mathrm{n}}$), where n' becomes the real part and k, the imaginary part. The relation between the complex refractive index and the dielectric function ($\tilde{\epsilon}$) is derived from Maxwell's equation[49], written as :

$$\tilde{\mathrm{n}} = \mathrm{n}' + \mathrm{i}k = \sqrt{\tilde{\epsilon}(\omega)} \tag{2.40}$$

where, $\tilde{\mathrm{n}}$ describes how an electromagnetic wave propagates through the medium, the real part n' describes how fast the wave travels in the medium, the imaginary part k is responsible for wave loss or decay; describes how the wave decays as the function of position and $\tilde{\epsilon}(\omega)$is the dielectric function of the material. The dielectric function and the complex index of refraction are called optical constants. The real and the imaginary part of the optical constants are not independent and they are mathematically connected through Kramers-Kronig relationship[50]. The complex dielectric function $\tilde{\epsilon}(\omega)$ describes the electrical and optical properties versus wavelength, frequency or energy. It also describes electric polarizability ($\vec{\mathrm{P}}$) and absorption properties of the material which is given

by:

$$\tilde{\mathrm{P}} = \epsilon_0 \chi \tilde{\mathrm{E}}(\mathrm{x}, \mathrm{t}) \tag{2.41}$$

with the relative dielectric function $\tilde{\epsilon_r}$ and the susceptibility χ relation, at high frequency limit:

$$\tilde{\epsilon_r} = 1 + \chi \tag{2.42}$$

The complex relative dielectric function $\tilde{\epsilon_r}$can be expressed as real and imaginary parts as $\tilde{\epsilon_\mathrm{r}} = \epsilon_1 + \mathrm{i}\epsilon_2$. From the relation between the complex refractive index, equation 2.40, and complex relative dielectric function, it is possible to write $n$and k from in terms of $\epsilon_1$and ϵ_2, and vice versa as following[51]:

$$\epsilon_1 = \mathrm{n}'^2 - k^2, \epsilon_2 = 2\mathrm{n}'k \tag{2.43}$$

with

$$\mathrm{n}' = (\epsilon_1 + (\epsilon_1^2 + \epsilon_2^2)^{1/2})^{1/2}, k = (-\epsilon_1 + (\epsilon_1^2 + \epsilon_2^2)^{1/2})^{1/2} \tag{2.44}$$

The refractive index n for the absorbing layers of selective solar thermal absorbers should be an increasing function of wavelength in the visible range $(300-1000\mathrm{nm})$ because it contributes to the solar absorption enhancing through the interference effect.

2.4 Solid State Optics

2.4.1 Macroscopic description

In the above sections, we learned the relation of the optical effects such as absorption, reflection and transmission related to the refractive index. In this section we will throw light on the optical response of the material with a strong absorption at one or more frequencies. We will first obtain the response of a simplified atom using a Lorentz model and then the Drude model assuming the electrons that surround atoms as being bound to the atom core with a phenomenological spring constant. This gives reasonably realistic projection of dispersion of the refractive index in regions of low absorption and a close understanding of n and k trends near these regions of strong absorption.

The nucleus of the atom much more massive than the electron, so that we can treat this as spring mass system. If we let go the mass, the spring will move back and forth and would be resonant.

2.4.1.1 Optical properties of dielectric material and the Lorentz Model

To predict the optical response of valence electrons in the presence of an oscillating em field, the electronic response follows the equation of motion $\mathrm{F} = \mathrm{ma}$ taking into account the electric driving force, the friction force (damping rate), and the restoring force. The

equation of motion thus becomes:

$$\mathrm{m}\ddot{\mathrm{r}}(\mathrm{t}) + \mathrm{m}\Gamma\dot{\mathrm{r}}(\mathrm{t}) + \mathrm{m}\omega_0\mathrm{r}(\mathrm{t}) = -\mathrm{qE} \tag{2.45}$$

where, going from left to right, the first term is the acceleration force, second is the frictional force, third is the restoring force with $\omega_0 = \sqrt{k/m}$ and term on the right of the equation is the electric/driving force.

The fourier transform of the equation 2.45 gives an expression for the (complex) harmonic motion amplitude $\mathrm{r}(\omega)$ in response to a harmonic driving field with amplitude $\mathrm{E}(\omega)$:

$$\mathrm{r}(\omega) = \frac{-\mathrm{q}}{\mathrm{m_e}} \frac{1}{\omega_0^2 - \omega^2 - \mathrm{i}\omega\Gamma} \mathrm{E}(\omega) \tag{2.46}$$

The expression for dipole moment μ, which is defined as charge times separation distance. Since the core of the atom is assumed to be stationary at position zero, the dipole moment becomes:

$$\mu(\omega) = \frac{\mathrm{q}^2}{\mathrm{m_e}} \frac{1}{\omega_0^2 - \omega^2 - \mathrm{i}\omega\Gamma} \mathrm{E}(\omega) \tag{2.47}$$

Describing the dipole moment with a quantity known as polarizability α, the dipole moment and the driving field according to $\mu = \alpha\mathrm{E}$, results in an expression for the Lorentz polarizability α:

$$\alpha(\omega) = \frac{\mathrm{q}^2}{\mathrm{m_e}} \frac{1}{\omega_0^2 - \omega^2 - \mathrm{i}\omega\Gamma} \tag{2.48}$$

With N atoms per unit volume , the net dipole moment per unit volume is

$$\tilde{\mathrm{P}} = \mathrm{N}\tilde{\mu}(\omega) = \mathrm{N}\alpha(\omega)\mathrm{E}(\omega) \tag{2.49}$$

With the Lorentz expression for polarization $\mathrm{N}\alpha(\omega)\mathrm{E}(\omega)$ with the relation $\mathrm{P}(\omega) = \epsilon_0\chi(\omega)\mathrm{E}(\omega)$ we obtain an expression for the frequency dependent susceptibility:

$$\chi(\omega) = \frac{\mathrm{Nq}^2}{\mathrm{m_e}\epsilon_0} \frac{1}{\omega_0^2 - \omega^2 - \mathrm{i}\omega\Gamma} \tag{2.50}$$

Note that χ is dimensionless, so that the term $\frac{\mathrm{Nq}^2}{\mathrm{m_e}\epsilon_0}$ has dimensions of ω^2. So, we set

$$\omega_\mathrm{p}^2 = \frac{\mathrm{Nq}^2}{\mathrm{m_e}\epsilon_0} \tag{2.51}$$

or equivalently

$$\omega_\mathrm{p} = \sqrt{\frac{\mathrm{Nq}^2}{\mathrm{m_e}\epsilon_0}} \tag{2.52}$$

where, ω_p is the plasma frequency.

The real and the imaginary parts of the dielectric function becomes

$$\epsilon_1(\omega) = 1 + \omega_p^2 \frac{\omega_0^2 - \omega^2}{(\omega_0^2 - \omega^2) + \omega^2\Gamma^2} \tag{2.53}$$

$$\epsilon_1(\omega) = 1 + \omega_p^2 \frac{\omega_0^2 - \omega^2}{(\omega_0^2 - \omega^2) + \omega^2\Gamma^2}, \epsilon_2(\omega) = \omega_p^2 \frac{\omega}{(\omega_0^2 - \omega^2) + \omega^2\Gamma^2}$$

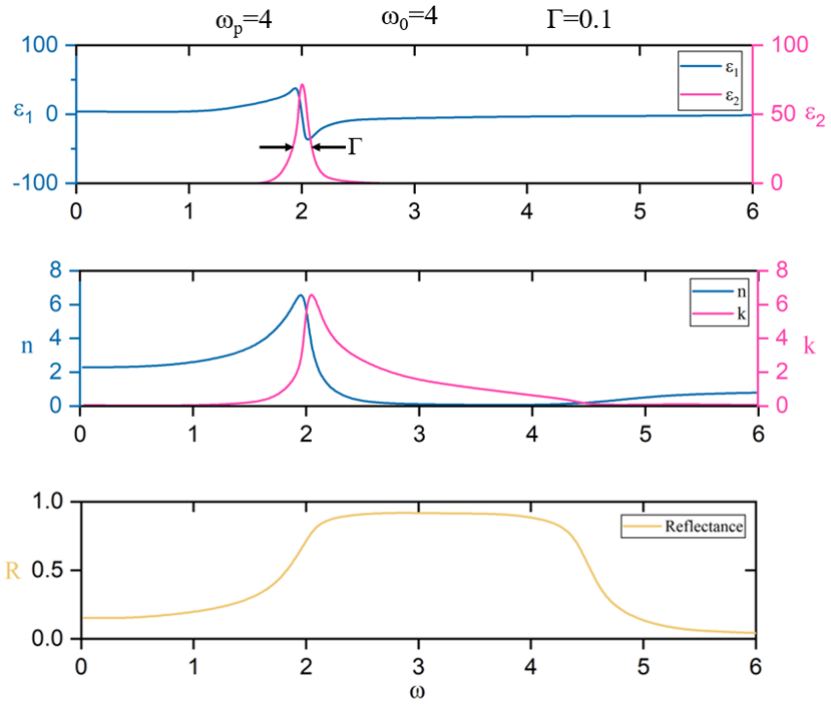

Figure 2.7: Typical Lorentz response for dielectrics.

In the above graphs shown in Figure 2.7 that show a typical Lorentz response for the dielectrics, it is clearly seen that the resonance occurs when the frequency is 2 and the plasma frequency is at around 4.5. Below the resonance, we have flat looking permittivity and the refractive index which shows that the materials in this region are transmissive. At the resonance, the properties of the materials become very extreme, and the refractive index and the dielectric constant goes way up i.e, the loss goes up and the material becomes absorbing at the resonance peak. Above the resonance, the materials becomes very reflective, and above the plasma frequency is a switch between reflected and transmissive region. Also, at the resonance, we get a sharp drop in the real part of the ϵ which is called anomalous or negative dispersion, and over most of the frequency range it is slowly increasing which is called positive dispersion.

From the above graphs, in the one on the top, the damping rate (Γ) determines the width of the resonance. The bigger the Γ, the wider is the resonance. Smaller the Γ, the narrower is the resonance. The material has no response at frequencies far above the resonance. In this region, the material becomes transparent whereas on the opposite side of the spectrum there is low loss but there is DC offset in the dielectric constant. This

is the region we work in when we design a device. It is worth noting that the dielectric constant can be negative and/or less than one around the resonance. From the graph in the middle, far from resonance, the loss is very low, and that n can be less than one around the resonance.

2.4.1.2 Optical properties of metals and the Drude Model

In metals, most of the electrons are free and not bound to the nucleus. This makes the restoring force negligible and there is no natural frequency. So, the Drude model for metals is derived by assuming $\omega_0 = 0$. Thus, the real part of the dielectric function becomes:

$$\epsilon_1 = 1 - \frac{\omega_p^2}{\omega^2 + j\omega\Gamma} \tag{2.54}$$

When the charges are free to move, they collide against one another and cause loss. Thus, it is often more meaningful to put equation2.54 in terms of 'mean collision rate, τ, also called momentum scattering time, when describing metals.

$$\epsilon_1 = 1 - \frac{\omega_p^2}{\omega^2 + j\omega\tau^{-1}} \tag{2.55}$$

where $\tau = \frac{1}{\Gamma}$

Dielectric contstant for metals in terms of real and imaginary components, according to Drude's model, can be written as:

$$\epsilon = \left[1 - \frac{\omega_p^2\tau^2}{1+\omega^2\tau^2}\right] + j\left[\frac{\omega_p^2\tau/\omega}{1+\omega^2\tau^2}\right] \tag{2.56}$$

In practice, metals are described in terms of real-valued permittivity and conductivity. Then

$$\epsilon_1 = 1 - \frac{\omega_p^2\tau^2}{1+\omega^2\tau^2}, \sigma = \frac{\sigma_0}{1+\omega^2\tau^2}, \tag{2.57}$$

where σ_0=$\epsilon_0\omega_p^2\tau$, called the DC conductivity.

From the typical Drude response in the figure 2.8, it is observed that below ω_p , the permittivity is negative and above ω_p it becomes positive. Whereas, the imaginary part of the permittivity is high below the ω_p, so the material is incredibly lossy, and above the ω_p, the material is not lossy at all. This is consistent when we discussed about Lorentz Model that above $\omega_p$materials tend to be transparent. From Graph b, below ω_p, absorption is really high and so is the real part of the refractive index. The material gets very lossy as we go down to DC, so much that no loss is experienced. The material parameters are so extreme, that when the wave encounters this material it actually reflects before it gets absorbed, so no absorption is experienced at all.

The following observations can be made from the above graph, above ω_p materials are transparent, however, below the ω_p they act as metals, with no sharp cut-off. Around

$\omega_p$metals are very lossy. Usually metals are very lossy near the optical frequencies and the ω_p for typical metals lies in the UV region. Below the ω_p, the dielectric constant is mostly imaginary and the metals behave like good conductors. Near the ω_p, both the real and imaginary part of the permittivity are significant and the metals are very lossy. This has been the biggest problem for optics and currently the first limitation for optical metamaterials.

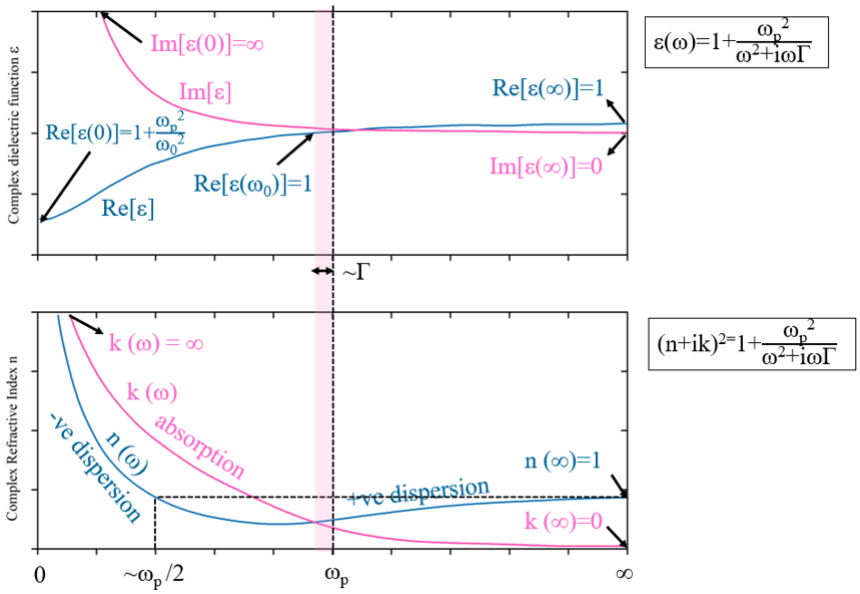

Figure 2.8: Typical Drude response for metals.

2.4.2 Anisotropic material

For anisotropic materials, the parameters such as permittivity, permeability and conductivity are directionally dependent. Because they vary in different crystal directions, they are treated as tensors. Anisotropic materials offer new and fascinating approach in engineering and technology. A few examples that show a significant improvement by using anisotropic materials are; a thin coating of anisotropic material would notably change the radar cross section of an aircraft, anisotropic composites have made their use in space shuttles and satellites, energy and opto-electronic devices also employ a vast range of anisotropic materials. Other applications include design with antenna patches where anisotropy is a employed as a major design parameter [52]. In electromagnetics, analytical solutions of wave propagation problems are confined to ordinary geometrical shapes [53, 54]. Material parameters (ϵ, μ, σ) for anisotropic materials like composites and crystals, are a function of vectors of electric and magnetic field direction. They are represented by 3×3 matrices for 3 dimensional structures.

$$\bar{\bar{a}} = \begin{pmatrix} a_{xx} & a_{xy} & a_{xz} \\ a_{yx} & a_{yy} & a_{yz} \\ a_{zx} & a_{zy} & a_{zz} \end{pmatrix} \tag{2.58}$$

where $a = \epsilon, \mu, \sigma$.

For anisotropic materials the constitutive equations now become

$$D = \bar{\bar{\epsilon}}\tilde{E} \tag{2.59}$$

$$B = \bar{\bar{\mu}}\tilde{H} \tag{2.60}$$

This means the electric and the magnetic fields are no more parallel to the electric and magnetic fluxes. The only exception being $a_{ij} = a$ for $i = j$ and $a_{ij} = 0$ for $i \neq j$. This also means that the refractive index depends on the field vectors, and the components a_{ij} are also frequency dependent functions with $a_{ij} \rightarrow a_{ij}(\omega)$ that follows Drude and Lorentz model.

This becomes of utmost importance for metamaterials introduced in the next section.

2.5 Understanding Metamaterials

The term metamaterial was first introduced in 2000 in the paper[29]. Here, we focus only on the materials that have phenomenal electromagnetic properties where the unit cell is relatively smaller to the wavelength[55]. It is worth knowing that the fundamental principle of metamaterials was discovered by the Russian physicist V. G. Veselago. He was the first person known to have noticed that Maxwell's equations do not eliminate the materials that have negative permittivity and permeability. The outcomes of reflection and refraction of electromagnetic waves with negative ϵ and μ materials were published published in 1968[56].

Before we begin to understand this, lets have a quick reminder on the physical relations that we studied previously in this chapter

- $n = \sqrt{\epsilon_r \mu_r}$, refractive index
- $c = 1/\sqrt{\mu\epsilon} = 1/\sqrt{\mu_0\mu_r\epsilon_0\epsilon_r} = c_0/\sqrt{\epsilon_r\mu_r} = c_0/n$, speed of light in a medium
- $\eta = \sqrt{\mu/\epsilon} = \eta_0 n/\epsilon_r$, impedance

Proposing a plane wave in equations 2.1 and 2.2 accounts for

$$k \times \tilde{E} = \omega B = \omega\mu\tilde{H} \tag{2.61}$$

$$-k \times \tilde{H} = \omega D = \omega\epsilon\tilde{E} \tag{2.62}$$

The above two waves provides information on the relative position of the vectors with each other. Here, $\tilde{E}, \tilde{H}, k$ are perpendicular to one another, however, their orientation relies on the sign of ϵ and μ. When $\epsilon > 0$ and $\mu > 0$ then the field vectors create a right handed system (RHS) where B becomes parallel to $\tilde{H}$ and D becomes parallel to $\tilde{E}$. Such

a material is called right handed material (RHM). When $\epsilon < 0$ and $\mu < 0$ then the field vectors create a left handed system (LHS) where B becomes anti parallel to H and D becomes anti parallel to $\tilde{E}$. Such a material is called left handed material (LHM). When $\epsilon < 0$ and $\mu < 0$ the materials are referred as 'double negative' (DNG), and when $\epsilon > 0$ and $\mu > 0$ the materials are referred as 'double positive' (DPS). Also, when either one of the parameter is negative, the material is 'single negative' (SNG) or 'epsilon negative' (ENG) or mu negative (MNG). For a DPS or DNG, the Poynting vector is defined as $S = (\tilde{E} \times \tilde{H}) = 1/(\epsilon\mu)(D \times B)$, which represents that the energy flux constantly points in the same direction. Waves that have wave vector pointing in the opposite direction to Poynting vector are called the backward waves. Figure 2.9 represents a clear difference between RHM and LHM.

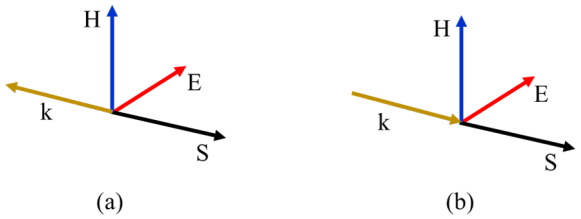

Figure 2.9: A clear illustration of (a) Left Hand Material (LHM); (b) Right Hand Material (RHM)

2.5.1 Negative index of refraction

Using boundary conditions and the definitions for the TE and TM modes, we can derive the continuity condition for the wavevector. In case of a TM mode, H_z is zero for the wave propagating in z direction, this leads to $H_t = H_y$, $H_n = H_x + H_y = 0$, 't' is tangential and 'n' is normal. For ease, the interface is defined at z = 0. Inside the material, the magnetic field is referred as H_2 and H = H_1elsewhere. H_y is considered a plane wave and is the sum of the incident and the reflected wave while $H_{2,y}$ has the transmitted wave traveling in the z direction.

$$H_y = Ae^{-i(k_z z + k_x x)} + Be^{i(k_z z - k_x x)} \tag{2.63}$$

$$H_{2,y} = Ce^{-i(k_{2,z} z + k_{2,x} x)} \tag{2.64}$$

where A, B, C are the amplitudes. Using the boundary conditions in 2.12 and that the boundary has an origin at $z = 0$

$$H_t = H_{2,t} \tag{2.65}$$

$$(A + B)\, e^{-ikx} = Ce^{-k_{2,x} x} \tag{2.66}$$

This condition can be achieved only if $k_x = k_{2,x}$ and A + B = C. The same logic exists for a TE mode with a tangential electric field. When the second material is is LHM,

the wavevector in this material $k_2$is antiparallel to the wavevector in the RHM with k. $k_x = k_{2,x}$ condition is still valid so k has to be negative for a wave with k_3 wavevector that is refracted above the perpendicular as seen in figure 2.10. This is know as the negative refraction.

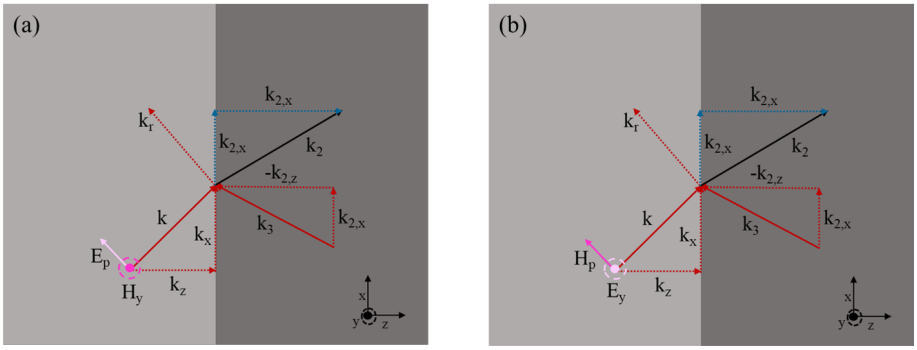

Figure 2.10: A clear illustration of (a) p-polarised wave; (b) s-polarised wave.

For deriving Snell's Law, $k_x = k_{2,x}$ condition with $k_x = k\sin(\theta)$ and $k_{2,x} = k_2\sin(\theta_2)$ requires to be satisfied. The dispersion relation $\omega = k/\sqrt{\epsilon\mu}$ leads to

$$\sqrt{\epsilon\mu}\sin(\theta) = \sqrt{\epsilon_2\mu_2}\sin(\theta_2) \tag{2.67}$$

$$\Leftrightarrow n\sin(\theta) = n_2\sin(\theta_2) \tag{2.68}$$

In case of negative refraction θ' becomes negative. Using the condition $\sin(-\theta_2) = -\sin(\theta_2)$ and substituting it in equation 2.68 and rearranging leads to

$$n_2 = n\frac{\sin(\theta)}{-\sin(\theta_2)} \tag{2.69}$$

But here equation 2.68 is disobeyed as $n\sin(\theta) = -n_2\sin(\theta_2)$ and hence n_2 has to be negative.

Further investigating the index of refraction, defined as $n = \sqrt{\epsilon\mu}$. In this definition for the index of refraction to be negative ϵ and μ have to be complex numbers for LHM. Same as describe in section 2.3, n' features the classical index of refraction and n'' the absorption.

$$n^2 = \epsilon\mu \tag{2.70}$$

$$\Leftrightarrow \left(n' + ik^2\right)^2 = (\epsilon' + i\epsilon'')\,(\mu' + i\mu'') \tag{2.71}$$

$$\Leftrightarrow n'^2 - k^2 + i2n'k^2 = \epsilon'\mu' - \epsilon''\mu'' + i(\epsilon'\mu'' + i\epsilon''\mu') \tag{2.72}$$

Everything derived until now is valid for the real parts of the quantities considered $\epsilon' < 0$, $\mu' < 0$, $n' < 0$. Now, by taking only the imginary part of the equation 2.72 we get,

$$\mathrm{n}' = \frac{\epsilon'\mu'' + \epsilon''\mu'}{2k} < 0 \tag{2.73}$$

k corresponding to absorption is > 0. Hence the condition remaining is

$$\epsilon'\mu'' + \epsilon''\mu' < 0 \tag{2.74}$$

2.6 Evanescent Waves

Let us consider a plane wave propagating in the x-direction in a medium with n as the index of refraction.

$$\tilde{\mathrm{E}}(\mathrm{x},\mathrm{t}) = \mathrm{E}_0 e^{-\mathrm{i}(k\mathrm{x}-\omega\mathrm{t})} \tag{2.75}$$

where E is the electric field vector, E_0 is the constant electric field vector amplitude, k is the propagation coefficient, and x is the position vector.

Using the dispersion relation

$$k = \frac{\mathrm{n}\omega}{\mathrm{c}_0} = (\mathrm{n}' + \mathrm{i}k)\,\frac{\omega}{\mathrm{c}_0} \tag{2.76}$$

substituting equation 2.76 in equation 2.75 gives

$$\mathrm{E}(\mathrm{t},\mathrm{x}) = \mathrm{E}_0 \mathrm{e}^{-\mathrm{i}\left(\frac{\omega}{\mathrm{c}_0}\mathrm{n}'\mathrm{x}-\omega\mathrm{t}\right)} \mathrm{e}^{-\frac{\omega}{\mathrm{c}_0}k\mathrm{x}} \tag{2.77}$$

where k will lead to an exponential decay of the incident wave. Now, linking the imaginary part of the refractive index to equation 2.35 Beer Lambert's Law, the intensity of the electric field that is proportional to the square of the field leads to

$$\mathrm{I} \propto |\,\tilde{\mathrm{E}}\,|^2 = \mathrm{E}_0^2 \mathrm{e}^{-\mathrm{i}2\left(\frac{\omega}{\mathrm{c}_0}\mathrm{n}'\mathrm{x}-\omega\mathrm{t}\right)} \mathrm{e}^{-2\frac{\omega}{\mathrm{c}_0}k\mathrm{x}} = \mathrm{I}_0 e^{-2\frac{\omega}{\mathrm{c}_0}kx} \tag{2.78}$$

where the term $\mathrm{E}_0^2 \mathrm{e}^{-\mathrm{i}2\left(\frac{\omega}{\mathrm{c}_0}\mathrm{n}'\mathrm{x}-\omega\mathrm{t}\right)}$gets absorbed in I_0. On comparing the coefficients of equation 2.35 with equation 2.78 leads to

$$\alpha = \frac{2\omega k}{\epsilon_0} \tag{2.79}$$

Till here, investigation of wave propagation in RHM ($\epsilon, \mu > 0$) and LHM ($\epsilon, \mu < 0$) is done. Now let us see in case of $\epsilon < 0, \mu > 0$ or $\epsilon > 0, \mu < 0$. Again using the dispersion relation here, leads to

$$k = \omega\mathrm{c} = \omega\mathrm{n} = \omega\sqrt{\epsilon_0\mu_0}\sqrt{\epsilon\mu} \tag{2.80}$$

In case of $\epsilon < 0, \mu > 0$ or $\epsilon > 0, \mu < 0$, k has to be a complex number $k = k' + \mathrm{i}k''$. Then for the plane wave propagating in x direction, the electric field is

$$\tilde{\mathrm{E}}(\mathrm{t},\mathrm{x}) = \mathrm{E}_0 \mathrm{e}^{-\mathrm{i}(k\mathrm{x}-\omega\mathrm{t})} = \mathrm{E}_0 \mathrm{e}^{-\mathrm{i}(k'\mathrm{x}-\omega\mathrm{t})} \mathrm{e}^{k''\mathrm{x}} \tag{2.81}$$

Here the term $e^{k''x}$ causes an exponential decay in the x direction, hence the penetration depth becomes limited. Such kind of a wave is called an evanescent wave. A sketch of reflection and transmission properties of distinctive material parameters is illustrated in figure 2.11.

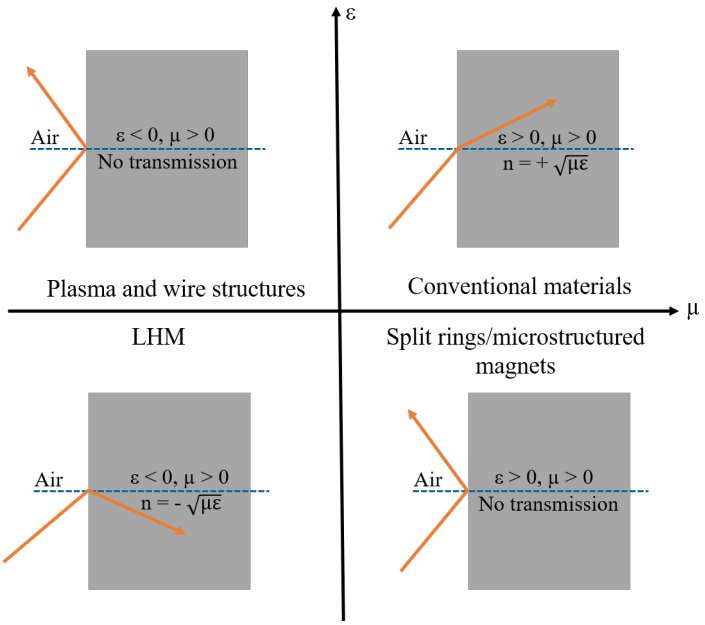

Figure 2.11: Depiction of different material parameters show casing reflection and transmission properties.

2.7 Resonators

2.7.1 Electric wire grid resonator

So far no DNG materials have been discovered naturally. However, in 1999 Sir J. Pendry [ref101] built a LHM by combining two different structures. By assembling wires with split rings, a structure would be created where one component would lead $\mu < 0$ and the other would lead $\epsilon < 0$. These inclusions would be chosen on a mesoscopic scale where dimensions of the structure are smaller compared to the wavelength but larger than the atoms.

- **Wire Grid Resonator**

In accordance with the Lorentz model $\epsilon(\omega) < 0$ near the resonance frequency. There is not dielectric material known with the similar property. However, many metals have this property as metals are depicted using Drude model where the conducting electrons are unbound and free to move. As shown in figure 2.8 negative ϵ exists for angular frequencies smaller than ω_p. Because of the absorption a small band is used for forming a negative index of refraction that can be manipulated by tuning the ω_p by altering the charge density. But it is not simple to generate the plasma and tune the position of the charges. For this Sir J. Pendry planned to combine the long wires of metal that seems as

an effective electron plasma to an incoming electromagnetic wave. The electric field would be polarised along the wires, and allows the materials with negative ϵ in the frequency range below 2GHz.

- **Cut wire grid Resonator**

To expand the bandwidth of the short wires their resonant behaviour can be used. In this case, the Drude model is not worthy because the ideal plasma assumptions do not hold true for short wires. In short wires the electrons are accumulated on the edges of the creating an opposing field that generates force proportional to the deflection. This force is dependent on the length of the wire. To boost the efficiency of such wire grid resonator, the cut wire grid method is proposed.

Here, the wires behave as inductors and the edges as capacitors. In the figure 2.12 a clear comparison between wire and cut wire is shown for μ and T. In case of cut wire, the frequency band is widened from ω_0 to ω_p due to the resonance, whereas, T for wire decreases exponentially. Such cut wire materials have many fascinating applications for DNG materials and also for horn antennas[57].

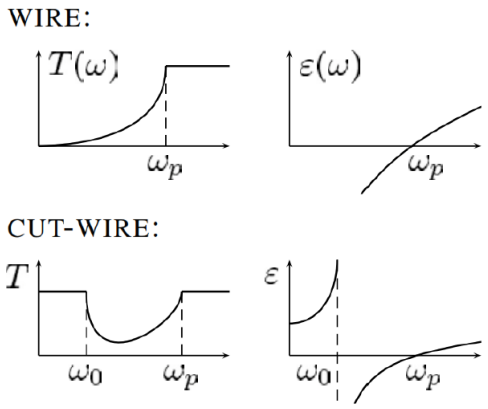

Figure 2.12: Transmission and permittivity of a wire and a cut wire[4].

2.7.2 Magnetic resonator

On a microscopic scale, unpaired electron spins are a result of magnetism, whereas on a macroscopic scale the way to have the magnetic moment is to bend the metal wire in the form of a circle and apply current to it. The generated magnetic moment perpendicular to the plane of the wire is

$$\mathrm{m} = \frac{1}{2}\int_{\mathrm{V}} (\mathrm{r} \times \mathrm{J})\, \mathrm{dV} \tag{2.82}$$

where J is the current density and r is the radius.

According to Ampere's law, the time varying current induces the magnetic field leading to magnetic moment m.This magnetic moment is too weak so as for the electric case, m

may increase by making use of resonance, creating a design called the split-ring resonator. The split ring is not completely closed and causes capacitance C connected in series with the inductance L of the ring. The split ring resonators leads to μ of [58]

$$\mu(\omega) = 1 - \frac{\omega_{\mathrm{m}}^2 - \omega_0^2}{\omega^2 - \omega_0^2 + i\alpha\omega} \tag{2.83}$$

where $\omega_{\mathrm{m}}$is the magnetic plasma frequency that is equal to the plasma frequency. Split ring resonators have sharp resonance and is a suitable choice $\mu < 0$.

2.8 Effective Medium Theory-Deriving optical constants for a composite

For the modelling of an object, numerical methods need to create a mesh to represent the object. In order to capture all the events of interest, the mesh needs to be very fine and coarse to reduce the cost of computation. For finite difference time domain (FDTD) algorithm, the size of the mesh should be at least $\lambda/10$. It is not possible to model the entire room of interest, thus single unit cells correspond to the big structure are modelled. Modelling of every single unit cell separately is not possible, thus multiscale techniques are used to prevent the typical requirement of fine meshes and to minimize the enormous computational cost. The objective following these methods is to foresee the nature of any given material at a large scale by performing calculations on a small scale, as single unit cell for example. Multiscale techniques can be roughly be classified into two categories, analytical and numerical homogenisation techniques. The analytical technique are usually used for composites with two component but have their constraints for metamaterials. The numerical homogenisation technique can be divided into direct and indirect techniques. For a direct technique, the material parameters can be straight-away calculated from the electric and the magnetic fields by field averaging. This usually requires inverting the constitutive equations as suggested by Wu or Pendry [59, 28]. The indirect method generally involves the scattering parameters that are explained in annex6.1 in and an algorithm to retrieve the material parameters from the S-parameters also explained in annex 6.1.

In this section, I have explained shortly the analytical methods of homogenization.

2.8.1 Effective Medium Approximation (EMA)

EMA is a method of solving a macroscopic inhomogeneous medium, where quantities such as conductivity σ, dielectric function ϵ, or elastic modulus vary in space. The optical constants of two-phase nanocomposites can be resolved by significantly mixing the optical constants of the individual components of the composite by EMA theories. This work would be focused on metal-dielectric, consisting of combination of metallic and dielectric particles in ordered or random manner. If the average size of the inhomogeneities is much smaller compared to the wavelength of the incident light, then electric and magnetic field are regarded consistent over this length[60]. This is called quasi-static approximation, and

the condition for the use of EMA for the determining the optical constants of a composite. To use these theories for determining the effective dielectric function, ϵ_{eff} , of the composite material, it is essential to know the optical constants of the embedded particles, ϵ_{p}, and the host matrix, ϵ_{M}. The most commonly used EMA theories are; Mawell-Garnett[61] and Bruggeman[62], that are used to model dielectric functions based on their corresponding constituents, volume fraction and shape of the particles.

2.8.2 Optical constants from Maxwell-Garnett (MG) Model

To begin with the simplest EMA theory is the Maxwell-Garnett (MG) theory. This theory considers the metal to be dispersed inside the dielectric matrix with separate grain structure[61], without particle interaction, of the two components. Maxwell-Garnett is relevant to combinations where the volume fraction of embedded particles is low (f_{M}˂0.3). The equation for Maxwell-Garnett model is[61]:

$$\frac{\epsilon_{\text{effMG}} - \epsilon_{\text{D}}}{\epsilon_{\text{effMG}} + 2\epsilon_{\text{D}}} = \text{f}_{\text{M}} \frac{\epsilon_{\text{M}} - \epsilon_{\text{D}}}{\epsilon_{\text{M}} + 2\epsilon_{\text{D}}} \tag{2.84}$$

where, ϵ_{effMG} is the dielectric function of the metal-dielectric composite from the Maxwell-Garnett model, f_{M} is the volume fraction of the metallic component of the composite, indexed by M for the metal and D for the dielectric.

2.8.3 Optical constants from Bruggeman Model

The Bruggeman model assumes an aggregate structure of randomly intermixed particles of metals and dielectric. It is applicable to microstructures where the distributed particles are barely distinguishable from the host matrix. This theory has proven to be appropriate in the cases for percolated systems. The equation for the Bruggeman's model is[62]:

$$\text{f}_{\text{M}} \frac{\epsilon_{\text{M}} - \epsilon_{\text{effBR}}}{\epsilon_{\text{M}} + 2\epsilon_{\text{effBR}}} + (1 - \text{f}_{\text{M}}) \frac{\epsilon_{\text{D}} - \epsilon_{\text{effBR}}}{\epsilon_{\text{D}} + 2\epsilon_{\text{effBR}}} = 0 \tag{2.85}$$

where, ϵ_{effBR} is the dielectric function of the metal-dielectric composite from the Bruggeman model.

The Bruggeman theory aims to predict broader absorption curves compared to MG theory. For very low volume fraction (f_{M}˂0.3) Bruggeman theory is same as MG theory, where no percolation is considered. For determining the effective dielectric function of a composite, MG and Bruggeman theories does not explicitly depend on the size of these inhomogeneities. This is due to the fact that the electric dipole term, which is proportional to particle volume, is maintained in the series expansion of the amplitude of the electric field scattered by a single particle. Although, significant inconsistencies between experimental and simulation results are discovered when only volume fraction is considered to describe the micro-topology of a nanocomposite material[45].

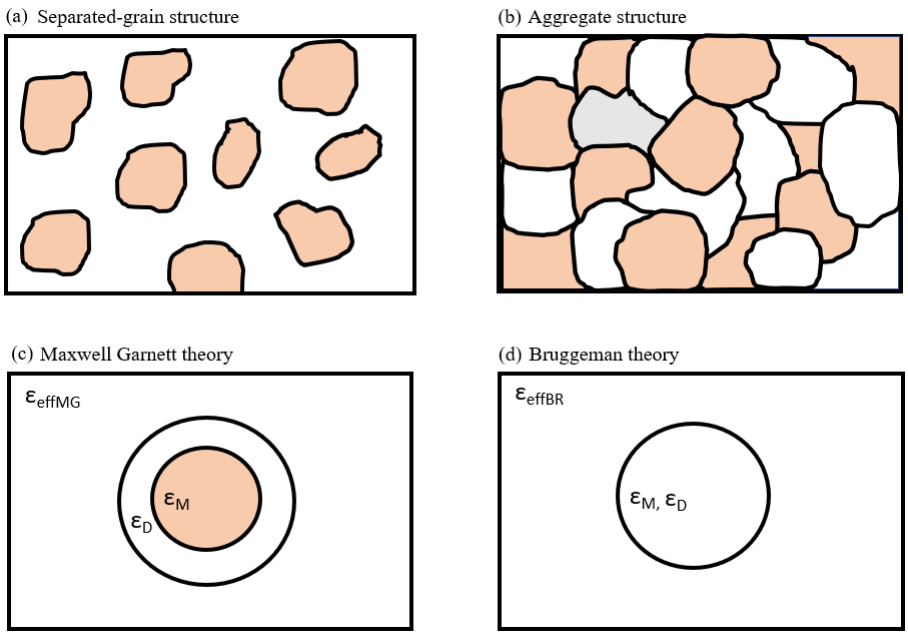

Figure 2.13: (a) and (b) illustrates the microstructures for heterogeneous two phase media; (c) and (d) indicates the corresponding random unit cells used to acquire the effective dielectric permeability within the Maxwell Garnett and Bruggeman theories.

2.9 Theory of thin film Optics

2.9.1 Single thin film and multilayer films

For the optical behaviour of a single homogeneous thin films, two boundaries are considered to understand its optical behaviour. The numbering of boundaries obeys the conventional rule i.e, counting from top to the substrate. As introduced in the previous sections, reflection and refraction of light occur when the light travels through different media. When two media are involved, at the interface, according to Snell's law of refraction:

$$n_1 \sin\theta_1 = n_2 \sin\theta_2 \tag{2.86}$$

The amplitudes of reflected, r,and transmitted, t, vectors are described by the Fresnel-coefficients[63, 64, 65] after applying the continuity interfaces conditions of Maxwell's equations:

$$r_\perp = \frac{n_1 \cos\theta_1 - n_2 \cos\theta_2}{n_1 \cos\theta_1 + n_2 \cos\theta_2} \tag{2.87}$$

$$r_{||} = \frac{n_1 \cos\theta_2 - n_2 \cos\theta_1}{n_1 \cos_2 + n_2 \cos\theta_1} \tag{2.88}$$

$$t_\perp = \frac{2 n_1 \cos\theta_1}{n_1 \cos\theta_1 + n_2 \cos\theta_2} \tag{2.89}$$

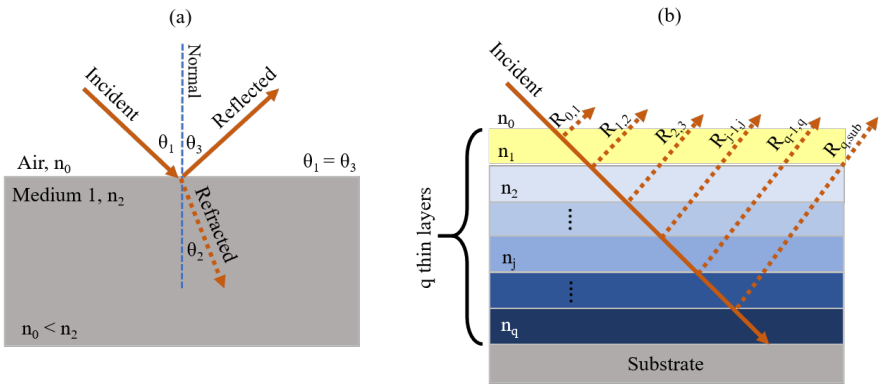

Figure 2.14: Schematics for the propagation of incident light beam through (a) two mediums (b) q multi thin layers deposited on a substrate (where the reflectance vector emerges from the j_{th}interface).

$$t_{\parallel} = \frac{2n_1 cos\theta_1}{n_1 cos\theta_2 + n_2 cos\theta_1} \tag{2.90}$$

where $\perp$, $\parallel$ are the perpendicular and the parallel interface vectors, respectively. For the normal incidence, $\theta_1,\theta_2,\theta_3$ all are equal to 0, the above equations can be simplified as:

$$R_N = \mid r_\perp r_\perp^* \mid = \mid r_\parallel r_\parallel^* \mid = \mid \frac{n_2 - n_1}{n_2 + n_1} \mid^2 = \frac{(n_2 - n_1)^2 + k^2}{(n_2 + n_1)^2 + k^2} \tag{2.91}$$

$$T_N = \mid t_\perp t_\perp^* \mid = \mid t_\parallel t_\parallel^* \mid = \left(\frac{2n_1}{n_1 - n_2} \right)^2 \tag{2.92}$$

where, $R_N$and T_N is the reflectance and the transmittance at normal incidence. These results can be generalized for $q$thin multilayers, using the matrix form. The terminology thin is significant for assumptions and calculations according to the interference theorems. If q are the number of thin films, then the total electric field for the q layers and the substrate in the matrix form is[66]:

$$\begin{pmatrix} E_0^+ \\ E_0^- \end{pmatrix} = \prod_{j=0}^{q} I_{j,j+1} L_{j+1} \begin{pmatrix} E_{sub}^+ \\ 0 \end{pmatrix} \tag{2.93}$$

where, $E_0^+$and $E_0^-$are the complex amplitudes of the forward and the backward traveling wave, respectively. $I_{j,j+1}$being the scattering matrix of the interface from j^{th}layer to $j^{th}+1$ layer, and $L_{j+1}$is the propagation matrix through the layer $j+1$.

Then the characteristic matrix for the whole system becomes[65]:

$$\begin{bmatrix} B \\ C \end{bmatrix} = \left\{ \prod_{j=1}^{q} \begin{bmatrix} cos\delta_j & (isin\delta_j)/n_j \\ in_j sin\delta_j & cos\delta_j \end{bmatrix} \right\} \begin{bmatrix} 1 \\ n \end{bmatrix} \tag{2.94}$$

where, $\delta = 2\pi ndcos(\theta)/\lambda$is the phase shift of the wave travelling a distance d normal to the boundary. $n_j$is the refractive index of the j^{th}layer and n_{sub} is the refractive index of the substrate. If the operator matrix is demonstrated as a product of operator matrices

of each of the layer, equation 2.94can be expressed as:

$$\begin{bmatrix} \mathrm{B} \\ \mathrm{C} \end{bmatrix} = [\mathrm{M}_1]\,[\mathrm{M}_2] \ldots [\mathrm{M_j}] \ldots [\mathrm{M}_{q-1}]\,[\mathrm{M_q}] \begin{bmatrix} 1 \\ \mathrm{n_{sub}} \end{bmatrix} \tag{2.95}$$

where C/B is the refractive index of the whole system i.e, the layers and the substrates. The total reflectance, transmittance and absorption of the entire system are given by:

$$\mathrm{R_N} = \left(\frac{\mathrm{n_0 B - C}}{\mathrm{n_0 B + C}}\right)\left(\frac{\mathrm{n_0 B - C}}{\mathrm{n_0 B + C}}\right)^{*} \tag{2.96}$$

$$\mathrm{T_N} = \frac{4\mathrm{n_0 Re}\,(\mathrm{n_m})}{(\mathrm{n_0 B + C})\,(\mathrm{n_{0+} BC})} \tag{2.97}$$

$$\alpha_{\mathrm{N}} = \frac{4\mathrm{n_0}\mathit{Re}\,(\mathrm{BC^{*} - n_m})}{(\mathrm{n_0 B + C})\,(\mathrm{n_{0+} BC})} \tag{2.98}$$

The numerical calculations for the optical constants n and k are governed by this system of matrices in the COMSOL Multiphyics software.

Chapter 3

Design, Working and Selection of materials for Spectral Selective Coatings

The part of this chapter written in italics has been taken from my manuscript [67] and [the paper under submission].

3.1 Different Designs for Spectral Selective Coatings for Solar Thermal Absorption

Selective solar absorbers have been classified into six types depending on their different designs: intrinsic, semiconductor-metal tandems, multilayer absorbers, multi-dielectric composite coatings, textured surfaces, and selectively solar-transmitting coating on blackbody like absorber. The schematics of these constructions are shown in the figure 3.1, and are discussed in greater detail below.

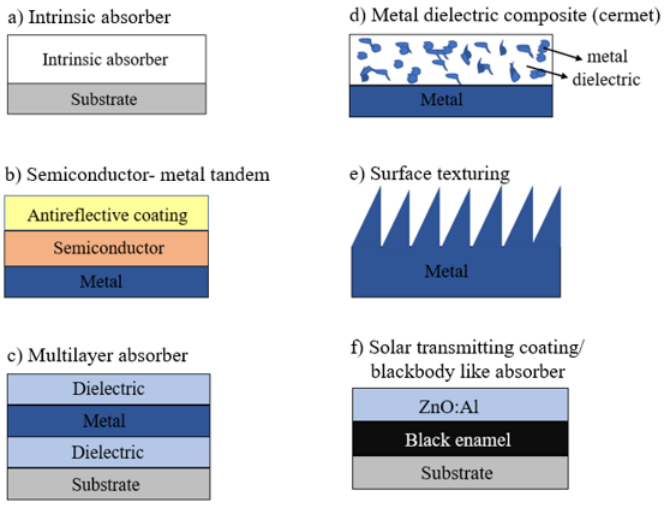

Figure 3.1: Schematics for different spectral selective coatings for solar thermal absorption.

(a) **Intrinsic absorbers (mass absorbers)**: this is considered as one of the most simplest and easy ways of selective coating production, where selectivity is the intrinsic property of the material i.e. absorptive in the solar spectrum and reflective in the far-infrared region. These types of absorbers are structurally stable but optically less effective

and hence, have lower efficiency compared to multilayer stacks that include, metallic W[41], MoO_3 – doped Mo[68], Si doped B, CaF_2, HfC, SnO_2, In_2O_3[41, 69].

Materials occurring naturally exhibit some roughly approximate selective properties, that need to be greatly modified to serve as an intrinsic absorbers. Transition metals and semiconductors fall in this category. Classically, research in intrinsic absorbers has not been very dynamic because there are no ideal intrinsic materials, hence these kind of absorbers are not ideal for solar applications.

(b) **Semiconductor-metal tandems**: semiconductors with bandgaps from $0.5 - 1.26$eV absorb light with short wavelength. These types of absorbers also indicate low emittance due to the underlying metal. so, these absorbers mainly constitute of semiconductors and an underlying metal layer, designed to minimize the thermal emission from heated substrates. Semiconductors that are usually used in these types of absorbers are Si(1.1eV),Ge(0.7eV) and PbS(0.4eV)[41]. The semiconductors used in here have high refractive indices, which results in high reflectance losses. Hence, antireflection coating are used for their better efficiency[46]. Si-based absorbers produced by chemical-vapor deposition (CVD) are well known in this category[68].

(c) **Multilayer absorbers**: these absorbers use the concept of optical interference to enhance absorption by alternating dielectric and metal layers. The thickness of the individual films in the coating are selected in such a way that, the light is transmitted through the coating and reflected from the dielectric/metal interface, to cause destructive interference with light reflected from the front surface of the film, increasing solar absorptance.

This interference effect may be optimized by several thin films to increase the number of reflections and maximize a. One example of these types of coatings is $Al_2O_3/Mo/Al_2O_3$triple layer absorber that was developed for US space project[70, 71]. The metals like Cr, W, Ti, Mo, Ag, Cu are usually sandwiched between the dielectric layers like $Al_2O_3$and AlN.

(d) **Metal-dielectric composite coating (Cermets)**: the word cermet comes from ceramic-metal composite. Composites are used extensively in various fields of application, occurring naturally or among engineered materials. Composites get their effectiveness from the combination of the properties of their constituent materials.

This type of coating constitutes of metal nanoparticles embedded in a dielectric or ceramic matrix, with ceramic characteristics in the visible spectrum and metallic in the IR. That means the cermet layer is transparent in the thermal IR region and strongly absorbs in the solar region. This happens due to the inter-band transition in the metal and the resonance of small particles in the cermet due to the plasmonic effect. The optical properties of the cermets can be intermediate between those of a dielectric and metal, with effective medium theory (EMT) predicting their optical performance. Cermet absorber coatings offer high degree of flexibility in terms of coating thickness, concentration of the particles, their position, shape, size and orientation[72, 73]. Other than alumina, which is a stable ceramic used at high temperature, SiO_2 and AlN are also used[74].

(e) **Textured surfaces**: surface texturing is one of the most common technique used to obtain the best spectral selectivity. The textured surfaces are rough, used for high solar absorbance by multiple reflections. The textured surfaces work like highly reflective surface in the IR region, and the emittance of such coatings can be administered by re-designing the microstructure of coatings. Well known textures include dendrite, needle-like and porous microstructures, with textured copper, nickel and stainless steel surfaces[75, 76] and dendritic tungsten[77] extensively used in practice.

(f) **Selectively Solar-transmitting coating on black-body like absorber**: these kinds of absorbers can have highly doped semiconductor over an absorber with long term longevity, like $SnO_2 : F, InSO_3 : Sn$ and $ZnO : Al$. Typical example of these kind of absorbers are low-temperature flat-plate collectors with black enamel as the absorber material[78].

3.2 Literature Survey

3.2.1 Cermets

There are two major classifications of spectrally selective solar thermal absorber coatings for high temperature applications ($> 400°C$). The first group is based on a multilayer structure absorber based on transition metal nitrides and oxynitrides. The second is based on cermets-based spectrally selective solar absorbers, the available tandems in the market. CSP technology use these absorbers for electricity generation.

Most of the designs available for the two kinds of optical stack undergo poor thermal stability from elemental diffusion between the different layers, when exposed to high temperature. A few examples of the studies stating this are; Liang et al. reported the occurrence of the element diffusion near the interface region, in interfaces SiO_2/CrO_x and CrO_x/CrN_x, and copper diffusion from substrate all over all the stacked layers[79]. Coa et al. confirmed the diffusion of atoms of iron from stainless-steel within the cermet layer forming a new phase of $FeWO_4$[80]. Kotilainen et al. studied the impact of temperature-induced copper diffusion on the deterioration of chromium oxynitride selective solar absorber coating. They reported the diffusion of copper starting from the substrate then reaching the coating and from the coating to the uppermost surface[81]. Wang et al. reported that their work improved the thermal stability of $W - Al_2O_3$ cermet absorber by adding Ti nanoparticles making it $WTi - Al_2O_3$. Doing this disclosed that partial oxidation of Ti atoms forms a protective layer that prevents diffusion of W element[82]. Zhang et al. through his work commented about the diffusion of $Cr, N$and O between the absorbing layer and Al substrate. They also observed defects in micro-structure in amorphous chromium nitride deposited on an aluminium substrate[46].

The list of host and inclusion materials used since decades along with their preparation method and thermal stability are mentioned in the table 3.1below. Materials like Cr_2O_3, Al_2O_3, AlN and SiO_2 have been mostly used as the host matrix. Metals like Cr, Ni,

Co, Ag, Mo, Cu, W, Pt, SS have been mostly used as inclusions. Stable oxide and nitride materials like Y_2O_3, HfN, ZrO_2 and TiN are yet to be widely investigated.

Matrix	Metal Inclusion	Preparation	Thermal Stability	Reference
Cr_2O_3	Cr	Electroplating	-	[83]
	Cr	Electroplating	350°C	[84]
	Cr	Electroplating	300°C	[85]
	Cr	Sputtering	300°C	[86]
	Cr	Sputtering	-	[87]
	Cr	Sputtering	-	[88]
	Cr	Sputtering	-	[89]
Al_2O_3	Ni	Anodization	250°C in air	[90]
	Ni	Evaporation	500°C in air	[91]
	Ni	Sputtering	500°C in air	[92]
	Ni	Solution-based method	300°C in air	[93]
	Co	Evaporation	-	[94]
	Ag	Sputtering	400°C in vacuum	[95]
	Mo	Sputtering	2hr at 800°C in vacuum	[96]
	W	Sputtering	580°C in vacuum	[97]
	Pt	Evaporation	-	[98]
AlN	W	Sputtering	500°C in vacuum	[99]
	W	Sputtering	-	[100]
	SS	Sputtering	500°C in vacuum	[101]
	SS	Sputtering	-	[102]
	Al	Sputtering	-	[103]
SiO_2	Cu	Evaporation	277°C	[104]
	Cu	Evaporation	-	[105]
	Ni	Evaporation	500°C in a vacuum	[106]
	Ni	Sputtering	-	[107]
	Mo	Sputtering	580°C in a vacuum	[108]
	Mo	Sputtering	2hr at 800°C in vacuum	[109]
MoO_3	Mo	Solution-based method	300hr at 250°C in air	[110]
ZrO_2	Zr	Sputtering	-	[111]
$SS-N$	SS	Sputtering	-	[112]

Table 3.1: Tables listing the materials used for cermets along with their preparation methods and thermal stability.

3.2.2 Metamaterials

Metamaterials have been extensively explored for enhancing sunlight in Photovoltaivcs[113, 114] and solar-thermal conversion[115, 116, 117]. Various structure-based, material-based and shape-based PMAs have been used sunlight harvesting at high-temperatures. Metals like Ti and W are used as noble metal PMAs to solve the problem of narrow absorption band and poor thermal stability at the same time. Due to the large impedance mismatch and high-loss PMAs suffer absorptance drop of around 30% in the visible range [118, 119]. Even after using anti-reflection coatings the absorptance of these PMAs drops significantly[80, 120]. Unconventional material-based approach utilizing amorphous carbon have been utilized as mid spacer but in this case α_S is below 80% [121]. The IR emission of noble metal PMAs increases drastically after introducing high-loss meta-atoms

and IR reflectors.

The table 3.2 shows a list of materials along with their shapes that are commonly used as PMAs.

Material	Structure	Thickness (nm)	Reference
$TiN/SiO_2/TiN$	Ring-like	240	[122]
$W/SiO_2/W/SiO_2/W$	Circular	450	[119]
$Ti/SiO_2/W$	Square	420	[118]
Au/C/Au	Square	435	[121]
Ni/Si	Pyramids	500	[123]
$W/SiO_2/W$	Cuboid	60	[124]

Table 3.2: Tables listing the materials commonly used for MMs along with the most preferred shapes and thickness.

In the direction of design of MMs, the existing MMs are mostly 2D. To expand the practical applications, it is important to move from 2D to 3D. However, this transformation is not easy. In the direction of fabrication, MM suffer a major setback. Out of many techniques used lithography is the technique best and mostly used for the fabrication of MMs. With complicated structures, the labour and the cost of the machine increases to a large extent.

With the aim of achieving spectral selective coating (SSC) with best efficiency and the one that is thermally and chemically stable at elevated temperatures, we will begin this chapter by explaining the kind of the spectral selective coating that we have chosen for this work, as well as the design selected for the coatings. We will then demonstrate the working of the picked design involving the role of individual components of the coating. At the end of the chapter we would describe the reasons for preferring the materials of the individual components of SSC.

3.3 Design and structure for SSC

In this work, an unconventional design methodology for solar selective absorber layers, with the intention of boosting light absorption efficiency, over a wide solar spectrum, beyond the current status will be investigated. We would demonstrate solar-thermal performance of a cermet based Plasmonic Metamaterial Absorber (PMA) by adopting a hybrid strategy where a new structure, material and shape would be explored.

Cermet coatings have been broadly investigated and are still being extensively researched for the past two decades, due to their applications in CSP systems affirming high solar absorptance, low IR emittance[78, 94] and good thermal stability at low-and-medium-temperatures[125, 80, 126, 120]. The details for cermet SSC has been already explained in section 3.1 of Chapter 2. Preparation of a cermet composite was chosen for this work so that it have ceramic characteristics in the visible spectrum and metallic properties in the IR. The constituents of the cermet, their size and shape, the thickness of the coating, and volume fraction of metal in the dielectric matrix, strongly affect the

ceramic and metallic characteristics across the solar and IR spectra. Similarly, PMA develop a new class of selective absorbers for high-temperature function where absorption is enhanced through strong localized surface plasmonic resonances (LSPRs) in the metallic nanoparticles[127, 128]. The detailed effects of all the above mentioned parameters will be explained in the section 4.4 of Chapter 5.

To meet the required characteristics of a SSC, preparation of several layers of metallic NPs embedded in a dielectric matrix, one on top of the other, making it a composite of a thickness of few hundred nanometers, was adapted. It is unachievable to have all the desired properties in a single material, this being the case, a composite is needed with a blend of properties of two or more materials. This composite would represent a fundamental element of a more complex structure, the emergence of the metamaterial. Producing an ideal metamaterial based selective absorber structure by placing an array of resonators, (which would be a combination of a loop and a dipole, omega shaped structure), on top this composite dielectric, would make this new nano–structured absorber (PMA) that have many benefits over conventional absorbers, including adaptability and frequency tuning. Figure 3.2(a, b) shows schematic illustration of the components present in SSA and the design of the unconventional metal-insulator based plasmonic metamaterial absorber adopted for this study, respectively.

In practical, absorbers do not make use of just one but several absorption mechanisms to achieve better selectivity, such as multilayer cermet-based absorbers comprising of multilayer stacks of metal-dielectric composite, and introducing plasmonic nano-structures to make metamaterials, in this study.

3.4 Working of the individual components

3.4.1 Metallic particles

The requirement of the metallic particles in the cermet, is high k. As the electromagnetic wave enters the composite and strikes the metallic particle, it absorbs some of the incident light because of high k and the rest of the light is reflected and reaches the other metallic particle. This particle also absorbs some of the light and reflects the rest of the light to the other, and this process goes on.

The appropriate volume fraction (vf) of metallic particles in the composite is of utmost importance for tuning the optical properties of the solar absorber layers. The nanoparticles scattered all over the composite will give more extinction cross-section to the entire structure of the absorbing layers. *The extinction cross–section, sometimes called the attenuation cross–section, [129], is the area which, when multiplied with the irradiance of electromagnetic waves incident on the unit cell, gives the total radiant flux absorbed by the unit cell. We define*

$$\sigma_{\text{ext}} = \sigma_{\text{sca}} + \sigma_{\text{abs}} \tag{3.1}$$

where, σ_{ext} *is the measure of the dissipation of light in a medium,* σ_{sca} *is the amount of light scattered inside the material by particles and* σ_{abs} *is the amount of light absorbed, as Joule loss, in the material.*

More nanoparticles present in the absorbing layers would connect to each other forming a large structure close to the wavelength, causing more reflection. Sub-wavelength inclusions of $\lambda/10$ provide substitutes to conventional approaches based on bulky optical components. Artificial structures made of sub-wavelength inclusions and metasurfaces carry remarkable optical and electromagnetic properties that are not attainable in naturally occurring materials. Below is the most fundamental aspects described in brief, of sub-wavelength structures based techniques, i.e., the localization of electromagnetic waves by artificially designed sub-wavelength structures constructed with metals and dielectrics.

In principle, wave behaviour between light and material can be interpreted using Maxwell's wave equation, which in most generalized case can be written as

$$\nabla \times \epsilon^{-1} \nabla \times \mathrm{E} = \mathrm{k}_0^2 \mu \tilde{\mathrm{E}} \tag{3.2}$$

$$\nabla \times \epsilon^{-1} \nabla \times \mathrm{H} = \mathrm{k}_0^2 \mu \tilde{\mathrm{H}} \tag{3.3}$$

where His the magnetic field and ϵ, μ and $k_0$are the relative permittivity, permeability, free space wavenumber, respectively. With some mathematical manipulation equation 3.3 becomes

$$\nabla \times \nabla \times \tilde{\mathrm{E}} + \epsilon \nabla \epsilon^{-1} \times \nabla \times \tilde{\mathrm{E}} = \mathrm{k}_0^2 \epsilon \mu \tilde{\mathrm{E}} \tag{3.4}$$

When both permittivity and permeability are constant, equation 3.4is reduced to the wave equation

$$\nabla^2 \mathrm{E} + \mathrm{k}_0^2 \epsilon \mu \tilde{\mathrm{E}} = 0 \tag{3.5}$$

For sub-wavelength structures with substantial difference of permittivity, permeability, and refractive index, waves in the adjoining domains interact dynamically with each other , hence the second term in equation 3.4could not be neglected. This term directed to many fascinating solutions of wave equations such as surface plasmons, strongly localized waves, and negatively refracted waves.

We know that collective excitation of free electrons at the metal-dielectric interface, i.e., surface plasmons polaritons (SPP) with a propagation constant of $\gamma = \mathrm{k}_0 \sqrt{\epsilon_\mathrm{m} \epsilon_\mathrm{d} / (\epsilon_\mathrm{m} + \epsilon_\mathrm{d})}$, play a key role in the light-matter interaction[130] with ϵ_m the permittivity of a metal and ϵ_d the permittivity of a dielectric. The effective wavelength of even (or symmetric) surface plasmon polaritons mode for a thin metal film with thickness d is described by

$$\lambda_{eff} = 2\pi/\gamma \tag{3.6}$$

$$\coth\left(\sqrt{\gamma^2-\epsilon_{\mathrm{m}}\mathrm{k}_0^2}\mathrm{d}/2\right)=-\frac{\epsilon_{\mathrm{m}}\sqrt{\gamma^2-\epsilon_{\mathrm{d}}k_0^2}}{\epsilon_{\mathrm{d}}\sqrt{\gamma^2-\epsilon_{\mathrm{m}}k_0^2}} \tag{3.7}$$

If the thickness of the film is much smaller than the wavelength, the optical performance can be conveniently explained using effective impedance and effective wavelength and can be relatively as[131]

$$\lambda_{\mathrm{eff}}=2\pi/\gamma=2\pi/\sqrt{\epsilon_{\mathrm{d}}\mathrm{k}_0^2+\left(\frac{2\epsilon_{\mathrm{d}}}{\epsilon_{\mathrm{m}}\mathrm{d}}\right)} \tag{3.8}$$

Definitely, the effective wavelength can be largely reduced by either decreasing the film thickness or by increasing the permi<w<ttivity of the dielectric. This is different from the odd (antisymmetric) surface plasmons polaritons mode, where the propagation constant decreases with film thickness.

Besides metal film, a metal-insulator-metal waveguide is also used to transport and localize light wave with a horizontal dimension considerably smaller than the wavelength[132, 133]. The antisymmetric mode has a larger propagation constant compared to the symmetric mode, which is calculated using a slight change of equation 3.7

$$\tanh\left(\sqrt{\gamma^2-\epsilon_{\mathrm{d}}\mathrm{k}_0^2}\mathrm{d}/2\right)=-\frac{\epsilon_{\mathrm{d}}\sqrt{\gamma^2-\epsilon_{\mathrm{m}}k_0^2}}{\epsilon_{\mathrm{m}}\sqrt{\gamma^2-\epsilon_{\mathrm{d}}k_0^2}} \tag{3.9}$$

3.4.2 Dielectric thin films

The dielectric thin films would be the matrix for the absorbing metallic particles. The most fundamental requirement for the matrix is to be non-conducting, i.e, a host with zero electrical conductivity σ and high thermal conductivity κ.

When the metallic particle absorbs the incident light, its temperature is increased and the heat is generated. The dielectric matrix helps in transferring the generated heat down to the sink for the concerned application.

3.4.3 Metallic structure omega (Emergence of a metamaterial)

A layer of periodic metallic nano-structures is added on top of a cermet in order to achieve a near unit absorption by manipulating local magnetic and electric pole resonances of the meta-structure, transforming the cermet into a metamaterial absorber (PMA). To develop this metamaterial, both the individual unit cell that contains the included periodic resonator and the full-scale system needs to be considered. These absorbers uses localized surface plasmons polaritons (LSPPs) with a concept of metamaterial to achieve sufficient performance with smaller absorber volumes and design flexibility along with the materials used. Localised surface plasmon resonance (LSPR) are collective electronic excitation in metallic nanostructures[134, 135]. The properties like LSPR spectral peak position and resonance strength of plasmonic metamaterial strongly depends on the size, material and shape of the meta-atoms. Plasmonic nanoparticles with sharp corners, compared to

square or circular nanoparticles, show larger bandwidths in absorption cross-section[136, 137, 138].

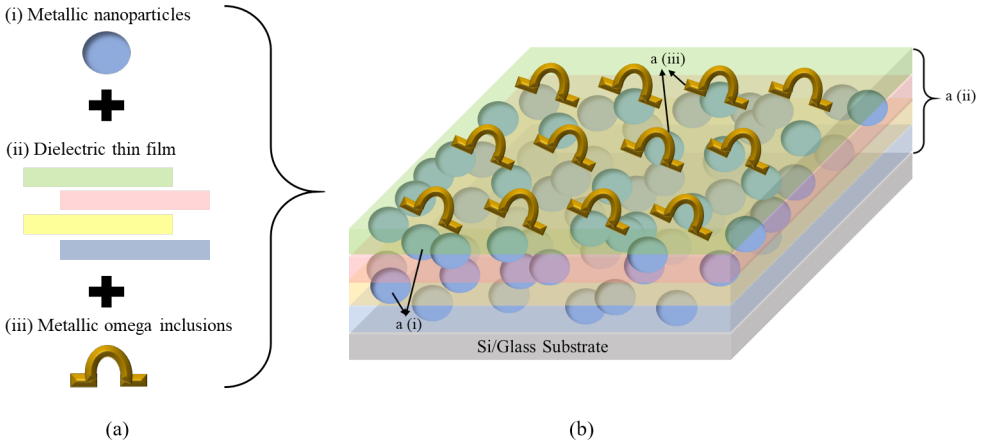

Figure 3.2: (a) The individual components of the structure of SSC. (b) Schematic of the complete design and structure of SSC showing its horizontal section with all the components included in it.

In this work, we decided to build our metamaterial based on metallic omega inclusions for the following two reasons. First, it is a moderately simple structure because the split ring and the wire are integrated into one structure and are not structurally separated like the metamaterial designed by Smith[29]. Second, the existence of the band gap of a single unit call is due to electric and magnetic resonance since omega structures have bi-anisotropic properties. This shape also leads to the coupling of electric and magnetic field the unit cells are arranged properly. The work on this shape was carried out by [139]. The effects of different kinds of omega inclusions concerning the size and orientation on the transmission and reflection is mentioned in the publication by Aydin[140, 141] and Li[11, 93]. The equivalent circuit diagram in the figure 3.3(b) has been analysed to understand the working and the physical mechanism of the proposed omega structure. This structure is divided into three parts with a ring, horizontal arms and a gap between the arms illustrated in the figure 3.3(a). To better understand, the ring and the horizontal arms create inductive effects defined as L_{Ring} and L_{Arm}respectively. The gap demonstrated as C_{Gap}creates a capacitive effect. Hence, an equivalent circuit diagram for the omega structure has been obtained as an LCR circuit shown in figure 3.3(b).

Expecting the best properties from the proposed structure and design of the above explained SSC, it is important to understand the working of the individual components of the SSC, described above. To summarize, it is predicted to have the conductivity of the composite between the conductivity of the fill particles and the dielectric matrix i.e, high k, low σ and high κ in the same composite.

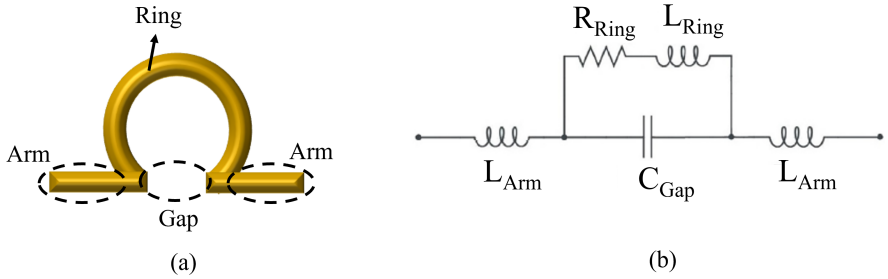

Figure 3.3: (a) Different parts of the omega structure. (b) Equivalent LCR circuit diagram of the omega structure.

3.5 Need for a composite

When designing an ideal selective solar absorber we choose material such that the refractive index, n, *is close to that for air, over the visible range spectrum to reduce reflection and higher in the infra-red region to cause more reflection at the interface. Figure 3.4 shows the refractive index functions of composite phases.* AlN *curve shows no dispersion over the* VIS–IR *spectrum e.g.,* n *is constant and no loss with* k *null. This makes these materials very transparent to light.* TiN *is, however, conductive with high loss, dispersive and the refraction index is close to unity is* VIS *while increasing high for* IR *region. When designing the composite dielectric* TiN/AlN, *we ensure that the* TiN *nanoparticles do not reach the percolation limit, so that any agglomeration will not cause large reflection in the* VIS *region, while smaller particles increase the scattering extinction, Striebel et al. [142].*

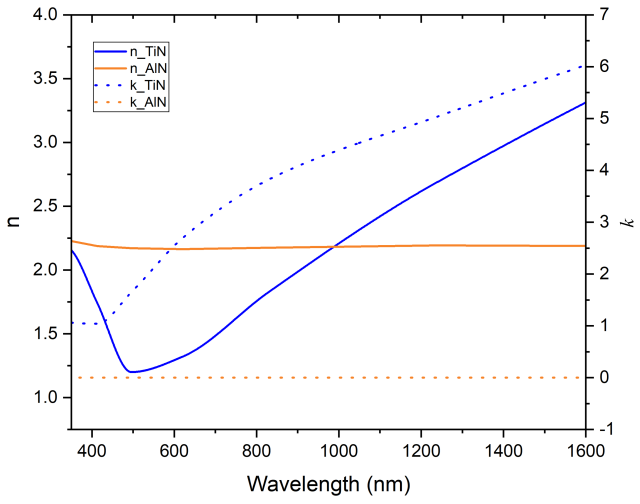

Figure 3.4: Refractive index n and extinction coefficient k for TiNand AlN.

The ideal selectivity of the SSCs cannot be achieved only with the composite therefore metamaterials (addition of omega structure on top of the composite) improves the selectivity of the SSCs. The addition of omega structures to the metamaterial do not

add an additional feature to the SSCs but enhance the filter property and thus improves selectivity.

3.6 Selection of materials

For high operating-temperature of CSP applications, achieving a SSC with good thermal stability and high efficiency remains a primary challenge. One strategy is to explore new materials for metallic inclusions, dielectric and plasmonic metallic structure (the array of which creates a metamaterial). Table 3.1 and 3.2 in Chapter 2 shows various materials that are in trend for cermets as well as PMA respectively, and our reasons for choosing the materials of our interest are clearly mentioned below.

3.6.1 Important properties of the materials

There are various properties of interest that are expected from the materials for the best performance of the SSC, and considering all those properties the following materials were chosen.

3.6.1.1 Metallic particles

Considering all the above mentioned properties required in a SSC, Titanium Nitride nanoparticles (TiN) NPs were preferred as metallic inclusions in the matrix. TiN possesses all the properties of a metal, and is an extremely hard ceramic material. Its hardness is a benefit for the durability of the coatings at high temperatures. TiN has gained much attention in the context of materials for CSP, due to its peculiar properties, particularly its high chemical and thermal stability, together with its low electrical resistivity. In addition, its high melting point (2930°C) and high hardness of TiN also make it an ideal material to be embedded into a dielectric matrix for CSP applications[143, 144, 145, 122]. Moreover, it has been reported that TiN is an excellent candidate for high–temperature plasmonic applications, while conventional plasmonic materials like gold and silver are not suitable because of their relatively low melting point and softness[143, 145, 146].

3.6.1.2 Dielectric thin films

For the dielectric matrix, Aluminum Nitride (AlN) is preferred over all the other insulators. This is because AlN is known to provide hard coatings, that are chemically and thermally stable at elevated temperatures. It has a wide band gap $(6.0 - 6.2\text{eV})$[147, 148]and is transparent in the visible region of the spectrum. It has high thermal conductivity, $70 - 210\text{Wm}^{-1}\text{K}^{-1}$for polycrystalline material, and as high as $285\text{Wm}^{-1}\text{K}^{-1}$for single crystals)[149] and a high melting point (2200°C). In air, the oxidation of AlN is known to occur at (700°C). At room temperature, surface oxide layers of $5 - 10\text{nm}$ have been reported, that protects the AlN material up to 1370°C. Thus, it is suitable as a dielectric matrix for CSP applications[150, 151].

3.6.1.3 Plasmonic Metamaterials

Like Gold (Au) and Silver (Ag), Platinum (Pt) also exhibits superior plasmonic properties[152, 153], and hence are utilized in improving the performance of the devices with suitable optical, electric, magnetic and catalytic properties. The aim of this study includes dynamic LSPR characteristics from the omega structures creating a metamaterial, for better performance of the SSC. For this reason Pt was chosen for creating the metallic omega structures on top of the composite.

Other than this, this study also concentrates on the working of the SSC at elevated temperatures, thus it became of extreme importance to look for a metal that show both, outstanding plasmonic properties and high melting point. Compared to other plasmonic metals like Au and Ag, Pt has comparatively higher melting point of 1768°C and this would definitely be advantageous while concentrating on the working of SSC at temperatures of 1000°C.

3.6.2 Thermal and chemical stability of the materials

Apart from the properties of interest that are mentioned above, thermal and chemical stability play a vital role in the performance of SSCs. Interface stability becomes crucially important when the focus of the work is towards the multilayer composites and its performance at elevated temperatures. A thorough literature survey was done for this purpose.

3.6.2.1 Metallic (TiN) nanoparticles

In a work proposed by Nikhil P. et al in the year 2014 on post deposition annealing of TiN thin films, it has been clearly stated that TiN thin films possess good thermal, electrical and morphological stability when heated at 500°C, 700°C and 900°C. They also stated that XPS results of the films annealed at such high temperatures, had all TiN phases, clearly indicating the stability of the films[154]. In 2014 Wei L. et al investigated the thermal stability of the TiN metamaterial absorber and made a comparison with Au metamaterial absorber. It was seen that when TiN metamaterial absorber was heated at 400°C, 600°C and 800°C for 8 hours, neither the shape, the size nor the absorbance of the structure changed. The Au metamaterial absorber was treated in a similar manner and it was observed that the Au structure melted into NPs just after 15 min of annealing. This can be described by the fact that bulk TiN has a melting point of $2930^{\circ}C$ which is much higher that that for Au, 1063°C. It was also seen that the absorber made of Au can only withstand a temperature as high as 600°C[122]. In a recent work by Tobias K. et al an investigation on the oxidation behaviour at 1000°C under medium vacuum conditions and thermal stability at 1400°C under high vacuum condition was done. An exceptional structural stability and thermal stability was seen when TiN films were heated for 2hours and 8hours, respectively, without any protective coating layer. The author also revealed that to his knowledge it is the first time that TiN film structure exhibited

remarkable thermal stability at such high temperature[155]. Now, talking about the stability of TiN powder Chunhong G. et al reported a method for synthesizing TiN NPs in flowing ammonia at 900°C for 4hours. This confirms that TiN NPs can withstand this temperature[156].

Current research suggests that the prime properties, such as conductivity and permittivity, of TiN changes narrowly with temperature[157, 158]. These findings unlatch the fundamental understanding of the TiN at extreme temperatures and presents a possibility of a promising candidate for high temperature applications in harsh environments.

3.6.2.2 Dielectric (AlN) thin films

V. Moraes in 2016 confirmed that AlN thin films were grown by varying the substrate temperature from 250°C to 800°C with a step of every 100°C, could sustain texture and thermal stability at all the temperatures[159]. In a work by Keltouma A., it was observed that AlN thin films could tolerate temperature up to 1000°C. Though the upper surface was oxidized, but was protected with ZnO against surface oxidation[160]. The oxidation of AlNthin films plays a crucial role in the determining the stability of the films, and thus affects the overall performance of the device. A lot of work has been carried out on thermal stability and oxidation of AlN films since past few decades. In a work by F. Ansart in 1994, a detailed report on the oxidation of AlN thin films was published, where the deposited films had excellent thermal stability until 850°C and did not undergo any kind of chemical and physical alteration. The author explained in this work the existence of oxygen at 1000°C, and above 1100°C the oxidation of the films progresses rapidly[161]. In a similar work by C. Labatut, the oxidation behaviour of AlN films were studied between the temperature range 1000°C to 1400°C. Oxidation was only detected above 1000°C, where compounds like AlO_xN_y and Al_xO_ywere formed. Apart from this the films were structurally and thermally stable[162].

The additional excellent thermal, chemical stability and high mechanical properties of AlN thin films is an extraordinarily attractive combination for highly sophisticated applications, like thin films for solar-thermal absorption, that can withstand rough temperature conditions.

3.6.2.3 Metallic (Pt) Metamaterial

In a work by M Rauber in 2012, an insight into the thermal stability of Pt nanowires was presented. The Pt nanowires of 74nm did not decay until 900°C and assured adequate durability of the Pt nanowire-based devices[163]. Beck in 2014 compared the thermal stability of Pt thin films with Ag thin films and Pd thin films. She reported that at temperatures of up to 750°Cthe Pd thin films were most stable and hence widely used in metal electrodes[164]. In another work, thermal stability for Pt NPs was checked by Ying where Pt NPs on the surface of pristine GO were found to be thermally stable at 700°C[165]. In a recent work by Samadi in 2018, Pt NPs were proved capable of reaching

the thermal stability at 700°C while maintaining its structural integrity . Pt NPs were also proved better thermally compared to other metallic nanoparticles[166].

Though none of the above works concentrated on Pt MM, but they were good enough to prove the thermal stability of Pt nanostructures at high temperatures.

Chapter 4

Solar Selective Coatings: A Methodology for a complete design

The part of this chapter written in italics has been taken from my manuscript [67] and [the paper under submission].

4.1 Numerical Solution of Maxwell's Equations

In computational electromagnetics (CEM) there are various methods of solving Maxwell's equations. All these methods have their own advantages and disadvantages depending on various cases where one method is a benefit over the other. Here is a review of various numerical techniques for the solution of Maxwell's equations.

- **Time Domain vs Frequency Domain**

CEM can be divided in two categories: Time domain (TD) and Frequency domain methods. Time domain methods are mostly used if a broadband analysis is needed. An example would be an electromagnetic pulse in time domain, interacting with a dielectric material, with their transmission and reflection coefficients indicated in the frequency domain. On this account, a pulse is explained in the time domain and after it interaction with the dielectric, the Fourier transform is applied to change the response from the time to frequency domain. The outcome is a very broadband response in the frequency domain by running the algorithm only once in time domain. If on the contrary, we are only focused on a time-harmonic steady state solution at only one frequency, the frequency domain method is much more effective because no time stepping is required and the result is obtained by a process of matrix inversion. An additional profit of a frequency domain method is its clarity to implement frequency dependent (dispersive) material parameters (ϵ, μ, σ) as the scalar values can be used directly. This is complicated to be achieved in time domain because the fundamental equations, which is a multiplication in the frequency domain, grows intricated in the time domain. Obtaining a broadband response in a frequency domain method can also be done by running numerous simulations, one at each frequency.

- **Boundary Element Method (BEM) or Method of Moments (MoM)**

The boundary element method or the method of moments are the methods used to solve partial differential equations that are defined as integral equations. The practice of this method ranges from electromagnetics to acoustics and fracture mechanics. This method became popular in late 1970s but its implementation started in the 60s. The major difference between this method and the presented finite difference and finite element methods is that BEM/MoM is the boundary method whereas others are the domain methods. In the case of BEM/MoM, for a three dimensional case, the discretisation is applied only to the boundary surface, whereas in domain methods, it is applied to the entire space. This leads to lower dimensions and further lower computational requirement due to smaller systems. Therefore, this method is applicable to the problems with small surface to volume ratio and when the geometry includes large metallic surface or resonant length wires. If the size of the obstruction is much bigger than the incoming wavelength then this method is typically used. In this work, we are interested in objects with a size in the order of magnitude of the exciting wavelength, making this method not applicable for our applications. Usually BEM method results in completely populated matrices, needing a lot of storage requirement, and the computational time proportional to the square of the problem size whereas, for Finite Element Methods the storage requirement grows linearly with the problem size [167]. BEM method is more sorted for problems in linear homogeneous media where Green's function can be calculated, which is considered a non-negligible restriction for our application and thus, we concentrate on methods with volume discretisation.

- **Finite Difference Time Domain Method (FDTD)**

The publication from Courant, Firedrichs and Lewy from the year 1928 can be considered as the beginning of Finite Difference Method [168]. They explored the solution of problems by a process of finite different methods. They also explained a finite difference approximation for the wave equation, and the defined the CFL stability condition that is necessary for the convergence of a solution. This condition is an important parameter in the FDTD formulation as it couples the time step with the spatial step of the mesh. Gerschgorin, in 1930 [169] derived the error bounds for the different approximation of elliptic problems. Many years later with the betterment of computers came the practical applications pushing the development of FDTD method. O'Brian, Hyman, Kaplan [170], John [171] during the 1950s and 1960s were among the many other key protagonists that further lead to the development and generalisation of the method. The most accepted FDTD method in electromagnetics is the Yee algorithm [172] that is named after the inventor Kane S. Yee. Some of the major advantages of this methods are[30][173] : easy discretisation process that permits a 3D problem to model with short lines of code that makes it easy to comprehend; no inherent limit required for the size of simulation due to its explicit nature, no linear algebra or matrix inversions are required; the scheme holds the energy and amplitude of the wave; being a time domain method, simulation with a single run allows the entire representation of frequency domain by using Fourier

transform; precise and powerful method that can be effortlessly be parallelized on CPU's and GPU's. The major drawbacks of this method are: it becomes complicated for the method to work with large scale applications as the stability condition connects the time step with the spatial size of the smallest mesh element; being a method with low order, the precision of the outcome may undergo numerical dispersion.

- **Finite Volume Time Domain (FVTD)**

In the beginning, finite-volume method was used for solving the equations only in fluid dynamics. In the 90's, Madsen [174], and Shankar [175] altered this technique for the solution of Maxwell's equations. Like the Yee algorithm, Madsen also proposed an interleaving of the fields and in such cases the method may be mentioned as a hybrid FDTD - FVTD method. Here the electric and magnetic field components are put on the edges of the primal and dual cell respectively. Another FVTD method was suggested by Yee and Chen [176, 177]. In contrast to the method proposed by Madsen, they stored the fields on the vertices of the cells that lead to the simplification of the derivation of the updated equations. In FVTD formulation, Maxwell's equations in the integral form are used to conserve the field quantities, whereas in the standard FDTD method, the electric and magnetic field vectors are stored on the nodes of grid cells, and in FVTD the fields are described in minor volumes n space. The main advantage of the FVTD method over the FDTD method is the generality of the unstructured mesh, allowing the conformal estimation of the curved surfaces. Besides, this method can be used for non-uniform meshes also. The spatial discretization for linear and non-dispersive materials has to be smaller than $\lambda_{\text{dielectric}}/10$, where $\lambda_{\text{dielectric}}$ is the wavelength inside the dielectric. Materials having large electric permittivity can be discretised into smaller cells compared with materials with low electric permittivity. The unstructured mesh allows an uninterrupted transition between materials with high and low permittivity, and this typically reduces the number of cells in the entire mesh. Globally the FVTD method is a combination of an explicit time domain method along with an unstructured mesh. The shortcomings of this method is the requirement of a dual grid, which may be difficult to generate the larger stencils, needed for greater precision, pulling down the locality of the technique. Moreover, this method is not divergence free.

- **Finite Element Method (FEM)**

The FEM was originally developed in the 1940's for the application in structural mechanics. Until 1990s FDTD was popularly used due to its directness and capability with respect to the computational resources. By further developing the FEM in Time Domain, and by utilizing refined algorithms, higher efficiency and accuracy could be accomplished. Contrary to the standard FDTD method, Finite Element Time Domain (FETD) can be worked on unstructured meshes. FETD can also be used to deal with higher-order polynomial functions. A clear conceptual difference exists between the finite

difference and finite element methods. FD method approximates the operators (derivatives) $\partial t/\partial u \approx (u(t_{i+1})-u(t_i))/\Delta t$,and FE method approximates the solution of the differential equation $u(t) \approx \sum_i^N u_i \phi_i(t)$, where $\phi_i(t)$ is a local basis of expansion function defined over a local finite element, and then adjust the solution to reduce the variation between the numerical and exact solution. A downside of this method is that a big albeit often sparse matrix, have to be defined in implicit schemes, to accomplish continuity at element boundaries, often restricting the applications of the method. This technique is explicit in second order central finite difference method. Limiting this method to low orders accepts an iterative scheme. Nevertheless, this method is not divergence free and introduces dissipation [178].

4.2 Numerical Study

In the past few years, complications of process focus in materials science and experimental physics are constantly expanding, so much that an analytical route towards theoretical modelling is leaving the field approaching its numerical counterpart. This inclination towards numerical modelling in research thus elevated the development of comprehensive numerical packages providing an extensively precise description for physical processes. Impressive detailed insight can be attained for design and performance of specific systems, providing a validation of the expected functionalities or beneficial suggestions for improvement. At such stages, to achieve the targeted results several attempts are made where countless trials-and-errors are not possible. Considering a vast range of applicability, the possibility of implementing this technique as a genuine numerical method, able to predict the results of an experiment before performing it, results exceedingly favourable. This becomes much more convenient when the focus of the study is a complicated nanostructured system where fabrication can be mainly time consuming and exorbitant.

4.2.1 Introduction to COMSOL Multiphysics

COMSOL Multiphysics is a versatile simulation software used in the fields of engineering, manufacturing, and scientific research. The software carries single-physics modelling capabilities, fully-coupled multiphysics, simulation data management, and convenient tools for constructing simulation applications. The software allows physics-based user interfaces and coupled systems of partial differential equations (PDEs) together.

The finite element method (FEM) is a general numerical method used for solving PDEs in two or three space variables. For the solution of a problem, FEM subdivides a larger system into smaller and simpler parts, called finite elements. This is accomplished by space discretization, that is carried out by the construction of a mesh of the object. The easy and manageable equations that represents these finite elements are then assembled into a larger system of equations that models the complete problem. The FEM then approximates a solution by minimizing an associated error function via the calculus of

variations.

COMSOL Multiphysics includes the Model Builder that contains all the features and operations for constructing, solving and post processing the models, the Application Builder provides the tools to build a self simulation app, and the Model Manager is a simulation data management tool.

There are several add-on modules providing specialized functionality, categorized according to the application areas for electromagnetics, acoustics, fluid flow, structural mechanics, heat transfer, and chemical engineering.

4.2.2 Wave Optics Module

The Wave Optics Module is one of the several modules offered by COMSOL Multiphysics. This module is used by engineers and scientists worldwide to comprehend, speculate and study electromagnetic wave propagation and resonance effects for optical applications. By evaluating em field distributions, transmission and reflection coefficients, and power dissipation in a planned design, simulations would open a way for powerful and efficient products with superior engineering methods.

The Wave Optics Module allows to easily set a model in 2D, 2D axisymmetric, and 3D domains. The workflow is simple and direct, and is described in various steps: import or creation of a geometry, selection of materials, selection of suitable Wave Optics Interface, defining the boundary and the mesh, selection of a solver, and visualization of the results. Em modelling needs highly appropriate boundary conditions, including the ability of modelling unbounded domains as well as periodic structures like metamaterials. The functionality of this Module includes simulation of electromagnetic fields and waves based on Maxwell's equations along with material laws for propagation in several media. The modelling abilities are acquired via built-in user interfaces, which permits the analysis of wave phenomenon in optics and photonic devices. For data visualization and extraction, the results are presented using plots of electric and magnetic fields, reflectance, transmittance, S-parameters, power flow, and dissipation.

General Introduction to the terms used for numerical study The wave–optics module in COMSOL Multiphysics is used to predict the optimal design of the absorber coatings, starting with the interaction of light with the nanoparticles. The technique used in this study is based on multi-scale modelling of the absorber layer. The geometry will be parametrized and a reduced order modelling technique, based on a method called Proper Generalized Decomposition (PGD), is appointed within a co–volume time domain electromagnetic algorithm. This will be used to establish the solution as a function of the shape parameters. To determine the optimum shape that brings about a near unity absorption, optimisation at the upper scale micro–level will be used to model the composite absorber layer as chiral and anisotropic with dispersive layers. The material properties of these layers will be computed from the solution obtained at the nano–scale

level, using a homogenisation technique. A gradient free optimisation scheme, based on the modified cuckoo search, will be used to determine the optimum shape, its orientation and the number of layers to be used. Verification of the findings will be executed by comparing the computationally predicted optical properties with those that are observed experimentally.

In COMSOL Multiphysics, there are two ways to retrieve parameters, first by creating a nano-scale numerical model and obtaining the parameters directly. Second, by utilizing the nano-scale numerical model, a new homogenization technique that is developed and implemented in the macro-scale numerical model to obtain the effective material parameters corresponding to a given geometry of the inclusion at nano-scale. In our study, we have utilized both direct and indirect method for the retrieval of parameters for the given geometry. Before we understand the implementation of the two methods in our work, it is important to know the following terminologies:

1. **Port:** The ports are essential in any numerical model created, for computing the scattering parameters, and are usually placed at the interface between the free space and perfectly matched layer (PML). The Port is used as a node where incident electromagnetic wave is excited. A port assumes that the geometry cross-section and material is constant in the normal direction. Moreover, the port boundary is assumed to be flat, that results in a constant normal throughout the boundary.

2. **Perfectly matched layer (PML):** The PML domain functionality indicates stationary governing equations that have wave-like behaviour in nature, where the fields represent a radiation of energy. One such case of this is the electromagnetic waves, frequency domain interface. The PML acts as a domain which is as good as an ideal absorber. Not only with plane waves, PML remains valid with all types of waves. It is also very efficient at oblique angles of incidence. In the frequency domain the PML takes advantage of a complex-valued coordinate transformation to the selected domain that successfully makes it absorbing at a maintained wave impedance, and thus excluding reflections at the interface.

3. **Mesh:** The mesh used for the modelled geometry plays an important role in making us understand the way the model is solved. It determines the factors like the way geometry is divided, kind of shape or element the geometry is divided into, the size, density and the number of elements present in the geometry, and the quality of the element. These factors affect the computation of a problem , directly, including the time and the mount if memory required to solve the model, the way solution is interpolated between the nodes, and the precision of the solution. In COMSOL Multiphysics, meshing employs different element types, they are tetrahedra (tets), hexahedra (bricks), triangular prisms (prisms), and pyramids. Apart from this, there are nine element size settings present, which runs from Extremely fine to Extremely coarse.

4. **Floquet Periodic boundary condition:** Floquet boundary condition is a periodic condition used to establish the displacements and rotations on two different sets of edges considering the same geometrical shape, as in a periodic structure. Utilizing the floquet boundary condition, the modeled structure becomes typically a unit cell of a repetitive structure.

5. **Perfect electric conductor (PEC):** The perfect electric conductor is a specific case of a boundary condition that makes the tangential component of the electric field to zero. $n \times E = 0$. It is applied in the case of modelling of a lossless metallic surface, example, a ground plane, or as a type of symmetry boundary condition. It applies symmetry for magnetic fields and magnetic currents and antisymmetry for electric fields and electric currents. A perfect electric conductor has zero electrical resistance, so a steady current in a perfect conductor will flow without losing its energy to resistance. The heating in conductors is caused due to resistance and thus a perfect conductor will not generate any heat.

6. **Scattering Parameters:** The scattering or S parameters are essential quantities to determine the electromagnetic properties of the material, the theory for which is based on linearity assumption. The S parameters describes the input-output relationship between the ports in an electrical system. The S-parameters are complex numbers corresponding to the magnitude and phase of a signal. They are demonstrated in a matrix form with rows and columns equal to the number of ports. For two ports, the matrix is:

$$\overline{\overline{\mathrm{S}}} = \begin{pmatrix} \mathrm{S}_{11} & \mathrm{S}_{12} \\ S_{21} & S_{22} \end{pmatrix} \tag{4.1}$$

For a matrix element $\mathrm{S_{ij}}$, subscript j corresponds to excited input port and subscript i corresponds to output port. S_{11} is the ratio of the signal that reflects from first port to the amplitude of the signal incident on the first port. S_{21} refers to the response at the second port due to an incident signal at first port. Parameters along the diagonal elements of $\overline{\overline{\mathrm{S}}}$ correspond to the reflection coefficients because the S-parameters only considers what happens at one port. On the other hand, off-diagonal elements correspond to the transmission coefficients because they refer to what happens at one port when it is excited by an incident signal at the other port. The process for the extraction of optical constants n and k from the S parameters is explained in detail in annex 6.1.

4.3 Defining geometric parameters for the design of the dielectric composite

Computational electromagnetics is nowadays regularly used to instruct selections during the initial designing phase of many components and devices. In some growing areas (e.g. nano–optics and nano–photonics), the utilization of computational methods goes ahead of its classical use to accelerate the designing process. Computational methods are

nowadays used for the revelation of advanced solutions and for comprehending the fundamental physics. Structured meshes based on multi–block decomposition are employed, but the mesh generation process often proved to be time consuming and inappropriate for general three dimensional geometries. These problems were reduced by the introduction of fully automatic unstructured tetrahedral mesh generators[179] and the execution of finite element based electromagnetic solvers on these meshes[180]. Yee's scheme for the solution of the Maxwell equations is a co–volume method that was initially implemented on a pair of mutually orthogonal structured meshes[172]. This algorithm shows a high degree of computational efficiency, in terms of both CPU and memory requirements when compared to, for example, a finite element (FEM) solution method.

To meet the required characteristics for CSP applications, the optimisation of the shape of an inclusion, its orientation and its periodicity within the absorber layer is to be carried out. The technique used for this purpose will be based on multi–scale modelling of the absorber layer. The aim of the optimization process is to predict the shape and orientation of the nano-structure and the thickness of the absorber, that includes the number of unit cells in the normal direction. It is to note that the geometry of the nanostructures, their shape and size play a major role in the extensive investigation of absorption of light. By appropriately modifying the structural parameters of the selective solar absorbers (SSA), the spectral absorption range can be tactfully tuned with regard to the centre wavelength and bandwidth concerning highest absorptance to build the solar absorber devices in varying colours[181, 114, 182]. In the past a lot of work[183, 184] has been carried out where design and structure were studied numerically and experimentally, showing high solar absorptance with low thermal emittance and good thermal stability. Nevertheless, there is always room to further investigate the geometry and design of the nanostructures in developing a SSA, to broaden the absorption spectrum of the device into longer wavelength region to gain additional energy from solar radiation with greater efficiency in the solar-to-thermal conversion mechanism.

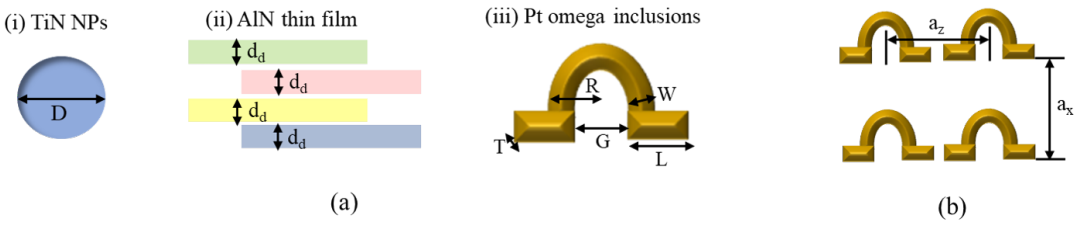

Figure 4.1: (a) Geometric parameters required to be defined for each of the component of SSC by numerical method, later for experimental validation. (b) Schematic of periodicity of array of Omega cells.

4.4 Methodology adopted for the prediction of geometric parameters, optical constants n and k, and reflectance of SSCs, numerically

In this section, we would understand in detail the methodology that was adopted to construct the SSCs numerically. Here, we focus on an ideal scenario of numerical simulations alongside retrieving the parameters of the (SSCs) numerically that would help in synthesizing the composite experimentally.

Retrieval of diameter (D) for the TiN NPs In this case, we study the approach acquired to retrieve the parameters that would be used to synthesize only one component of the SSCs, i.e, the composite of the SSCs. It is worth noting that the unit cell shown in the figure 4.2 is constructed before the experimental preparation of the SSCs. The main aim of modelling this unit cell is to know the diameter of the TiN NPs that leads to the most extinction of light in the visible region of the spectrum. This unit cell would also provide us with the retrieval of optical constants n and k through S parameters.

To begin with, a nanoscale model was created, where we included a TiN NP inside the matrix of AlN. *Instead of modelling an array of* TiN *NPs with* AlN *thin film over the bulk silicon, we used a single unit cell along with a Floquet periodic boundary condition on the sides [185, 186]. This approach significantly reduces the computation time of the model, without compromising the accuracy of the results. Figure 4.2(a) shows the constructed nanoscale–model, where a single* TiN *NP is buried in a* AlN *matrix, forming a single unit cell. The perfectly matched layer (PML), indicated in yellow, is a domain/layer that is included to mimic a non–reflecting infinite domain. The top and bottom surface, between the PML and the air, is considered as the port from which the excitation of the incident wave is activated.* The mesh generated for the model is fine enough to capture all the phenomenon of absorbance and at the same time is as coarse as possible to lower the computational costs. *The maximum mesh element size used in the electromagnetic simulations is* 5nm. *This is much smaller compared to the minimum wavelength λ simulated. The refractive indexes of* AlN *and* TiN *are dispersive over the frequency spectrum, for our simulations we used the data available from database https://refractiveindex.info. In order to ensure sufficient accuracy and mesh convergence while doing parametric sweep calculations over the spectrum* 250nm–2.5μm, *the PML is always maintained to be $\lambda/2$ and eight prismatic elements, the air space between PML and unit cell is three prismatic elements. Tetrahedral elements are used to mesh unit cell including the NP and the element size is chosen to be fine enough (*5nm*) to resolve the particle curvature and also kept below $\lambda/8$. Quadratic elements are used with direct solver which counts for* 54000 *dof which have shown good convergence rate for all frequencies.* In the figure 4.2(a), we considered a linearly polarised plane wave with angular frequency ω which is normally incident on a planar sample (in this case, on the unit cell with AlN matrix with TiN inclusion) of infinite lateral extension and finite thickness d situated in free space. *The*

performance of the proposed design will be validated experimentally by a comparison with the prediction of the numerical model. The aim of the numerical optimization is to determine the size of the NPs, so that the material maximizes the absorption in the visible fraction of the solar spectrum, as well as the reflection in the IR region of the spectrum. We investigated, on the unit–cell, the extinction cross–section relative to the particle volume, ranging from 20nm−60nm TiN *particle diameter. The extinction cross–section, sometimes called the attenuation cross–section, [129], is the area which, when multiplied with the irradiance of electromagnetic waves incident on the unit cell, gives the total radiant flux absorbed by the unit cell formed with the* TiN *particle buried in the* AlN *matrix.We define*

$$\sigma_{ext} = \sigma_{sca} + \sigma_{abs} \tag{4.2}$$

where, σ_{ext} *is the measure of the dissipation of light in a medium,* σ_{sca} *is the amount of light scattered inside the material by particles and* σ_{abs} *is the amount of light absorbed, as Joule loss, in the material.*

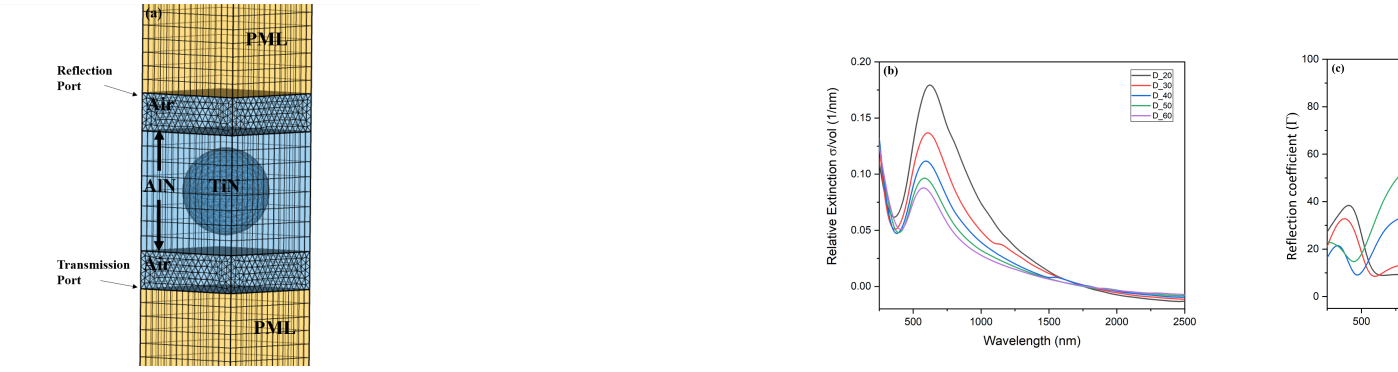

Figure 4.2: (a) Single unit cell modelled with TiN NP inclusion in AlN host. (b) Extinction cross section for various particle sizes showing that small particle diameter (20nm) gives better performance. (c) The reflectance results showing that 20% volume fraction of TiNperforms the least reflectance over the visible and the most in IR fraction of the spectrum.

On investigating on the unit–cell, the extinction cross–section relative to the particle volume, ranging from 20nm − 60nm TiN *particle diameter with a step of every* 10nm*, it is seen in Figure 4.2(b) clearly that* TiN *particle diameter of* 20nm *demonstrates the best*

curve in terms of relative extinction of the incident wave with wavelength. The bigger the TiN *particle, the more was the reflectance in the visible region. One reason for more reflectance in case of bigger particle could be more scattering.* Thereafter, in all the experiments carried out for the synthesis of the composite dielectric, we used TiN NPs with the diameter of around 20nm. After having achieved the D for the TiN NP, we now calculated the *vf* of TiN NPs in AlN matrix to achieve reflectance curve close to the reflectance curve of an ideal absorber (shown in black in figure 2.4). Four different volume concentrations $20\%, 25\%, 50\%, 75\%$ were investigated while the diameter of TiNwas fixed in each case. *The vf of* TiN *with best reflectance and absorbance would be considered hereafter in all the experiments. Figure 4.2(c) shows the computed reflection coefficient (*Γ*) for* $20\%, 25\%, 50\%$,75 *different volume fraction of* TiN *NPs in the* AlN *matrix. For the composite with* vf *of* 75% *of* TiN *NPs inside the* AlN *matrix, a high reflectance in the visible and IR region is seen, which is not what we are seeking. The composite with vf of* 20% *of* TiN *gives the best absorbance (least reflectance) in the visible region and high reflectance in the IR. The* 20% *volume fraction also has a peculiar characteristic of a sharp filter between the reflectance in the visible and the IR region of the spectrum.* Also, the *vf* of 75% of TiN NPs would form a connecting conducting network of TiN NPs in the AlN matrix disregarding the rule of sub-wavelength inclusion as explained in Chapter 3 in the section 3.4 for metallic particles 3.4.1, giving rise to high reflectance in the visible region of the spectrum obstructing the optical performance of the composite dielectric and thus the SSC. *Thus, in all our subsequent experiments carried out for the preparation of the composite, we used* 20nm *diameter* TiN *NPs and tried to control the concentration of* TiN *NPs close to* 20%.

Retrieval of volume fraction vf**of** TiN **NPs inside** AlN **matrix** The retrieval of the optical parameters (n, k) is not direct but is based on the calculation of S-parameters that are associated with complex reflection and transmission coefficients, that is described in annex 6.1 in detail. Once the S-parameters are obtained, they are placed in the python script that calculates the effective n and k. The formulas used the retrieve the dielectric properties (described by n, k) by the python script, from S-parameters are discussed in annex in detail. Once the n and k are obtained from the micro-model (homogenisation) described by the above method, they are now fed into the macro-model that would provide us with results of interest, the reflectance of the $20\%\mathrm{TiN} - \mathrm{AlN}$ composite and the filter characteristic of the composite at different angle of incidence of the incident electromagnetic beam. For the preparation of a numerical macro-model, the thickness of the composite (mix of TiN and AlN) was taken as 1μm. The bottom surface, between the PML and the air, is considered as the port from which the excitation of the incident wave is activated. The constructed macro-model is shown in the Figure 4.3(a). *The behaviour of the computed reflectance, for* 20% vf *of* TiN *NPs in the* AlN *matrix, was studied in the visible and IR region.* The same macro-model is also used to examine the filter

characteristic of the composite. The incident light was projected at the composite from different angles of incidence (0°, 30°, 45°, 60°) to check the performance of the composite by studying its reflectance with wavelength. *Figure 4.3(b) shows the computed reflectance spectrum from the same macro–model at different angles of incidence. It is clear from the figure 4.3(b) that, at* 60° *angle of incidence of the incident wave, the composite gains about* 20% *more reflectance in the visible spectrum and loses about the same in the IR spectrum, compared to* 0° *angle of incidence. An important feature to note here is the same trend of reflectance for all angle of incidences throughout the spectrum. This signifies that the optical performance of the composite does not change much even at the grazing incidence which is a privilege.*

In the entire work carried out in the thesis for both numerical and experimental study, transmittance is considered 0 **i.e;** $A = 1 - R$**.**

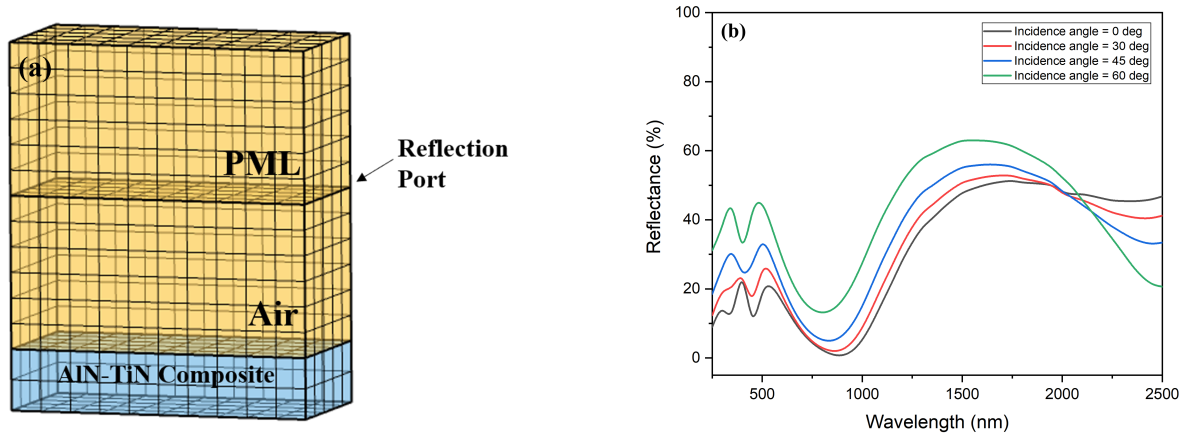

Figure 4.3: (a) Macro-model modelled numerically with homogeneous distribution of TiN NPs distributed all over in AlN matrix. (b) Reflectance curves achieved at different angles of incidence for the prepared macro-model.

Dimensions of parameters for omega structure After having studied the reflectance behaviour of the 20%TiN in AlN matrix, forming a composite for SSC, it is now time to study the reflectance behaviour of the composite with the omega structures on the top which makes the complete SSC. We refer this as a metamaterial. For this investigation, it is important to know the dimensions of omega structure which included the loop radius (R), the arm length (L), width of the metal strip (W), gap between the arms (G), thickness of the metal strip (T) and the size of the unit cell (D). For the reflectance curve that we aim to achieve, omega structure with particular dimensions for the parameters mentioned, was optimized for the $20\%TiN - AlN$ composite. The essence of the calculations of parameters of the omega structures is shown in annex 6.1. The parameters achieved for the construction of omega on top of the composites, are shown below in figure 4.4.

Parameter	Description	Values (nm)
R	Loop radius	500
L	Arm length	480
W	Width of the metal strip	218
G	Gap between the arms	39
T	Thickness of the metal strip	98
D	Size of the unit cell	1250

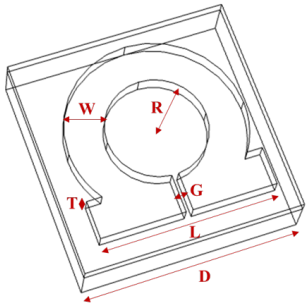

Figure 4.4: Parameters obtained for the omega structure.

We begin with constructing a model for the composite with omega inclusion on top to build complete SSC. After having achieved all the parameters of the Pt omega structure, yet another structure was modelled where a single structure of omega(with the dimensions mentioned in figure 4.4) was placed on top of the dielectric composite with 250nm thickness as shown in figure 4.5(a) . *Floquet periodic boundary condition was used on the sides of the modelled structure. [185, 186]. This approach notably minimizes the computation time of the model, without compromising the precision of the outcome. The perfectly matched layer (PML), indicated in yellow, is a domain/layer that is included to mimic a non–reflecting infinite domain.* The thickness of the PML in this case is taken as 250nm. *The top and bottom surface, between the PML and the air, is considered as the port from which the excitation of the incident wave is activated. The mesh generated for the model is fine enough to capture all the phenomenon of reflectance and at the same time is as coarse as possible to lower the computational costs. The performance of the proposed design will be validated experimentally by a comparison with the prediction of the numerical model.* The aim of the numerical optimization is to determine the curve for reflectance after the addition of omega resonator to the composite.

Figure 4.5(b) shows the reflectance curve achieved for the structure shown in figure 4.5(a). The purple dotted curve shows below 20% reflectance in the visible region of the spectrum, a filter near 1μm and reflectance of 60% and higher in the infrared spectrum. Whereas the dotted green curve shows the reflectance for only the composite, substituting omega structure as air. It is understood from the graph that addition of omega to the composite did show improvement, and enhanced the filter characteristic and the reflectance in the infrared spectrum. The omega structure did work as a resonator here.

Inter spacing between TiN **NPs** After achieving all of the above parameters, we made a calculation to know about the distance d the size of the unit cell of AlNwith TiN inside.

$$\mathrm{d} = \mathrm{D} * vf^{\frac{1}{3}} \approx 34\mathrm{nm} \tag{4.3}$$

This makes the distance between the two consecutive TiN particles $\approx$ 14nm.

It is simple to control the horizontal distance of 14nm between the TiN nanoparticles

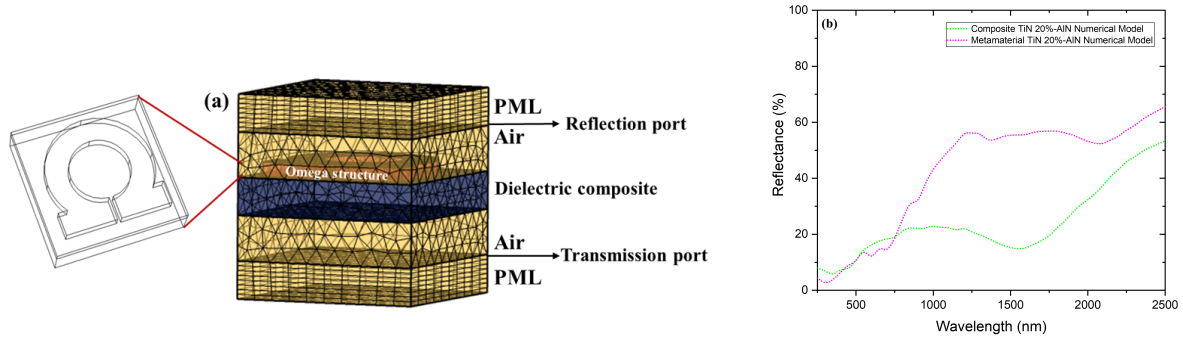

Figure 4.5: (a) Structure modelled with Pt omega structure on top of the dielectric composite. (b) Comparison of reflectance between 20%TiN-AlN composite and metamaterial 20%TiN-AlN(omega on top of the composite), obtained numerically.

when they are distributed manually with a certain volume fraction in the AlN matrix. Therefore, a distance of 20nm (rounding off to nearest 10) was tried to maintained between the particles vertically. Hence, 20nm of AlN layer was deposited conformally over the TiN particles.

4.5 Experimental Section-Process for the synthesis of AlN – TiN dielectric composite

In this study a considerable portion is dedicated to numerical modelling, experimental validation will allow us to demonstrate that the technique that the technique can be practised for the design of micro-scale composite absorber.

For the synthesis of the composite, a two–step approach was chosen that included a wet–chemical method for the distribution of TiN *NPs and a thin film deposition technique for* AlN *thin films. It was not possible to achieve both the phases of the* TiN/AlN *composite simultaneously, using a deposition process such as atomic layer deposition (ALD), physical vapour deposition (PVD) or chemical vapour deposition (CVD), in a controlled manner Khanna et al.[67]. The approach proposed by Bilokur et al.[187] and Du et al.[188], a single method of DC magnetron sputtering provided deposition of Titanium Aluminum Nitride (*TiAlN*) crystals. In such cases, depending upon the composition of* Ti *and* Al*, the layer was tuned for sought optical properties. Whereas, in our work, we expect to have individual properties of* TiN *and* AlN*, in a single composite.*

Several layers of TiN *NPs embedded in a* AlN *matrix were synthesized, one on top of the other, making it a single composite of a thickness of few hundred nanometers. Each single layer of* TiN *NPs embedded in a* AlN *matrix was obtained first by dispersing* TiN *NPs onto the previous layer. A conformal film of* AlN *is then deposited on to the* TiN *dispersion. Two approaches were adopted to obtain the* TiN *NPs dispersion: the first starting from dry powders of TiN (Goodfellow) followed by suspension in deionized water; the second by directly adopting a ready–made suspension (US Research Nanomaterials Inc.). In*

Chapter 5 we will analyse the two kind of composites, one where TiN *NPs dispersion comes from the preparation based on dry powder and the other where the dispersion comes from the ready–made suspension. This will be accomplished by making a clear comparison with the differences in the* SEM *images,* XPS *analysis, electrical conductivity measurement and optical measurements.*

4.5.1 *TiN nanoparticles suspension from dry powder*

The preparation made from TiN *dry powder (*approx 20nm*) particle diameter, purchased from Goodfellow Suppliers) and water showed the presence of several large chunks of aggregated nanoparticles. This became evident when bigger clusters precipitated at the bottom of the beaker, if the solution was kept stationary for several hours.* SEM*(Scanning Electron Microscopy) and* STEM *(Scanning Transmission Electron Microscopy) analysis confirmed the spherical shape and the diameter of* $15-25$nm *of the* TiN *components, as well as their agglomeration in chunks of few micrometers size. Clearly, for achieving good optical properties, it is crucial to have the* TiN *NPs in a well–dispersed state and several methods were adopted to disaggregate the chunks of* TiN *NPs.*

- *A bath ultrasonic cleaner (*VWR, 45kHz, 80W *) was used at first for the proper dispersion of nanoparticles by making use of capable amount of energy. After subjecting the* TiN *NPs solution to sonication for hours, there were no noticeable differences in the size of NP agglomerates before and after the sonication.*

- *Probe sonicator (*$Q500, 110V, 20kHz, 500W$*) was then used to sonicate the NPs solution as it provides more energy to the solution being in immediate contact with it. The probe sonicators have high localized intensity compared to a bath sonicator. Generally, ultrasonic probe sonicator exceeds an ultrasonic bath by a factor of* 1000 *i.e. higher energy input by three orders of magnitude, per volume. The use of probe with suitable size can greatly reduce the processing time and ensure the entire volume of the solution is processed properly. The volume of the solution is directly linked to the probe diameter which meant that, for sonicating small volumes of liquid (*$20-250$ml*), a probe with* 12.7mm *diameter ideal for such volume, was used. It is clear, from the graph in Figure3, that probe sonication greatly reduced the size of the agglomerates, resulting in the range* $100-500$nm *with very few chunks close to* 1μm.

- *With the objective of further reducing the size of* TiN *agglomerates, the probe sonicated solution was filtered, using a paper of pore size* 0.4μm. *This reduced the size of the* TiN *chunks to nearly* 200nm.

- *For better dispersibility of* TiN *NPs solution, chemical functionalization was carried out by adding surfactants. In the literature, we could not find any conclusive work specifically dealing with* TiN *NPs. In addition, it has been observed that none*

of the common surfactants (e.g. Ficoll 400, Tween 80, Chitosan and PEG-400), is able to stabilize the TiN *dispersions[189]. We chose , Polyvinylpyrrolidone –* **PVP***and* Polyethyleneimine – PEI *as stabilizers that are well suited for particles that have a metallic behaviour, but neither worked well for the stabilization of the TiN dispersions.*

Figure 4.6 summarizes the results of the various strategies adopted in order to disaggregate/remove TiN *NPs aggregates into the solution obtained from dry powders. For comparison, it also includes the ready–made solution by US Research Nanomaterials Inc.*

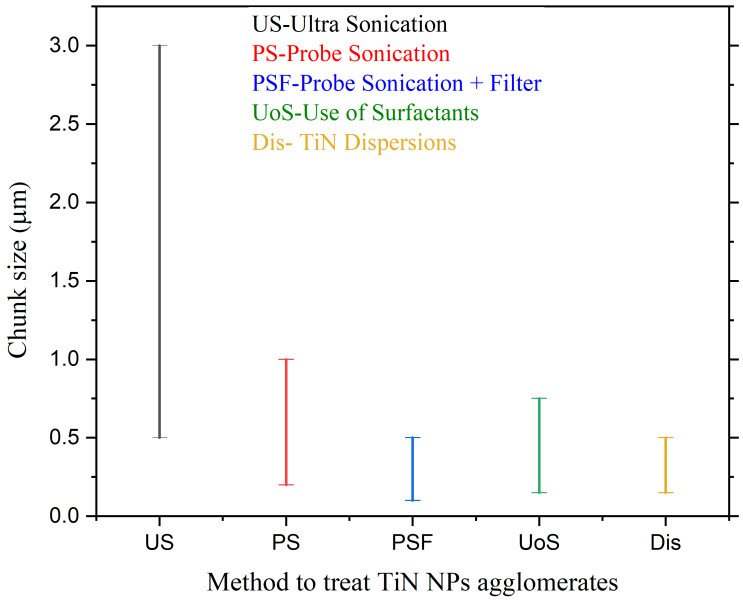

Figure 4.6: Graph showing the comparison between the agglomerates achieved after using different methods.

4.5.2 *TiN nanoparticles dispersion onto underlying surfaces*

TiN *NPs from liquid solution (either obtained from dry powder or ready-made one) were laid on an* Si *wafer by wet incubation method. They were then conformally coated with thin film of* AlN*, via plasma–enhanced atomic layer deposition* PE – ALD *[190, 191, 192], as shown in figure 4.7. The steps (a) and (b) of figure 4.7 were repeated several times, to obtain a composite with thickness of several hundred of nanometers, as illustrated in step (c) of figure 4.7. Among wet–chemistry synthesis routes for nanostructure fabrication [193], incubation proves to be a simple, cost– effective process, with rather easy control over the distribution of particles. In this process, the* Si *substrate is submerged into the nanoparticles solution and incubated for a controlled time, during which nanoparticles progressively undergo physisorption adhesion onto substrate surface. Parameters*

like solvent, particle concentrations, type of nanoparticles to be deposited and time of incubation, play an important role in nanoparticles deposition. All these parameters were fine–tuned in several experiments to obtain the desired distribution of TiN NPs. To improve the interaction of TiN NPs with the underlying surface (i.e. Si wafer at the beginning, AlN conformal layers by $PE-ALD$ for the subsequent steps), a method called surface functionalization was adopted [194], in which we functionalized the underlying surface with APTES ((3 − Aminopropyl)triethoxysilane) (99%) Sigma Aldrich). APTES is used as a special linking molecule that activates the Si surface by creating stable amino–terminations suitable for nanoparticle capture. The presence of hydroxyl groups on the surface is an essential requirement for the process of silanization [195, 196, 197]. Silanization refers to the process of functionalizing the surface with silane solution that results in the formation of a silane monolayer. For this purpose, the surfaces receiving TiN NPs were functionalized where they were treated using oxygen plasma by a reactive ion etching equipment (*Plasmatherm* 790 RIE) for 3 minutes. Oxygen plasma promotes −OH groups on the surface of the substrate, which covalently bind with the positively charged silane head groups from $APTES$. At the end of plasma treatment, the substrates are immediately submerged in an air-tight glass container with 20mM solution of APTES in ethanol, for 2 hours. Substrates are successively taken from the APTES solution, washed with ethanol so that the loosely attached silanes are removed and dried under nitrogen flux. The substrates are then dipped in the solution of TiN NPs (concentration 0.5 mg/ml) for 3 hours. In this step, the negatively charged TiN NPs stick to the positively charged Silane head groups of APTES on the surface. Finally, the substrates are washed thoroughly with water, for the removal of loosely or unbound TiN NPs, and dried with nitrogen. A detailed experimental process for the distribution of TiN NPs on the Si and glass substrate is described in figure 4.8(a).

4.5.3 *AlN conformal coating by (PE-ALD)*

The AlN layer over the distribution of TiN NPs, was grown by the $PE-ALD$ reactor (Beneq TFS 200). Precursor Trimethylaluminum $Al_2(CH_3)_6$ (TMA) and a proper mixture of N_2 : H_2 : Ar gases with a flow ratio of 100ppm/80ppm/30ppm, were used ($ALPHAGAZ, \geq$ 99.9999 less than 0.5ppm of H_2Omol impurity)[198]. The AlN films were grown by employing a sequence of four steps: TMA ($0.1s$), N_2 purge ($5s$), : H_2 : Ar plasma ($20s$), and N_2 purge (5s). The deposition temperature was set to 250°C. The plasma power was set at 100W. The above sequence was repeated through 275cycles, to deposit a AlN layer of about 20nm thickness. The process, of using a thin film of AlN to cover the TiN NPs laid over the substrate, by $PE-ALD$, is illustrated in figure 4.7(b). For the second distribution of TiN NPs onto the AlN film, which constitutes the 3rd layer of the composite, the process was repeated for silanization, but now the AlN layers were functionalized with 20mM solution of APTES with toluene as solvent[199]. This second distribution of TiN NPs was again coated with 20nm of AlN, which constitutes the fourth

layer in the composite. A total of eight layers were created to prepare the composite of the desired thickness, staring with the distribution of TiN *NPs (1st layer) and ending with the* AlN *film (8th layer), distinctly seen in the figure 4.7(c).*

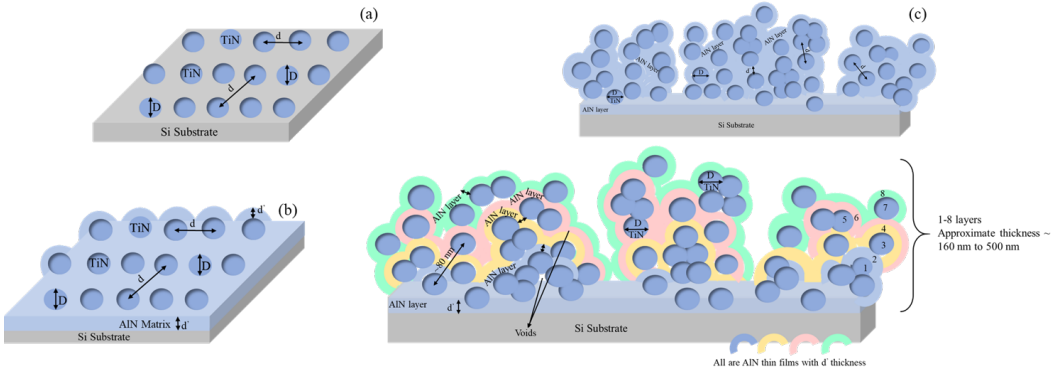

Figure 4.7: Schematic of the steps included in the synthesis of a composite; (a) Step 1: Distribution of TiN NPs on Si/Glass substrate. (b): Step 2: Covering TiN NPs with a thin film of AlN. (c) Step 3: Repeating Steps 1 and 2 several times to get a composite of the desired thickness.

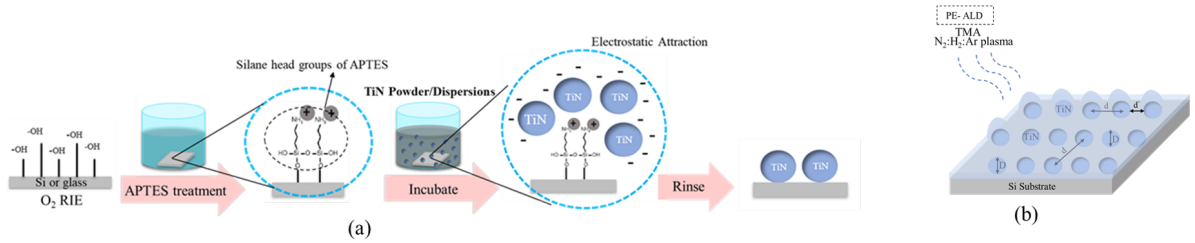

Figure 4.8: Detailed experimental process for the preparation of the composite.

4.5.4 Pt Omega Structures patterning by e-beam lithography

The standard process flow fabrication of a binary optics structure is sketched in figure 4.9. The exposure was performed with e-beam exposure tool by Raith eLINE Plus. A series of different base doses were done to find the correct dose. Before the beginning of the process, the Si substrates covered with $\sim 160 - 350$nm thick composite I and composite II, were cleaned with acetone/isopropanol/de-ionized water and then dried with nitrogen. The samples were spin-coated by Solarsemi QS200 with a 350nm thick e-beam resist layer of PMMA with 1500 rpm (see figure 4.9(ii)). It was soft baked using te hotplate, Solarsemi QS200 for 90sec at 180°C. The omega patterns are transferred to the resist by e-beam exposure with the dose of 182μm/cm^2. For the patterning of 5mm $\times$ 5mm area, it took 5 days to expose the whole matrix with the applied dose. Successful development of the exposed area (see figure 4.9(iv)) was done by washing the samples for 20sec in Methyl isobutyl ketone (MIBK) and Isopropyl (IPA) solvents mixed together in the ratio 1 : 3. For the process of metalization, metal deposition was done using e-beam evaporator DONTON VACUUM EXPLORER. For this process Ti/Pt (10nm/95nm) was deposited.

The last step included the process of a lift off in acetone, cleaned in IPA and distilled water, and dried in Nitrogen.

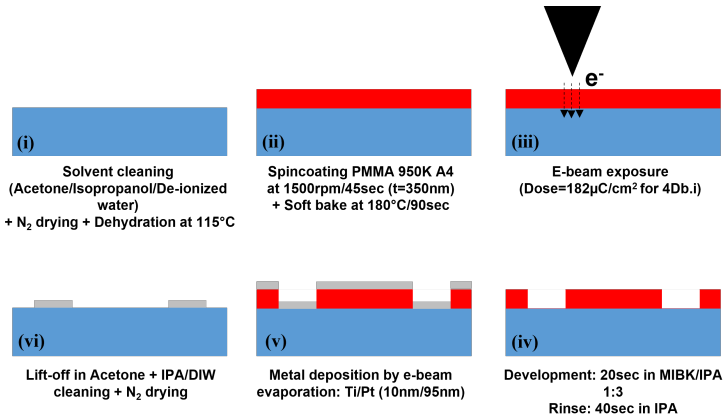

Figure 4.9: Schematic of the fabrication process flow followed for the development of omega on top of both the composites.

4.6 Retrieval of optical constants and reflectance, experimentally

4.6.1 Spectroscopic Ellipsometer

Spectroscopic Ellipsometer (SE) is primarily a technique for exploring the optical properties of film/composite materials with polarized electromagnetic radiation [200]. The universal goal of the ellipsometry measurements is fixed on the analysis of the polarization of the light beam reflected from the sample to be investigated. A linearly polarized light is directed towards the sample at a given angle. After the reflection of the incident light beam, the beam changes into elliptically polarized light [200]. This change in polarization is completely dependent on the angle of incidence, the wavelength, the thickness of the layers in the sample and their optical properties. These changes in the polarization is described by ellipsometric parameters, i.e. phase difference ($\triangle$), the difference between the p-wave and s-wave components of the wave after reflection, and tanΨ is related to the amplitude change. This is shown clearly in Figure 4.10 The angle of incidence at which the incident beam and the sample interacts should have the values close to Brewster's angle for which this method is the most tactful. A mathematical model reflecting the characteristics of the sample is generated using the ellipsometry software. This generated model is based on the parameters $\triangle$ and Ψ that were formulated during the measurements. The model uses mathematical relations called dispersion formulae that assist to evaluate the thickness, surface roughness and other optical properties of the material by modifying specific fit parameters. The degree of fitting the model value with the measured values is defined as mean squared error (MSE). The created model defines the layers individually through their thicknesses and the values of their optical parameters. These values might be taken from the ellipsometry material database or are created by the user. According to

the fundamental equation of ellipsometry[201]:

$$\frac{R_p}{R_s} = \tan\Psi.e^{i\triangle} \tag{4.4}$$

where R_p *and* R_s *are the intensities of the p-wave and s-wave of the reflected light, respectively.*

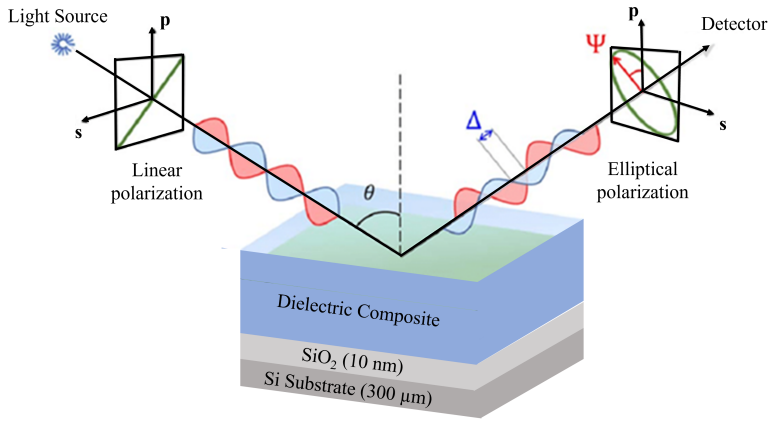

Figure 4.10: Basic principle of acquisition of n(λ) and $k(\lambda)$ by SE.

4.6.2 UV-Visible Spectroscopy

UV-Vis Spectroscopy is an analytical method that calculates the proportion of discrete wavelengths of UV or visible light that is absorbed by or transmitted through the sample compared to a reference sample. The property of absorption and transmission is influenced by sample composition. This spectroscopy technique depends on the use of light, therefore its important to first understand the properties of light.

The energy associated with light is inversely proportional to its wavelength. Light associated with shorter wavelengths carry more energy compared to lights with longer wavelengths. Certain amount of energy is required to promote the electrons to a higher energy state which can be detected as absorption. Electrons with different bonding environment in different substances requires different specific energy to promote electrons to the higher energy state. For this reason absorption of light occurs at different wavelengths in different substances.

In the spectrometer, a steady light source capable of emitting light across a broad range of wavelengths is essential. For this function two different sources are employed. A tungsten or halogen lamp to scan the visible wavelength and a deuterium lamp to scan the UV wavelength[202]. A reference sample is measured, often referred to as 'blank sample' for calibration. This is done for making a comparison with the actual measurement. After the light passes through the sample to be measured, the detector converts the light into

a readable electronic signal.

Figure 4.11: A simplified schematic of the main components in a UV-Vis spectrophotometer.

For the measurement of a clear liquid sample, the instrument measures direct transmittance as a percentage (%T) which is the measure of the percentage of the incident beam transmitted through the sample. This value is then used to calculate absorbance, where $A = \log(1/T)$. For the measurement of reflectance for a solid sample (in our case), there are two kinds of reflectance, specular and diffuse. Specular reflectance is the one where the incident beam is reflected at the same angle as the angle of incidence. Diffuse reflectance is the one where incident beam is all reflected in all the directions. Depending on the equipment used, it is possible to take separate measurements for specular, diffuse and overall reflectance. Reflectance measurements are either relative or absolute measurements. In this work we would measure total absolute reflectance which measures the proportional amount of reflected light relative to the amount of light measured directly from a light source.

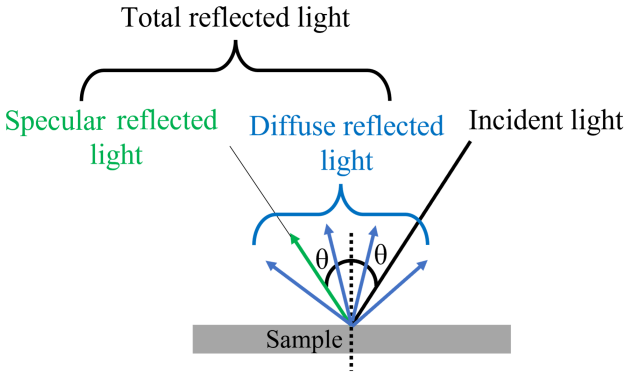

Figure 4.12: Illustration of total reflected light from the surface of the sample.

4.7 Thermal Stability Test of the composites and the metamaterial

Along with suitable optical properties, the adequate SSCs that are used in CSP plants needs to be thermally and mechanically stable in air and in vacuum at high temperatures. Various standards explaining the durability and aging tests of solar thermal collectors have been mentioned in the publications [203, 204, 205, 206]. In Europe, the EN 12975 -1:2066+A1:2001[207] is being followed. In order to predict the service life time of the SSCs of 25 years, the International Energy Agency (IEA) of the Solar Heating and Cooling

(SHC) program in Task X [208] established a plan of action to guess the lifetime of these coatings. For this process, the performance criterion (PC) is defined by:

$$\mathrm{PC} = - \triangle \alpha_{\mathrm{S}} + 0.25 \triangle \epsilon_{\mathrm{T}} \begin{cases} \mathrm{PC} \leq & 5\mathrm{PASS} \\ PC > & 5\mathrm{FAIL} \end{cases} \tag{4.5}$$

where $\triangle \alpha_{\mathrm{S}}$ is the change in solar absorptance, $\triangle \epsilon_{\mathrm{T}}$ is the change in the thermal emittance before and after the test.

Asymmetric thermal stability test

The asymmetric thermal stability test were carried out for the composite I and II, and for the metamaterial I and II, by exposing the samples at 800°C and 1000°C for constant 12hours in the furnace (Furnaturaex) by Aexor. The samples were exposed to Ar air flow under vacuum conditions with a programmable heating ramp of 5°C/min for reaching the needed temperature. After 12hours of heating, the samples were allowed to cool down to the room temperature inside the furnace.

After the thermal treatment of each of the sample mentioned above, a visual check is carried out to assess the condition of the coating's surface, where, the loss of homogeneity, change in colour and the presence of cracks in the composites and the metamaterials can be directly observed. The samples that passed the visual inspection were analysed by optical characterization, where all the samples are subjected to UV-Visible Spectrophotometer for examining their optical performance after long hours of heating.

All these results have been discussed in Chapter 5.

Chapter 5

Results and Discussions

The part of this chapter written in italics has been taken from my manuscript [67] and [the paper under submission].

5.1 Experimental synthesis of the composite

After having achieved all the parameters required to achieve maximum absorption in the visible region and maximum reflection in the infrared region, providing us with a clear idea regarding the performance of the solar selective coatings, we started with synthesizing the composite. Below are all the results of the steps that are used in the synthesis of the composite.

5.1.1 SEM analysis of the composite starting with the distribution of TiN NPs over the Si wafer

Knowing the diameter D that gave the required results in terms of absorption and reflection, D with 20nm were used in the entire experiments. *For this purpose dry powder of* TiN *was purchased from Goodfellow suppliers with nominal diameter of* 20nm *and ready-made* TiN *dispersions from US Research Nanomaterials Inc. also with nominal diameter of* 20nm. *The process adopted for laying* TiN *NPs on the* Si *wafer is described in detail in subsection4.5.2 of chapter 4. After distributing the* TiN *NPs over the Si substrate that made the very first layer of the composite, the morphology and the vf of the* TiN *NPs were analysed by Scanning Electron Microscopy (SEM).*

To estimate the volume fraction of TiN *NPs, we considered the area covered by in–plane SEM images, in sub– monolayer deposition conditions.We assumed that the fraction of area covered by* TiN *NPs corresponds to the volume fraction in the* AlN *matrix. For this purpose, SEM images were analyzed by* ImageJ *software. Figures 5.1(a), (b) show nearly* 20 *surface coverage fraction of* TiN *NPs distributed over the* Si *substrate (indicated by red the zone, with colour threshold for area calculation). Despite the manual approach, this result is well in line with the targeted value. The comparison of the* vf *with the area coverage is good as, according to the calculations, the vf is* 0.94 *times the area coverage.*

Assuming the configuration where the surface coverage is the projection on the surface, we can write $V_C = S_C(4/3)(r/a)$*, where* V_C *is the volume coverage of* TiN *NPs on the substrate,* S_C *is the surface coverage (projection) of the* TiN *NPs over the substrate, r is the radius of the* TiN *NP and* a *is the side of the single unit cell.* Figure 5.1(a), (b) makes the very first layer of the composite and describes the distribution of TiN NPs on a surface with a few single particles and many agglomerates lying all over the surface.

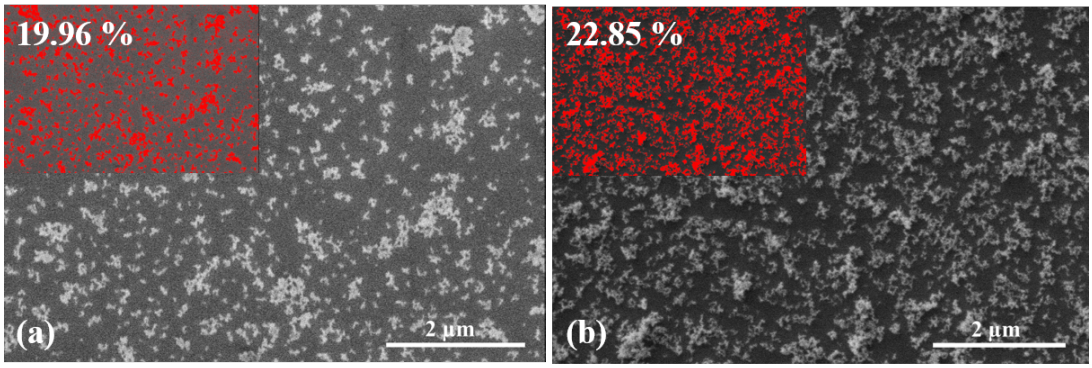

Figure 5.1: SEM images showing approximately 20 vf of distributed TiN NPs over the substrate. (a) 19.96 distribution of TiN NPs powder solution over Si substrate. (b) 22.85 distribution of TiN dispersions over Si substrate.

After the first layer of the composite, AlN thin film of $\sim$ 20nmwere conformally coated over TiN NPs, making it the layer 2 of the composite. The detailed process for this is explained in subsection 4.5.3 in chapter 4. Figure 5.2(a), (b) shows the TiN NPs from dry powder and TiN NPs from ready-made suspension conformally coated with AlN, completing the first two layers for composite 1 and composite II respectively.

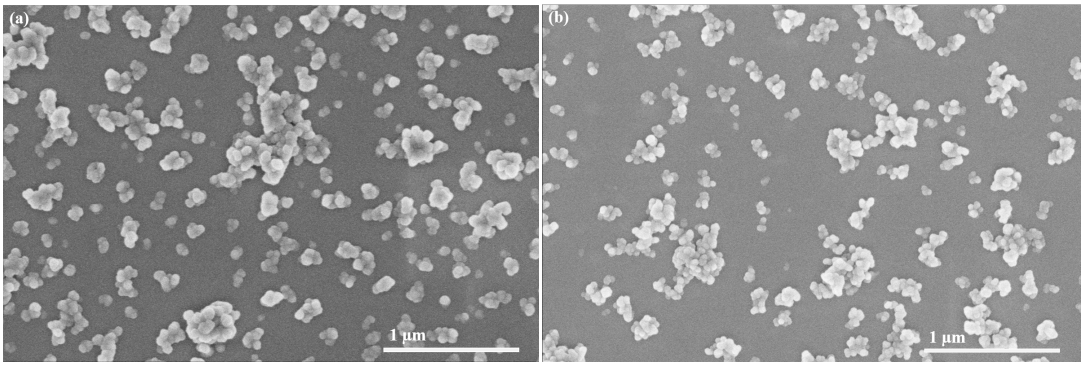

Figure 5.2: SEM images showing TiN NPs conformally coated with AlNthin film making layer 2 of the composite. (a) TiN NPs from dry powder conformally coated with AlNthin film, for composite 1. (b) TiN NPs from ready-made suspensions conformally coated with AlNthin film, for composite 2.

Layer 3 of the composite constituted the distribution of TiN NPs with again $20vf$, on top of layer 2 i.e. AlN thin film. Except layer 1, which was TiN NPs on the Si wafer, every alternate layer starting from layer 3 until layer 7, was the distribution of TiN NPs over AlN films. Figure 5.3(a), (b) shows the TiN NPs from dry powder and ready-made suspensions forming the 7th layer for both composite 1 and composite II. It is worth

noting in these SEM images that the distribution of TiN nanoparticles over AlN thin film is less as compared to the distribution shown in the figure 5.2. This happened because of the underlying rough surface that the previous TiN distribution provides for the upper one. This will reduce the vf of the TiN NPs in the composites which is expected to be 20% according to the outcomes of the numerical modelling. A study with the estimate vf of TiN is made in the subsection 5.1.2 below.

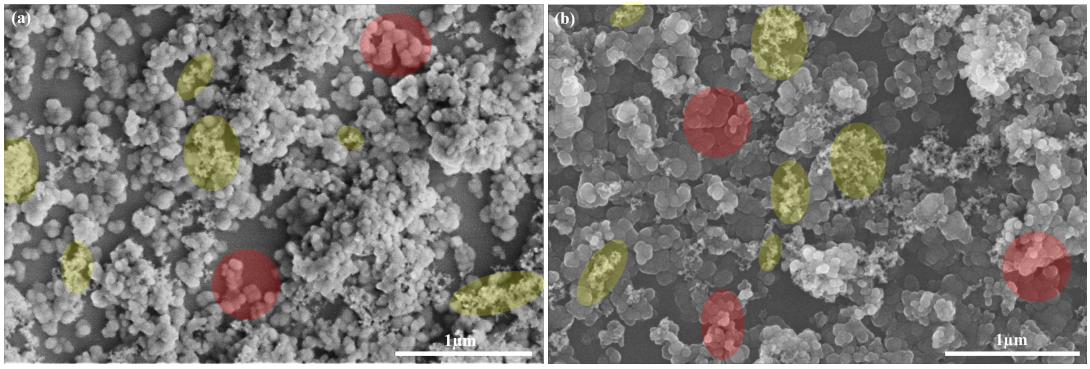

Figure 5.3: SEM images showing layer 7 of the composite with TiN NPs laid on top of AlNfilm. (a) TiN NPs from dry powder laid on AlNfilm from composite 1. (b) TiN NPs from ready-made suspensions laid on AlN film from composite 2.

Figure 5.4 shows a schematic with different steps involved in the synthesis of a composite. First one being the distribution of TiN NPs over the Si substrate, second is covering the TiN NPs conformally with AlN thin films via ALD, and third one shows the repetition of step a and b several times to attain the entire composite. The schematic below provides a better and a clearer understanding of the composite that was synthesized experimentally. The schematic of the composite drawn at the bottom in figure 5.4(c) shows four different bilayers in different colors, to better understand the structure. To not get confused with different colors, it is worth mentioning that the TiN NPs present in the entire composite are all the same (only difference being the different suppliers for TiN dry powder and TiN ready made dispersions) laid with the same method, and the AlN thin films are also the same formed with the same method. The top schematic of figure 5.4(c) shows the entire structure of the composite with eight layers of TiN and AlN in total. A single schematic was drawn for both composite 1 and 2 assuming that the structure and the morphology would be same with thickness being the only difference in the two composites. Justification of different thickness of the two composites would be shown next.

Figure 5.5(a), (b) show the cross–section, as well as the top view, of the final composites, at the end of the layering process, which includes four distributions of TiN *nanoparticles and four* AlN *films depositions by ALD alternating each other. Images clearly show that* TiN *NPs were conformally coated with* AlN*. Repeated layers of* TiN *NPs distribution and* AlN *thin film leads to a high surface roughness of the final composite. Cross sectional views reveal non–constant thickness, ranging from* 150nm *to* 560nm*, because of the piling–up of* TiN *NPs in the various positions of the substrate at the end of the pro-*

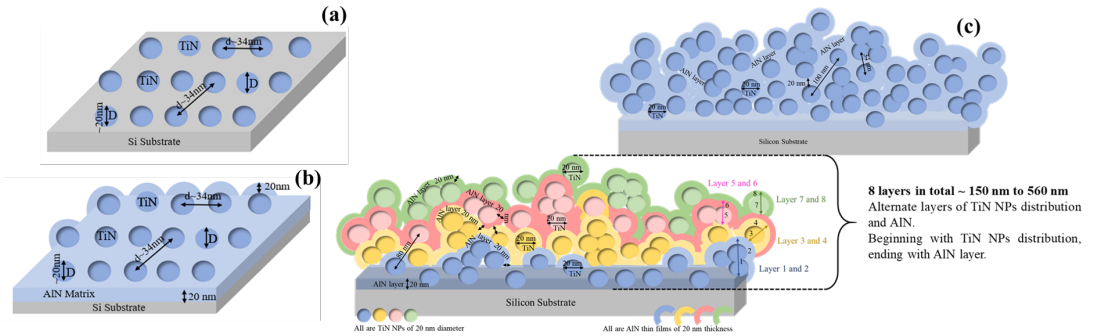

Figure 5.4: Schematic of the steps included in the synthesis of a composite; (a) Step 1: Distribution of TiN NPs on Si/Glass substrate. (b) Step 2: Covering TiN NPs with a thin film of AlN. (c) Step 3: Repeating Steps 1 and 2 several times to get a composite of the desired thickness.

duction process. Figure 5.5(a), (b) also discloses the different thickness of the composite I and II. It is inevitable from the *vf* of TiN NPs laid over the Si wafer in figure 5.1(a), (b) that the thickness of composite II would be more than that of composite I. The average height can be seen in figures (a) and (b) from the green marks where the average height in case of composite I is much less than the composite II.

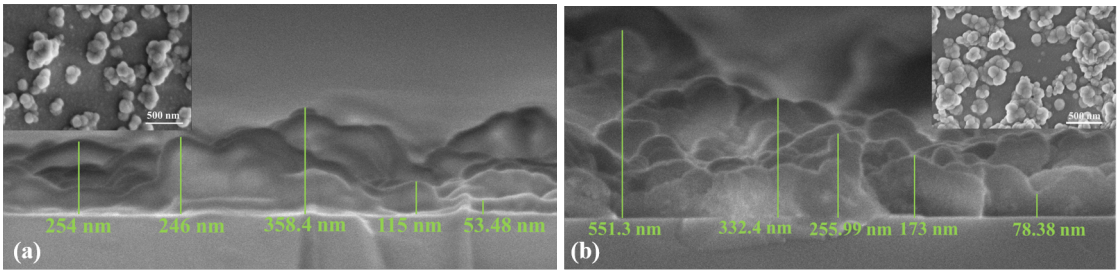

Figure 5.5: SEM images with cross-sectional and top view of the prepared composites. (a) Composite I prepared with TiN powder. (b) Composite II prepared with TiN dispersions.

The complete stack of multilayers after the integration of omega looks like as shown in the figure 5.6 . The entire process of development of omega on top of the composites was carried out in Institute Lafayette, France. work was carried out in The entire metamaterial II after the development and integration of the periodic array of omega added to the top layer of the composite II is shown in the figure below. The developments of omegas was done in 5mm $\times$ 5mm area. A 5mm $\times$ 5mm matrix layout was too dense and heavy that the e-beam exposure software could not handle it. Hence, four 1.25mm $\times$ 1.25mm submatrices along the x and the y axis were used to pattern a 5 $\times$ 5 matrix. This makes a total of 16 submatrices in 5 $\times$ 5 matrix. Each submatrix had around 1000 omegas along the x-axis and 1000 omegas along the y-axis which makes a total of 1000000 omegas in each submatrix. In this work the quality of omega depends on the presence of opening between the two arms, that we expected to be 39nm. According to the SEM analysis done, $1/3$ of the 5mm $\times$ 5mm matrix is good (classified by the presence of opening between the arms), $1/3$ is bad (classified by the absence of opening between the arms) and the remaining

1/3had both good and bad omegas. Hence, it could be concluded that only around 50% of 5mm × 5mm area has good omegas. The figure 5.6(a) and (b) shows bad omegas, 5.6(c) and (d) shows good omegas, and 5.6(e) shows zoomed omega with dimensions very close to the ones achieved numerically. Missing omega patterns in the areas of large chunks of TiN NPs can be seen in figure 5.6(a), (b), (c) and (d).

It was possible to pattern these sub-wavelength range omegas on top of such rough surface (composite II) however, it is very challenging to control the gap between the omega patterns. The two possible reasons for the absence of gap between the omegas are; first, long exposure times (it takes 5 days to expose the whole 5mm × 5mmmatrix) which means the risk of beam current variation and temperature change after a certain time, and this changes the exposure conditions. Second, is the amount of applied dose. Though several iterations of dose tests were carried out covering a wide range (from $70^{\mu C}/_{cm^2}$ to $182^{\mu C}/_{cm^2}$) but the dose depends on surface state of the underlying surface (composite II in this case). Many a times the resist was underexposed or overexposed with the given dose leading to no openeing between the arms in omega.

Note that omega patterning was done only on top of composite II, making it metamaterial II.

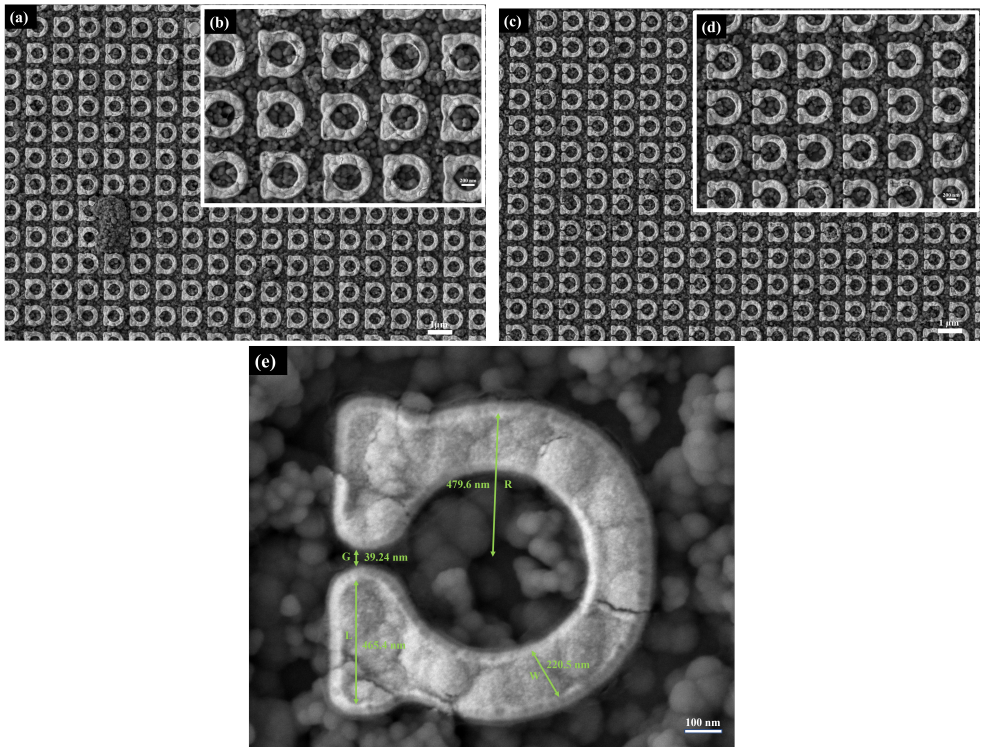

Figure 5.6: SEM Images of the developed metamaterial II on top of composite II. (a) An array of bad (closed) omegas. (b) Closer view of an array with bad omegas. (c) An array of good (open) omegas. (d) Closer view of an array with good omegas. (e) Omega marked with dimensions required.

5.1.2 XPS analysis of the AlN − TiN composite dielectric

To verify the elemental composition of our samples, particularly in respect to the presence of contaminants and to the in-depth distribution of the main constituents (namely Al, N *and* Ti*), XPS was carried out with a Kratos Axis Ultra DLD instrument using* Al*(*1486.6eV*) X-ray source at normal incidence angle with respect to the surface and a argon ion gun (*4keV*) for etching. Figure 5.8(a) shows the results of the XPS survey scans for both types of composite before the* Ar+ *etching. Aluminum and nitrogen are dominant at the surface, as expected. Prominent oxygen peaks indicate that the surfaces of the topmost* AlN *layer of both composites is strongly oxidized. In fact, the surface of* AlN *films is prone to oxidation, and the emergence of different forms of oxides and hydroxides, on its surface, has been reported [209, 210, 211, 212]. In addition, carbon, fluorine and chlorine are also observed and assigned to surface contamination, the last two with intensities close to instrument sensitivity limit. Figure 5.8 (b), (c) shows the elemental composition profile of the two composites over a total etching time of* 15min*. The* Si *signal and the oxygen linked to* Si*, appearing and becoming dominant at larger etching times, has not been considered in the calculation of the percentages, aiming at emphasizing the trends of the element of interest. With respect to surface composition, three main differences in both composites are highlighted by in–depth profiles. Firstly, the carbon intensity drops to a very low value, indicating the substantial absence of carbon impurities inside the composites. This in turn suggests that, despite the low temperature of deposition, there was no noticeable fusion of carbon containing ligands from* TMA *and the precursors used were completely decomposed[213]. In fact, if methyl groups from the* Al *precursors were trapped in the film, this would have given rise to a substantial amount of carbon. In summary, the absence of a carbon signal signifies that neither the deposition of* TiN *NPs (four repetitions in both composites) nor the deposition of* AlN *thin films (four repetitions in both composites) introduced carbon impurities.*

Secondly, the amount of oxygen shows a significant drop after the first steps of etching in both composites, suggesting that a considerable portion of it was the result of atmospheric oxidation. Yet, after the initial drop, the two curves show an increase up to remarkable level of oxygen, which remains rather constant throughout the composites volume. This is ascribable to oxidation taking place during composites preparation steps, where samples are exposed to the air after each AlN *thin film deposition as well as to post-deposition oxygen plasma treatment of* AlN*, the last aiming to promote* TiN *nanoparticles adhesion as explained in section 4.5.2 of chapter 4. It can also be ascribable to oxygen contamination affecting the deposition process of* AlN *itself. Aiming to investigate this last point,* AlN *films having thickness around* 400nm *were deposited and subjected to XPS in-depth profile analysis. An amount of approximately* 15 *at. of oxygen was observed in the volume. This suggests the presence of oxygen contamination sources (e.g. moisture) in the reactor chamber and/or in the precursor or gas lines and, consequently, the presence of* Al_2O_3 *or aluminum oxynitride (*AlON*) within the* AlN *film. Favourably,* AlN, Al_2O_3

and AlON*, all three are optically transparent materials in the near-ultraviolet, visible, and midwave - infrared regions of the electromagnetic spectrum, which would not have a major impact on the optical properties of the composites.* The graph in figure 5.7 below shows similar optical properties for AlN and Al_2O_3. *It is worth noting that both* AlN *and* Al_2O_3 *curves show no dispersion over the* $VIS-IR$ *spectrum e.g.,* n *is constant and no loss with* k *null. This makes both* AlN *and* Al_2O_3 *transparent to light.*

The third difference in the depth profile with respect to surface composition is the appearance of a titanium signal after a certain etching time. This grows until a fairly constant value is attained throughout the composite volume. This is clearly related to the presence of TiN *NPs, which are completely embedded inside the* AlN *matrix, as expected. It is worth notice that, because the X–ray spot dimension* $(700 \times 300)\mu m$ *is much larger than the dimension of* TiN *nanoparticles and the spacing between them, the profiles represent the average composition over the spot size. Moreover, due to the high roughness of both samples, resulting from random distribution as well as agglomeration of* TiN *nanoparticles (as unveiled by SEM cross–sections in figures 5.5(a),(b)), composition averaging should be considered also in the vertical direction. In this respect, the etching of the thinnest regions, where no* TiN *particles are present, quickly reaches the* Si *substrate, introducing an oxygen contribution related to* SiO_2 *on the substrate surface. On the other hand, the appearance of the* Ti *signal only after a certain etching time confirms that the* TiN *particles are all completely covered by* AlN*, in the area averaged by the XPS beam spot. To further investigate the chemical state and the nature of bonding of aluminum, nitrogen and oxygen, high resolution XPS scans were acquired for* Ti2p, O1s, Al2p *and* N1s *orbitals, for both prepared composites, as shown in figure 5.9. The high–resolution scans are collected after an etching time of* $900sec$*, so that the information provided is ascribable to the volume fraction in the bulk of the composite.*

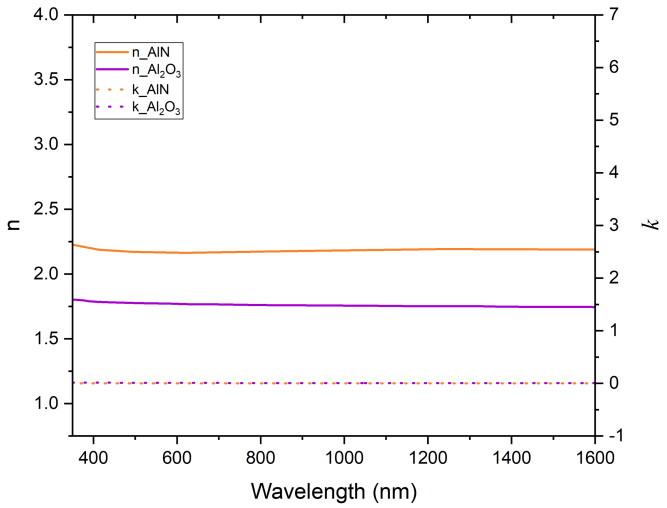

Figure 5.7: Refractive index n and extinction coefficient k for AlNand Al_2O_3.

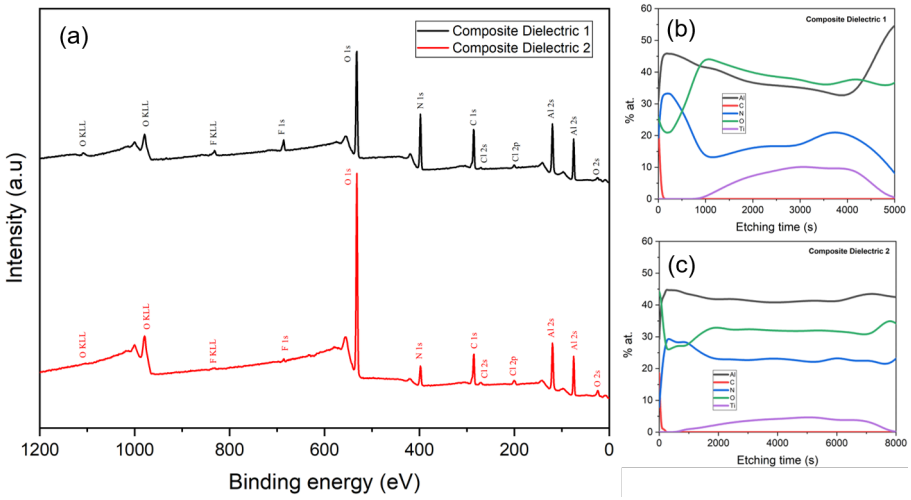

Figure 5.8: XPS results of the two composite dielectrics. (a) Survey scans of composite dielectric I and II. (b) Elements present during XPS scan of composite dielectric I, until reaching the Si interface. (c) Elements present during XPS scan of composite dielectric II, until reaching the Si interface.

The complex combination of peaks and satellite features of Ti2p *peak, as shown in figure 5.9(a), is ascribable to* TiN , TiO_2 *and* TiO_xN_y *[214, 215]. The high resolution scan of* Ti2p *for composite dielectric II shows the analysis with fitting of the background,* TiN, TiO_xN_y, TiO_2 *along with a perfect fitting of the experimental data. Similar general features were obtained for the* Ti2p *of composite dielectric 1, which is not detailed further here. The first* Ti2p3/2 *peak and the third* Ti2p1/2 *peak at* 454.7eV *and* 460.6eV *respectively, are signature of* TiN. *The shaded yellow region in the figure 5.9(a) shows the analysis for the* TiN *reference that was created by physical vapour deposition (PVD) in our laboratory. The binding energy of our experimental data compares well with that of the internal reference. The satellite features shown in cyan may be attributed to* TiO_xN_y *and* TiO_2, *which also supports the presence of oxygen in the composite. This could have happened due to the exposure of* TiN *NPs with atmospheric oxygen over a long time.*

The peak of Al2p *appears at* 75.6eV *for both the composites. Due to the closeness of the* Al2p *energies from* $Al-O$ *and* $Al-N$*[216, 217] the observed peak cannot unambiguously be associated to one of the species. On the other hand, the presence of both oxygen and nitrogen in our composites suggests that the observed* Al2p *peak includes the contribution of both species. The* N1s *peak is observed at* 397.9eV *for both composites. As with the* Al2p *peak, the measured binding energy value of* N1s *is compatible with the cases of* N *bonded to* Al *and* N *bonded to* Ti *[218], which are nevertheless both present in the composites. Moreover, aluminium oxynitride* AlON *shows* Al2p *energy of similar values preventing a clear assessment of the possible oxidized species. A single* O1s *peak was observed at* 532.5eV. *According to the literature, the binding energy of* O1s *peak for metal oxides appears at* $529-530$eV *[219]. This makes it clear that no* TiO2 *is present. The energy of observed* O1s *peak matches pretty well the case of* O *bonded to* Si *[220] from the substrate. The observed energy is also very close to the energy of* O *linked to* Al (531.1eV) *which*

justifies that a fraction Al_2O_3 *is also present in the composites. It is also possible to have a fraction of oxygen from* $Ti-O-N$ *and* $O-Ti-O$*, the energy which was observed in the high resolution scan of* Ti2p*. There is also a high probability that the oxygen is chemisorbed on the surface of the* TiN *nanoparticles, as the naked particles were in contact with the air for a long time after deposition.*

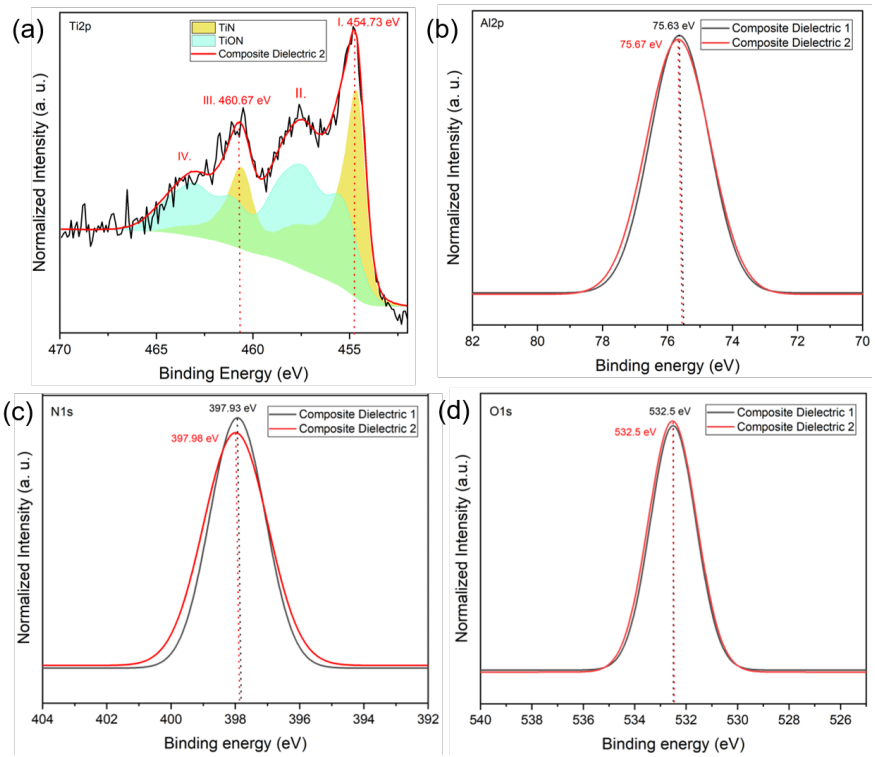

Figure 5.9: The comparison of narrow scans acquired after 900sec of Ar+ sputtering, of composite–1 and composite–2: (a) Ti2p, (b) Al2p, (c) N1s, (d) O1s.

From the above analysis, it is fair to say that there is a thorough consistency in the two composites, in terms of synthesis of AlN *thin films by* PE–ALD*, from the two approaches, and chemical composition. Furthermore, no other element was detectable in the XPS scans that distinctively shows the stability of* TiN *and* AlN*. In addition, no material diffused into any other during their synthesis.*

After a clear idea revealed from the XPS analysis, it was fair to divide each composite into two layers. The upper layer called layer 1 that is a mixture of AlN and Al_2O_3, and the core of the composite with layer 2 that was a mix of AlN, $Al_2O_3$and TiN. The decision of dividing the entire composite into two layers was done after a deep analysis on the high resolution scan for the composite II. It was proved with the cross-sectional SEM images that average thickness of the composite II was 300nm. The figure below shows the table as received after XPS analysis with the elemental presence from 0sec to 9000sec of etching for composite II.

For better understanding of the prepared composites, we made our own calculations and made some useful conclusions from them that helped us in preparing the numerical

Etching time (sec)	Al 2p%	C 1s%	N 1s%	O 1s%	Si 2p%	Ti 2p%
0	30.8901	24.0605	19.326	25.7234	0	0
60	43.7429	1.87303	31.7781	22.606	0	0
120	45.6366	0	33.0454	21.318	0	0
180	45.9186	0	33.2582	20.8232	0	0
240	45.6893	0	33.2464	21.0643	0	0
300	45.861	0	32.7461	21.3928	0	0
600	44.1231	0	25.6646	30.2123	0	0
900	41.3641	0	13.4222	45.2138	0	0
1200	36.1158	0	11.0536	44.0148	6.80809	2.00778
1800	23.8523	0	10.2591	30.3234	31.136	4.42922
2400	14.9929	0	7.10337	18.6599	55.6114	3.63247
3000	8.27284	0	3.78356	10.3083	75.1361	2.49917
3600	4.47512	0	2.94371	5.3637	85.9855	1.23195
4200	2.00341	0	1.28912	2.55892	93.4769	0.671639
4800	1.2947	0	0.304104	0.832692	97.5685	0
5400	0.772069	0	0	0.495349	98.7326	0
6000	0	0	0	0.199836	99.8002	0
6600	0	0	0	0	100	0
7200	0	0	0	0	100	0
7800	0	0	0	0	100	0
8400	0	0	0	0	100	0
9000	0	0	0	0	100	0

Ignored- presence of Carbon

Layer 1 – Al_2O_3 + AlN
vf - 0.645 0.355

Layer 2 – Al_2O_3 + AlN + TiN
vf - 0.61 0.224 0.165

Dielectric Composite II

Subtracted Si and SiO_2 content

Ignored- presence of Silicon

Figure 5.10: The table with complete elemental presence from 0sec to 9000sec of etching done for composite II.

models and further the experimental ellipsometric models. The important things that we considered in the calculations made by us were the following:

1. We completely ignored the information at 0sec and 60sec (marked in red) etching timing because it had high content of impurities as shown in C1s%.

2. Information from 120sec until 900sec (marked in light blue) was considered as the upper layer 1 where there is no presence of C, Si and Ti . Layer 1 only had the presence of AlN and Al_2O_3 as discussed above.

3. Information from 1200sec until 4200sec (marked in purple) was considered as the bottom layer 2 with the presence of Si and Ti along with Al, N, O. This is considered as the core of the two composites.

4. Information from 4800sec until 6000sec (marked in yellow), the Si and SiO_2 content was subtracted from the calculations.

5. Information from 6600sec until 9000sec (marked in red) were completely eliminated from the calculations because of the absence of all other elements except a major presence of Si and minor presence of O and Al which also disappears completely from 6600sec of etching.

Estimations of the volume fractions of AlN, Al_2O_3 and TiN present in layer 1 and layer 2 are shown here. For layer 1 it proceeds as follows; from 120sec until 900sec of etching the average percentage of Al2p present is 44.76, N1s is 28.56 and O1s is 26.67. Now assuming that these 28 atoms of N are linked to 28 atoms of Al, making altogether 28 molecule of AlN. This means that only 16 atoms of Al out of the total 44 are left to link with 26 atoms of O. Therefore, for Al_2O_3, 8 atoms of Al combines with 24 atoms of O. According to the counting, there were 26 atoms of O in total, but we let go the remaining 2 atoms assuming these calculations are just approximative.

$$v_{\mathrm{AlN}} = \frac{\mathrm{atomicmassofAlN}}{\mathrm{densityofAlN}} = 13.4\mathrm{cm}^3 \tag{5.1}$$

$$v_{Al_2O_3} = \frac{\text{atomicmassof}Al_2O_3}{\text{densityof}Al_2O_3} = 25.7\text{cm}^3 \tag{5.2}$$

Here, v_{AlN} is the molar volume of AlN, $v_{Al_2O_3}$ is the molar volume of Al_2O_3. Thus, the total volume of AlN is $V_{AlN} = 28 \times 13.4 = 375.2\text{cm}^3$ and the total volume of Al_2O_3 is $V_{Al_2O_3} = 8 \times 25.7 = 206.1\text{cm}^3$. Thus we deduce the volume fractions in layer 1 to be

$$vf_{AlN} = \frac{V_{AlN}}{V_{AlN}+V_{Al_2O_3}} = 0.645 \tag{5.3}$$

$$vf_{Al_2O_3} = \frac{V_{Al_2O_3}}{V_{AlN}+V_{Al_2O_3}} = 0.355 \tag{5.4}$$

In a similar way calculations for layer 2 proceeds; from 1200sec until 4200sec of etching the average percentage of Al2p present is 35, N1s is 17.44, O1s is 38.54 and Ti2p is 8.10. Now assuming that these 8 atoms of Ti are linked to 8 atoms of N, making altogether 8 molecules of TiN. This means that only 9 atoms of N out of the total 17 are left to link with 9 atoms of Al making altogether 9 molecules of AlN. The remaining 26 atoms of Al are bonded to 13 atoms of O making 13 atoms of Al_2O_3. The molar volume of the atom of TiN is

$$v_{TiN} = \frac{\text{atomicmassof}TiN}{\text{densityof}TiN} = 11.5\text{cm}^3 \tag{5.5}$$

Thus, the total volume of AlN is $V_{AlN} = 9 \times 13.4 = 120.6\text{cm}^3$, for Al_2O_3 is $V_{Al_2O_3} = 13 \times 25.7 = 334.1\text{cm}^3$and for TiN is $V_{TiN} = 8 \times 11.4 = 91.2\text{cm}^3$. Thus we deduce the volume fractions in layer 2 to be

$$vf_{AlN} = \frac{V_{AlN}}{V_{AlN}+V_{Al_2O_3}+V_{TiN}} = 0.224 \tag{5.6}$$

$$vf_{Al_2O_3} = \frac{V_{Al_2O_3}}{V_{AlN}+V_{Al_2O_3}+V_{TiN}} = 0.610 \tag{5.7}$$

$$vf_{TiN} = \frac{V_{TiN}}{V_{AlN}+V_{Al_2O_3}+V_{TiN}} = 0.165 \tag{5.8}$$

For calculating the thickness of the two layers of the composite II we made a calculation as shown below:

$$t_1 = \left[\frac{(1050-120)}{(4200-120)}\right] \times L \simeq 68\text{nm} \tag{5.9}$$

$$t_2 = \left[\frac{(4200-1050)}{(4200-120)}\right] \times L \simeq 232\text{nm} \tag{5.10}$$

where, L is 300nm, the total average thickness considered for the composite, 4200sec is the time of etching when TiN completely disappears and high Si signal appears, 1050sec is the time during etching when the AlN and Al_2O_3 signal from the upper oxidized layer disappears and TiN signal begins to appear, 120sec is the time when the etching starts,

Etching time (s)	Al 2p %	C 1s %	N 1s %	O 1s %	Si 2p %	Ti 2p %
0	30.8901	24.0605	19.326	25.7234	0	0
60	43.7429	1.87303	31.7781	22.606	0	0
120	45.6366	0	33.0454	21.318	0	0
180	45.9186	0	33.2582	20.8232	0	0
240	45.6893	0	33.2464	21.0643	0	0
300	45.861	0	32.7461	21.3928	0	0
600	44.1231	0	25.6646	30.2123	0	0
900	41.3641	0	13.4222	45.2138	0	0
Total	268.5927		171.3829	160.0244		
%	44.76545	0	28.56382	26.67073		
	14.9218167					

Etching time (s)	Al 2p %	C 1s %	N 1s %	O 1s %	Si 2p %	Ti 2p %	Subtract Si	(6.8*2)% of O	O-SiO2	Si-SiO2	Total of Rows
1200	41.4144	0	12.67529	43.60805	6.80809	2.302344	93.19191	5.9860128	38.02879	87.2059	100.0000803
1800	36.84321	0	15.84661	40.46866	31.136	6.841549	68.864	4.1239824	26.19942	64.74002	100.0000309
2400	35.8246	0	16.97306	38.52288	55.6114	8.67956	44.3886	2.5377464	16.12215	41.85085	100.0000956
3000	35.26063	0	16.12635	37.96088	75.1361	10.652	24.8639	1.4019288	8.906371	23.46197	99.99987213
3600	33.68542	0	22.15809	34.88313	85.9855	9.273215	14.0145	0.7294632	4.634237	13.28504	99.99984945
4200	32.44343	0	20.87614	35.80366	93.4769	10.87659	6.5231	0.34801312	2.210907	6.175087	99.99982186
	215.4717		104.6555	231.2473		48.62526				236.7189	599.9997502
%	35.91195		17.44259	38.54121		8.104211					99.99995837

Figure 5.11: Calculations made to retrieve the vf of the compounds present in the composite II.

t_1 is the thickness of the upper layer 1 of the composite and t_2 is the thickness of the core layer 2 of the composite. We considered that the interface between layer 1 and layer 2 is at midway between 900sec and 1200sec which is 1050sec. It was hypothesized that having an average approximation of thickness for the two layers t_1, t_2 would be a reference in the subsequent calculations.

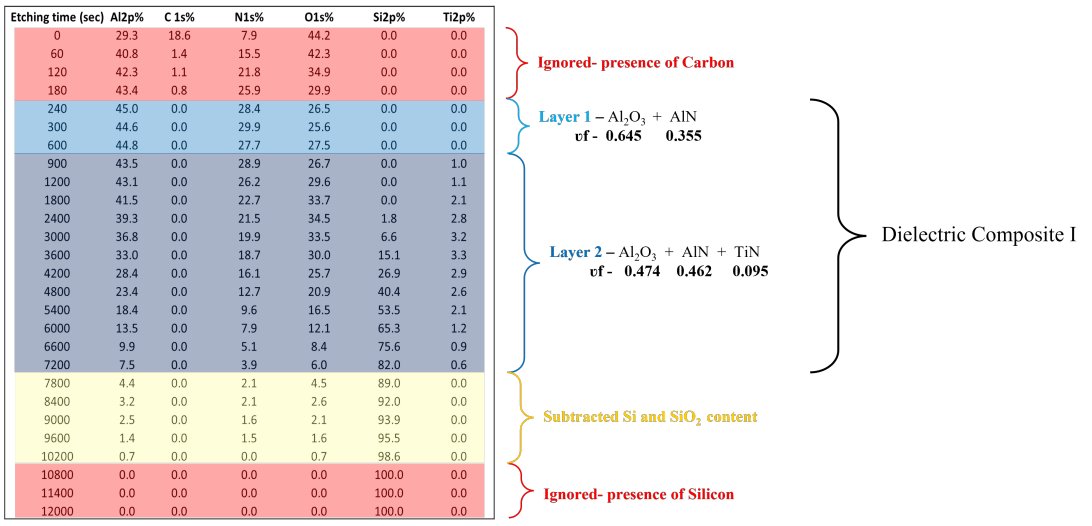

Figure 5.12: The table with complete elemental presence from 0sec to 12000sec of etching done for composite I.

A similar XPS study was made for composite I. The table in figure 5.12 shows the presence of elemental composition for composite II.

Here, v_{AlN} is the molar volume of AlN, $v_{\mathrm{Al_2O_3}}$ is the molar volume of Al_2O_3. Thus, the total volume of AlN is $\mathrm{V_{AlN}} = 28 \times 13.4 = 375.2\mathrm{cm}^3$ and the total volume of Al_2O_3 is $\mathrm{V_{Al_2O_3}} = 8 \times 25.7 = 206.1\mathrm{cm}^3$. Thus we deduce the volume fractions in layer 1 to be

$$vf_{\mathrm{AlN}} = \frac{\mathrm{V_{AlN}}}{\mathrm{V_{AlN}} + \mathrm{V_{Al_2O_3}}} = 0.645 \tag{5.11}$$

$$vf_{Al_2O_3} = \frac{V_{Al_2O_3}}{V_{AlN}+V_{Al_2O_3}} = 0.355 \tag{5.12}$$

In a similar way calculations for layer 2 proceeds; from 900sec until 7200sec of etching the average percentage of Al2p present is 42.4, N1s is 23.8, O1s is 30.5 and Ti2p is 3.29. Thus we deduce the volume fractions in layer 2 to be

$$vf_{AlN} = \frac{V_{AlN}}{V_{AlN}+V_{Al_2O_3}+V_{TiN}} = 0.462 \tag{5.13}$$

$$vf_{Al_2O_3} = \frac{V_{Al_2O_3}}{V_{AlN}+V_{Al_2O_3}+V_{TiN}} = 0.474 \tag{5.14}$$

$$vf_{TiN} = \frac{V_{TiN}}{V_{AlN}+V_{Al_2O_3}+V_{TiN}} = 0.095 \tag{5.15}$$

Etching time (s)	Al 2p%	C 1s%	N1s%	O1s%	Si2p%	Ti2p%
0	29.3	18.6	7.9	44.2	0.0	0.0
60	40.8	1.4	15.5	42.3	0.0	0.0
120	42.3	1.1	21.8	34.9	0.0	0.0
180	43.4	0.8	25.9	29.9	0.0	0.0
240	45.0	0.0	28.4	26.5	0.0	0.0
300	44.6	0.0	29.9	25.6	0.0	0.0
600	44.8	0.0	27.7	27.5	0.0	0.0
Total	134.4		86.0	79.6		
%	44.7888		28.67393	26.53723		

Etching time (s)	Al 2p%	C1s%	N1s%	O1s%	Si2p%	Ti2p%	Subtract Si	(6.8*2)% of O	O-SiO2	Si-SiO2	Total of rows
900	45.1	0.0	30.0	23.9	0.0	1.0	100.0	3.6275552	23.0456448	96.4	100.0
1200	44.9	0.0	27.3	26.7	0.0	1.1	100.0	4.0270008	25.5832992	96.0	100.0
1800	43.5	0.0	23.8	30.5	0.0	2.2	100.0	4.584628	29.1258720	95.4	100.0
2400	42.1	0.0	23.0	31.9	1.8	3.0	98.2	4.69744	29.8425600	93.5	100.0
3000	41.4	0.0	22.4	32.5	6.6	3.6	93.4	4.5498256	28.9047744	88.8	100.0
3600	40.8	0.0	23.2	32.0	15.1	4.1	84.9	4.0783544	25.9095456	80.9	100.1
4200	40.8	0.0	23.1	31.9	26.9	4.2	73.1	3.4920176	22.1845824	69.7	99.9
4800	41.2	0.0	22.4	31.7	40.4	4.6	59.6	2.8371368	18.0241632	56.8	99.9
5400	41.5	0.0	21.8	32.1	53.5	4.7	46.5	2.2380432	14.2181568	44.3	100.1
6000	40.8	0.0	23.8	31.7	65.3	3.6	34.7	1.6469192	10.4627808	33.0	100.0
6600	42.7	0.0	22.0	31.3	75.6	3.9	24.4	1.145732	7.2787680	23.3	99.9
7200	43.9	0.0	22.9	29.9	82.0	3.5	18.0	0.80967056	5.1437894	17.2	100.2
	508.7		285.8	366.2		39.5					
%	42.4		23.81585	30.51614		3.29507					

Figure 5.13: Calculations made to retrieve the vf of the compounds present in the composite I.

For calculating the thickness of the two layers of the composite I we made a calculation as shown below:

$$t_1 = \left[\frac{(750-240)}{(7200-240)}\right] \times L \simeq 22nm \tag{5.16}$$

$$t_2 = \left[\frac{(7200-750)}{(7200-240)}\right] \times L \simeq 278nm \tag{5.17}$$

where, L is 300nm, the total average thickness considered for the composite, 7200sec is the time of etching when TiN completely disappears and high Si signal appears, 750sec is the time during etching when the AlN and Al_2O_3 signal from the upper oxidized layer disappears and TiN signal begins to appear, 240sec is the time when the etching starts, t_1 is the thickness of the upper layer 1 of the composite and t_2 is the thickness of the core layer 2 of the composite. We considered that the interface between layer 1 and layer 2 is at midway between 600sec and 900sec which is 750sec. It was hypothesized that having

an average approximation of thickness for the two layers t_1, t_2 would be a reference in the subsequent calculations.

A few things worth summarizing here are:

- These calculations were done both for composite I and II to have an average approximation for the presence of AlN, Al_2O_3 and TiN in the composites.
- The presence of lot of Al_2O_3could be justified by the following; first, the exposure of the composites with the air. The two composites was in contact with the atmospheric oxygen for a lot of time during their deposition process that led the AlN thin film to oxidize. Second, the presence of oxygen contamination sources (e.g. moisture) in the reactor chamber and/or in the precursor or gas lines caused the presence of Al_2O_3 within the AlN thin films.
- After getting an idea for the presence of AlN, Al_2O_3 and TiN in the two composites, they were divided into layer 1 and layer 2 to better understand their structure experimentally and numerically. The optical study of composite I and II on the basis of layer 1 and layer 2 is done in detail later in the chapter.
- In the figure 5.5 SEM images clearly indicate that composite II is thicker than composite I, however it is not feasible to exactly mention the difference in the thickness of the two composites because of their rough surface. Despite of the difference in thickness, in the calculations done above, the average thickness for both composite I and II was taken as 300nm. This was done because in case of composite I, the etching time was much longer than in case of composite II. This could be easily concluded by the fact that the etching area in case composite I was thicker (due to the presence of the agglomerates) than in composite II.
- The presence of AlN and Al_2O_3 present in layer 1 of the two composites is identical, that makes a good sign and consistency in the two composites. However, there is a lot of difference in the presence of AlN, Al_2O_3 and TiN in the layer 2 of the two composites despite identical synthesis methods. This can be explained by the following; first, in case of composite II the deposition of AlN thin films is on a larger surface area (due to the presence of more TiN NPs and larger chunks of TiN) than in composite I. This becomes the source for the presence of Al_2O_3. Second, starting with vf of 19TiN NPs in the layer 1, the vf reduces to 9.5% in the layer 7 for composite I. However, in case of composite II, the vf reduces to 16.5 starting from 22. This happened due to the rough surface for TiNdistribution that the previous layer provided for the next one.

The above calculations were done for both composites I and II to have an average approximation, benefiting to have more structural idea for composite I and II. These calculations are just approximative and depends largely on the area of the composite being etched, and the thickness of the composite in that region.

5.1.3 Electrical Conductivity Measurement

Considering the perspective application of the composite, as one of the major components in solar selective coatings, it is necessary for the composite to behave as a dielectric. To test the electrical behaviour of the composite, impedance spectroscopy measurements were carried out using a Novocontrol Alpha-A Impedance Measurement System. Conductivity can be deduced from the impedance measurements for the known sample geometry. All measurements were made at room temperature.

The high roughness of the composite made it necessary to cover both sample faces with a metallic layer (Platinum, Pt*) to create a constant electric potential across the surfaces. This was done by coating both sides of the sample with a* 10nm *film of* Pt*, by sputtering technique using Leica EM bottom surfaces of the sample, hence the silicon substrate itself is part of the measured materials sandwich. In order to distinguish the impedance behaviour of the composite from that of the silicon substrate, a reference sample was prepared in which the* Pt *was deposited on the two surfaces of a silicon substrate only. The samples were then placed between the two parallel plates of the sample holder of the spectrometer. The platinum* Pt *layer ensured a good electrical connection between the entire (rough) surface of the composite and the (flat) top electrode of the sample holder. Due to the non–regular thickness of the composites, the impedance results have been referred to the average thickness within the electrode area. Figure 5.14 shows the results of impedance spectroscopy measurements, in terms of impedance module $|Z|$ as function of frequency. Although bare Si has a resistive behaviour throughout the frequency range investigated, at high frequencies, the samples including the composite multilayer behave as capacitors (one order of magnitude decrease in $|Z|$) per one order of magnitude increase in frequency), as expected. At low frequencies, composite samples basically behave as resistors, as $|Z|$ does not depend on frequency. In this region, we observe a difference of about one order of magnitude in the resistive component of the composite. However, considering both the resistive part at low frequencies and the capacitive part at high frequencies, we observe that the cut–off frequencies of the two composites* $1/\mathrm{RC}$ *are separated by one order of magnitude, in good agreement with resistance difference. This suggests that the capacitive behaviour of the two composites is basically the same.*

5.2 Results related to the optical performance of the composite

5.2.1 Retrieval of optical constants n, k for composite I and II, prepared numerically.

XPS analysis has been explained in 5.1.2 with all the details for two experimentally synthesized composite. Through the analysis, we became aware of the presence of additional compounds in the composite, than expected. The *vf* of the compounds present in the composite, and the thickness of the two layers that the composite dielectric was divided into, helped us in constructing the numerical micro and macro model similar to the composite

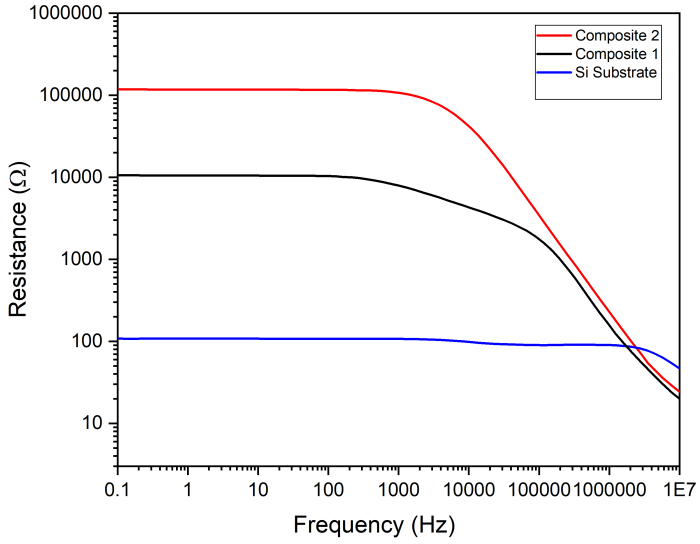

Figure 5.14: Electrical conductivity measurement of dielectric composite 1, 2 and bare Si substrate.

that was achieved experimentally.

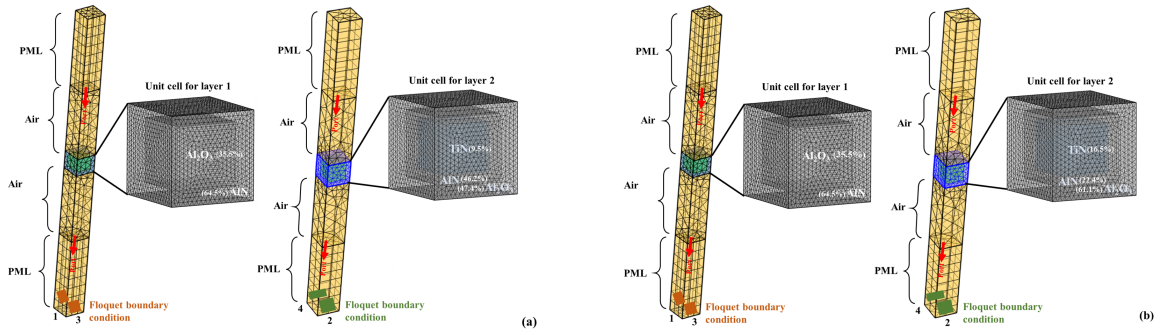

Figure 5.15: Numerical construction of a unit cell for layer 1 and layer 2 for the retrieval of n and k. (a) For composite I (b) For composite II.

Figure 5.15shows the modelled unit cells for layer 1 and layer 2 according to the outcomes of the XPS calculations made above. *The left unit cell of the figure 5.15(a) and (b) shows the computational domain, with an* Al_2O_3 *buried in a* AlN *matrix for layer 1. The unit cell on the right of the figure 5.15(a) and (b) shows* TiN *and* AlN *buried in* Al_2O_3 *matrix for layer 2. The equation 3.2 is solved by considering the following boundary conditions:*

- *Perfectly matched layer (PML), at extremities of computational domain to mimic an infinite space. The thickness of PML and air was taken to be half the wavelength* $\lambda/2$ *for each.*
- *The interface surfaces between the PML and the air, are set as ports from which the*

excitation of the incident wave is activated and also where the scattering coefficients Sij *are computed.*

- *The Floquet periodic boundary condition is applied to the two by two transversal sides of the computational domain to simulate infinity large surface.*

The S-parameters are calculated for two unit cells corresponding to layers 1 and 2 as explained in annex 6.1, and then optical constants n *and* k *are retrieved from the S-parameters as explained in annex 6.1 . The results for optical constants* n *and* k *from these numerical models will be compared to optical constants obtained experimentally from SE, in the following section.* **Note that the process explained above for the construction of the nanoscale model corresponding to the experimentally prepared composite was done separately for composite I and composite II, according to the separate calculations done for composite I and II in the XPS section 5.1.2.**

5.2.2 Retrieval of optical constants n, k, experimentally, for composite I and II from the Spectroscopic Ellipsometer (SE)

In order to validate the effectiveness of numerical modelling the same measurements were made experimentally. Considering an extensive range of susceptibility of ellipsometry, the potential of implementing the technique as a reliable and a decent numerical method, qualified for the prediction of the result for real experimental analysis before implementing it, clearly results exceptionally convenient. This is particularly true when the target of the study is the system with complex nano-structures. Here, we present a reliable and straightforward method, providing a comprehensive SE *analysis for a complex multi-layer systems with nanoparticles integrated inside the layers, with flexibility of design in terms of composition, thickness and number of layers. For each composite, the* SE *allows the calculation of the main optical quantities of interest which includes* n *and* k *for each of the layers along with their thickness and total surface roughness.* SE *analysis was performed over the spectrum of apparatus bulb, from* 370nm *to* 1600nm*. To better investigate the optical performance of the two composites, two angle of incidences were taken for the measurements* 50° *and* 75° *. Identical values from both* n *and* k *were received at* 50° *and* 75° *. Hence only the values obtained at* 50° *have been highlighted in the work. A standard model for the analysis of both composite I and II was created reflecting the characteristics of the real sample. We began with creating a model on* Si *wafer with a thickness of* 300μm *with a thin layer of* 10nm *of* SiO_2 *on top of Si wafer. A Cauchy model for Layer 2 was built that was treated as the core of the composite with the* AlN, Al_2O_3 *and* TiN*. Conducting* TiN *nano fillers were present between a mix of* AlN *and* Al_2O_3 *transparent film, this is why Cauchy absorbent was considered as a dispersion law for layer 2. Usually 'Cauchy Absorbent' is suitable to describe the optical properties when the material is weakly absorbing. The percentage of* TiN *in the composite is just* 20 *which makes it weakly*

absorbing. The formulation for Cauchy absorbent is:

$$\mathrm{n}(\lambda) = \mathrm{A} + \frac{10^4.\mathrm{B}}{\lambda^2} + \frac{10^9.\mathrm{C}}{\lambda^4} \tag{5.18}$$

$$k(\lambda) = 10^{-5}.\mathrm{D} + \frac{10^4.\mathrm{E}}{\lambda^2} + \frac{10^9.\mathrm{F}}{\lambda^4} \tag{5.19}$$

A total of six parameters are used in the equation of Cauchy absorbent model, where A is a dimensionless parameter. B (nm^2) affects the curvature and amplitude of the refractive index for medium wavelengths in the visible region. C (nm^4) *affects the curvature and amplitude for shorter wavelengths in the UV. Generally,*

$$0 <\mid C \mid <\mid B \mid < 1 < A \tag{5.20}$$

The three fit parameters that describe the extinction coefficient are, D which is a dimensionless parameter similar to A, E (nm^2) *is analogous to B, and F* (nm^4) *behaves like C. Then on top of absorbent layer 2, layer 1 with 'Cauchy Transparent' dispersion law was considered. This layer is a mixture of AlN and Al_2O_3 which are transparent in the visible region of the spectrum, which makes $k(\lambda) = 0$ for this equation, i.e. the terms D, E and F do not exist.*

$$\mathrm{n}(\lambda) = \mathrm{A} + \frac{10^4.\mathrm{B}}{\lambda^2} + \frac{10^9.\mathrm{C}}{\lambda^4} \tag{5.21}$$

$$k(\lambda) = 0 \tag{5.22}$$

The Cauchy transparent dispersion equation works best when the material has no optical absorption in the visible spectral range and therefore generally has a normal dispersion which means decreasing n *with increasing wavelength.*

Surface roughness was something that could not be ignored in our case where the two kind of composites showed intense roughness. Therefore an additional layer was added on top of the model with the characteristics of real surface roughness considering a gradient. To create the model, for the two layers above, $\mathrm{t}_1, \mathrm{t}_2$ *were at first kept fixed to* 68nm *and* 232nm *respectively (the values calculated by XPS data). This way the values for both layers for parameters* A, B, C, D, E *and* F *were obtained. Upon generating a standard model, after achieving the values for the six parameters, the thickness* $\mathrm{t}_{1,}\mathrm{t}_2$ *and roughness were fitted each time while analysing three different samples each for composite I and II.*

Figure 5.16 shows a table with the the fitting parameters of the model that was used for the retrieval of the optical constants from SE measurements. The thickness $\mathrm{t}_1, \mathrm{t}_2$ *and* S_R *obtained for three different samples of Composite I and II have been clearly mentioned in the table along with the value of Cauchy parameters for each layer of each sample. The following is worth summarizing here;*

- *There is uniformity in optical properties of all the samples of composite I and II*

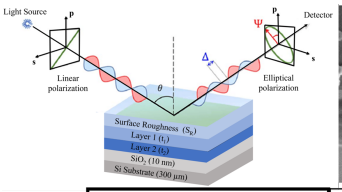

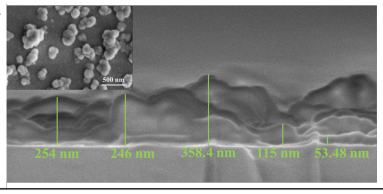

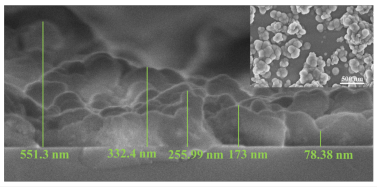

Spectroscopic Ellipsometer Model	Composite I			Composite II		
	Sample i	Sample ii	Sample iii	Sample i	Sample ii	Sample iii
Surface Roughness (S_R)	68.5	80	64.5	115.5	79.2	71.5
Layer 1- Cauchy Transparent (t_1)	48.3	55	55	44	84.8	91.4
Layer 2- Cauchy Absorbent (t_2)	192.5	180	198	281.8	294.6	296.4
SiO_2 (10 nm)						
Si Substrate (300 µm)						

	Layer 1	Layer 2	Layer 1	Layer 2	Layer 1	Layer 2	Layer 1	Layer 2	Layer 1	Layer 2	Layer 1	Layer 2
A	1.809	2.973	1.809	2.973	1.809	2.973	1.809	2.973	1.809	2.973	1.809	296.43
B	-0.219	-0.732	-0.219	-0. 732	-0.219	-0.783	-0.219	-0.732	-.0219	-0.732	-0.219	-0.732
C	0.025	0.097	0.025	0.097	0.025	0.095	0.025	0.097	0.025	0.097	0.025	0.097
D	0.003	0.0003	0.003	0.288	0.003	0.376	0.003	0.686	0.003	0.704	0.003	0.667
E	0	0.092	0	-0.02	0	-0.167	0	-0.314	0	-0.316	0	-0.400
F	0	-0.002	0	0.006	0	0.027	0	0.057	0	0.064	0	0.095

Figure 5.16: A detailed table highlighting the thickness of layer 1 (t_1), layer 2 (t_2) and surface roughness (S_R) for three samples individually of composite I and composite II. Along, are also mentioned the Cauchy parameters for layer 1 and 2 for each of the sample.

which also show good reproducibility among the samples hence approving the synthesis technique used for the composites;

- *the values* t_1, t_2 *are consistent with the average values shown in the SEM images proving correct the decision made earlier of average coating thickness* L *(sum of* $t_1 +$ $t_2 +$ S_R*) being greater for composite II.* S_R *is also in range with what was achieved through SEM images;*

- *All the above conclusions favour the concept for a common successful model for such complicated structure of the two composites;*

- **There is difference in the thickness t_1 and t_2 for both composite I and II, obtained from XPS calculations in section 5.1.2 and from spectroscopic ellipsometer in section 5.2.2. This could be because the area on the composite I from where the XPS information was received had more agglomerates of TiN NPs, giving a higher average thickness for composite I. The area on the composite where the beam spot fell in case of XPS and ellipsometer, were not the same.**

5.2.3 Comparison of n and k of layer 1 and 2 for composite I and II prepared experimentally, along with the numerical macro model of the composite II

The above explanation created a clear base for the steps followed for retrieving n *and* k *for the complicated structure of the composite from* 370nm *to* 1600nm*. For better apprehension and precision of the working of the two composites in terms of absorptance and reflectance of light, it is better to have optical constants for both layer 1 and 2 for both composites I and II. In this section, a clear representation is made highlighting thorough differences and logical reasoning between the optical properties obtained experimentally and numerically.* n *and* k *were all retrieved at an incident angle of* 50° *from numerical simulations and ellipsometer.* ***In this part of the thesis, comparison of*** n ***and*** k ***of composite I and II is only done with numerical macromodel of the composite II. This was done for the sake of simplicity and for a collective understanding of composite I and II. However, in the annex, there is a comparison of*** n ***and*** k ***of composite I and II is only done with numerical macromodel of the composite I.***

In the section 5.2.1, the structure composition used for numerical calculation was based on XPS data, however the surface roughness was not taken into account in the model. In the wave optics module in COMSOL software do not allow for adding the roughness feature, but our samples show high degree of roughness and therefore it is worth accounting for in the calculations of n *and* k*. The approach we adopted to account for roughness is by adding a air phase inside the unit cell of* AlN *and* Al_2O_3*, as an alternative way to model the roughness. Considering the calculations made in section 5.1.2, the ratio of* Al_2O_3 *to* AlN *was kept constant and* 25% *of air was added along with the mix for layer 1. The figure5.17 shows the comparison of* n *and* k *of layer 1 of composite I and II. Three different samples of composite I and II marked as (_i, _ii, _iii), along with the prediction from numerical model, for a direct comparison. The solid line curves represents the refraction index* n *and the dotted curves represents the extinction coefficient* k *throughout in the graphs. The green curves represents the numerical prediction reflecting the upper layer 1 of the composite. The black curves (i) are for composite I and the red (ii) for composite II. The numerical model considers a homogeneous mixture for* AlN, Al_2O_3 *and air in the layer 1, for which* n *is quasi constant and* k *null over the spectrum as seen in 5.7, therefore the prediction looks consistent throughout the spectral range. For a mix of* AlN, Al_2O_3 *and air the values of* n *and* k *are quite justified and go well with the XPS analysis as shown in figure 5.10 for the initial few seconds of etching until reaching the core of the composite. Being a combination of three dielectrics, the value of* k *obtained experimentally from the different samples of the two different composites, remains almost zero making layer 1 completely transparent allowing the incident light to pass through, reaching the core of the composite. It is worth noting that the values of* n *and* k *for layer 1 of the three samples of composite I and II each are identical and thus overlap one another.*

The figure 5.18 shows the comparison of n *and* k *for the three samples each of composite*

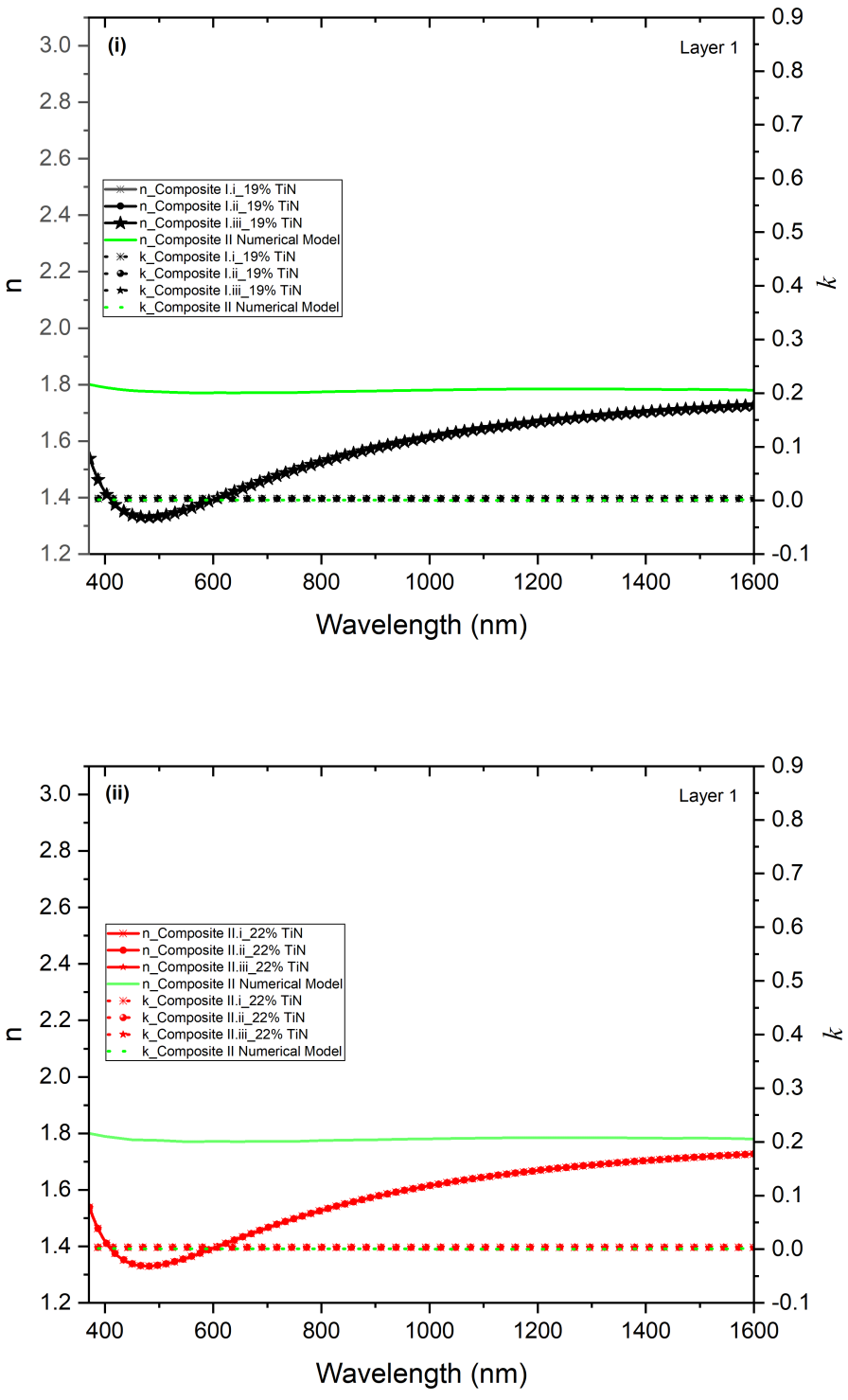

Figure 5.17: Comparison of optical contants obtained experimentally and numerically for layer 1 (i) Comparison of n and k of three samples of composite I with numerical model. (ii) Comparison of n and k of three samples of composite II with numerical model.

I and II along with the numerical prediction echoing layer 2. In the figure 5.18(i) the n *for sample i and ii are matching each other, whereas the* n *for sample iii is slightly lower in the VIS range. The k for the three samples of composite I is between* 0.1 *to* 0.35 *and is more or less consistent throughout the spectrum. The value of k for the numerical model shown in dotted green curve is much higher, particularly in VIS range. This is because the numerical simulations assumes an ideal case with a uniform periodic distribution of* TiN *inclusions throughout the dielectric in* $AlN + Al_2O_3$ *matrix which explain the destructive interference. The solid line curves highlighting* n *are all converging for IR region showing the same trend and moderate difference between them. The slight disparity between the different samples is due to the manual distribution of* TiN *inclusions in the composites. Since the* TiN *nanoparticles weren't distributed mechanically but manually throughout the layers in the composite, there were unavoidable chances of* TiN *NPs not being distributed homogeneously. This inhomogeneity caused formations of agglomerates and chunks laid in certain places causing light to behave differently. Higher k in figure 5.18(ii) clearly due to the presence of more* TiN *particles in case of composite II. The same can be seen through SEM images in the figure 5.5where the distribution of* TiN *NPs is* 22% *in case of composite II and* 19% *in case of composite I.*

The presence of conducting TiN *particles in the core of the composite described as layer 2, make its k much higher in the two composites compared to layer 1. Figure 5.19(i and ii) compares the refractive index between composites I and II. For both layer 1 and 2 along with the numerical prediction. Figure 5.19(i) compares the values of both* n *and k for the layer 1, the values corresponding to refractive index of composites I and II are lower than the numerical prediction in VIS range this is clearly an inaccuracy in SE fitting software, the dip around* 500nm *is characteristic to* TiN *refractive index as seen in 3.4 in chapter 3. The figure 5.19(ii) shows a comparison of optical constants of layer 2 for composite I, II and the numerical model. Despite of the manual control of distribution of* TiN *NPs, it can be appreciated that the values for optical constants for three samples each for composite I, II and numerical prediction were quite consistent and in a comparable range. This is also a very clear indication that all experimentally prepared samples were reproducible.*

5.2.4 Comparison of reflectance of the composites I, II prepared experimentally, along with the numerical macro model of the composite

Given the parameters, the diameter D *of* TiN *NPs, the vf of* TiN *NPs inside* AlN *matrix and the interspacing* d between the TiN NPs, explained in *section 4.4, for achieving the maximum absorption in the visible spectrum and the maximum reflectance in the IR spectrum, we retrieved the effective parameters of the homogenized composite dielectric in terms of refractive index* (n) *and extinction coefficient (k) as explained in section 5.2.1* To numerically examine the performance of the composite synthesized experimentally, the nanoscale model for both composite I and II was successfully refined according to the outcomes of the experimentally prepared composite. *The values of* n *and k obtained*

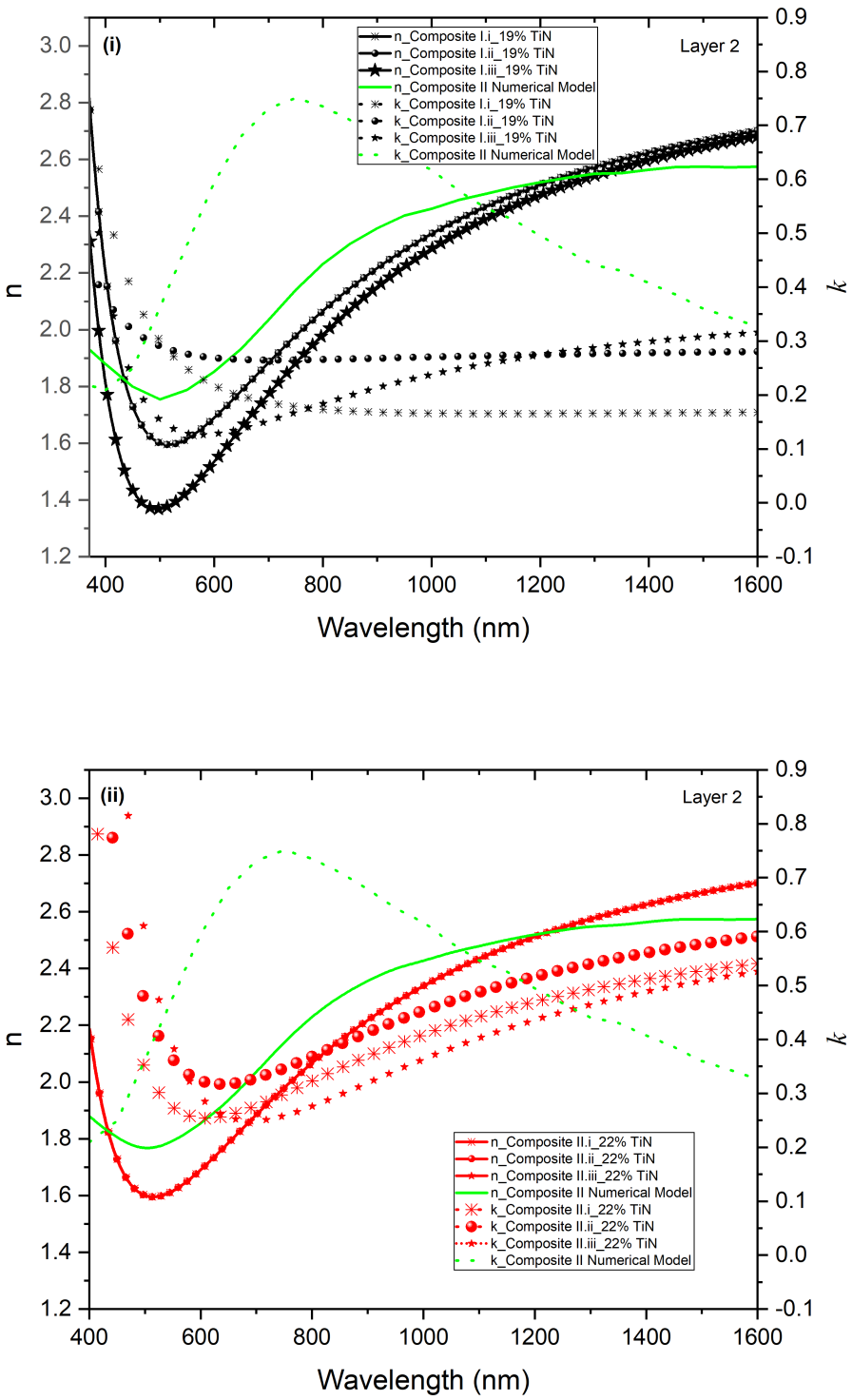

Figure 5.18: Comparison of optical contants obtained experimentally and numerically for layer 2 (i) Comparison of n and k of three samples of composite I with numerical model. (ii) Comparison of n and k of three samples of composite II with numerical model.

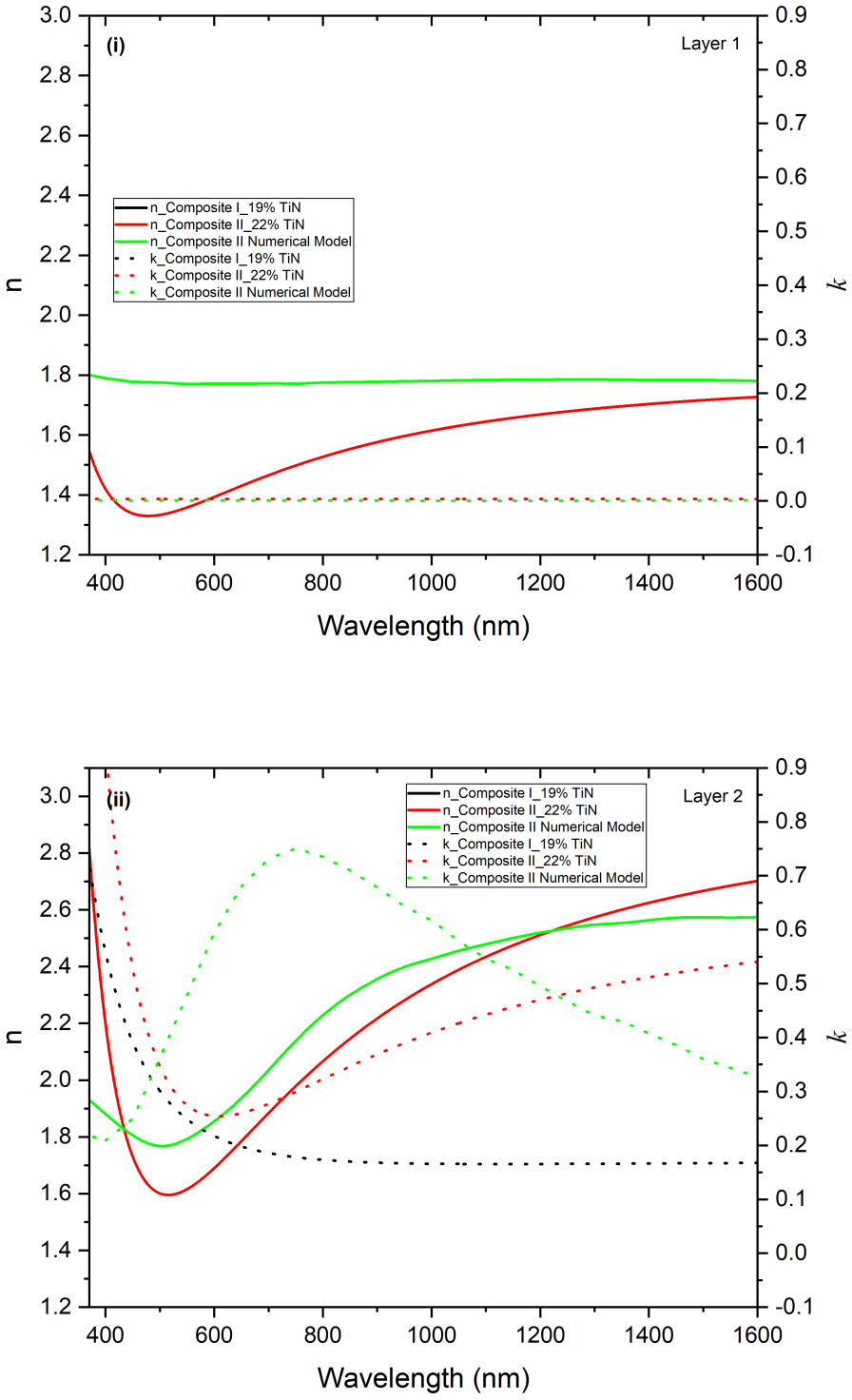

Figure 5.19: (i) Comparison of n and k of composite I, II and numerical model. (ii) Comparison of n and k of composite I, II and numerical model.

from these nanomodels now help us in obtaining the reflectance of the macro–model that corresponds to the experimentally prepared composite.

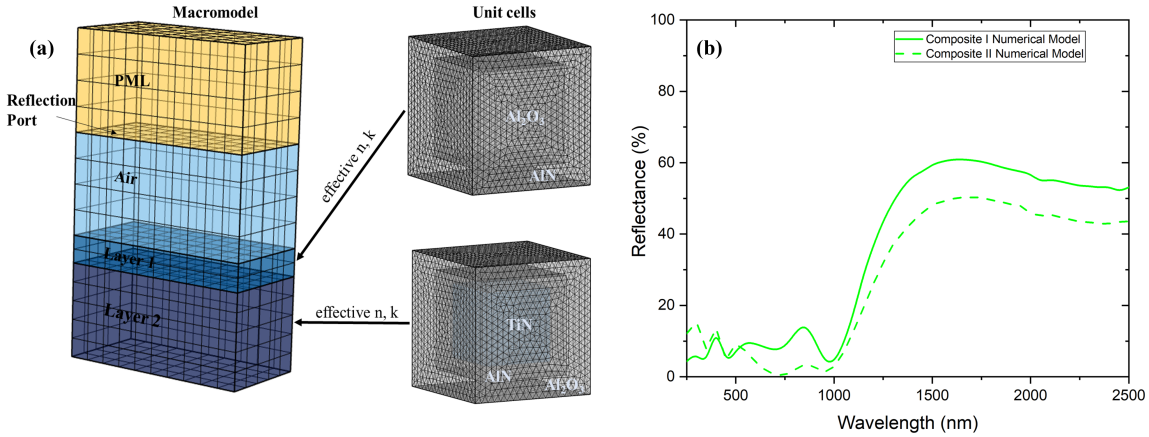

Figure 5.20: (a) Figure showing the constructed macromodel with n and k for different unit cells fed in the macromodel. (b) Reflectance obtained from the numerical macromodel I and II, corresponding to the experimentally synthesized model.

The macro-model describing the complete structure of the composite was successively refined according the outcomes of the experimental work. These regarded in particular the total thickness and the presence of a certain fraction of alumina (Al_2O_3) *in layers (see XPS results in subsection 5.1.2). Figure 5.20(a) shows a common computational model of the homogenized media with a thinner layer 1 on top of a much thicker layer 2 for composite I and II. The effective parameters retrieved from the nanoscale model (unit cell) as shown in figure 5.15(a) and (b) were placed in the homogenized macro-model shown in 5.20(a) for evaluating the optical performance of the composites, in terms of reflectance over the frequency range of the visible light. The width of TiN phase is* 20nm *and the width of the unit cell is* 26nm*, determined according to volume fraction of phases. The maximum mesh element size allowed here in the electromagnetic simulations is* $\lambda/15$*.To study the behaviour of reflectance of the dielectric composite numerically*, we tried to make the numerical model identical to the experimental one. For this purpose, the composite was divided into layers, layer 1 and layer 2. The n, k obtained from the unit cell prepared with AlN matrix with a certain *vf* of Al_2O_3 inside, were placed in layer 1, along with the thickness determined by XPS analysis 5.1.2of the layer 1. The n, k from the unit cell prepared with Al_2O_3 matrix with a certain *vf* of AlNand TiN inside, were placed in layer 2, along with the thickness determined by XPS analysis 5.1.2 of layer 2 . **Note that the process explained above for the construction of the macro model corresponding to the experimentally prepared composite was done separately for composite I and composite II, according to the separate calculations done for composite I and II in the XPS section 5.1.2**. Figure 5.20(b) shows the two

curves with reflectance of the numerical models for composite I and II that were refined according to the outcomes of the composites prepared experimentally.

To experimentally validate the numerical procedure for having achieved reflectance, UV-Visible Spectrophotometer was used for the measurement of the reflectance experimentally. Before measuring the reflectance of the final SSCs that are developed in this work, it is important to show and understand the reflectance of the two composites I and II. This would provide a clear understanding of the optical performance of an important component of the SSCs and would give an insight for later, on the improvement of the composites after having added the metallic structure omega.

The optical reflectance in the visible and IR range was measured experimentally using the Perkin Elmer Lambda 750 Spectrophotometer. The SEM images in the figure 5.5(a), (b) for composite dielectric I shows partial coverage of the Si substrate with agglomerates ranging from about 50 *to* 360nm*, while the image corresponding to that of the composite dielectric II also shows partial coverage, but with slightly more surface coverage, and agglomerates ranging from about* 80 *to* 550nm*. In the numerical simulation, shown in figure 5.20(a), we modelled two cases by considering the XPS results; where the bottom layer is made of composite (*AlN − TiN − Al_2O_3*) of thickness* 278nm *and* 232nm *the top layer is made of composite* AlN − Al_2O_3 *with* 22nm *and* 68nm *thickness, respectively for composite I and II.* Figure 5.21 shows the comparison between the measured (experimentally) and the computed (numerically) reflectance at normal incidence of both composites. The different black curves in the figure represents different positions in composite I whereas, the different red curves in the figure represents different positions in composite II. The three black curves are close to each other, with a difference of around 10% reflectance in the entire spectral range. This occurs due to the difference in TiN distribution in the composite I, which was quite challenging to control manually. Nevertheless, it also confirms the good reproducibility in composite I. The black and the red curves show a considerable difference in magnitude in the IR region. This happens because first, composite II has more absorbing material than composite I and much bigger agglomerates, and second, the presence of less AlN(higher n) in composite I than in II. The dotted green curve corresponds to numerical macromodel for composite II while the bold green corresponds to numerical macromodel for composite I. The black reflectance curves are close to the numerical model curve for composite I because TiN distribution achieved in case of composite I was better in terms of homogeneity and the size of the TiN agglomerates. Whereas, the red reflectance curves are seen to have a large difference compared with the numerical model curve for composite II. This happens because the model considers a uniform and a homogeneous distribution of TiN NPs throughout the composite, which is not achieved experimentally, *and the model surfaces are uniform, while the composites have very rough surfaces. The important thing to note here is that all curves show a peculiar filter behaviour at* 1μm*, as predicted.*

In the entire work carried out in the thesis for both numerical and experi-

mental study, transmittance is considered 0 **i.e;** $A = 1 - R$.

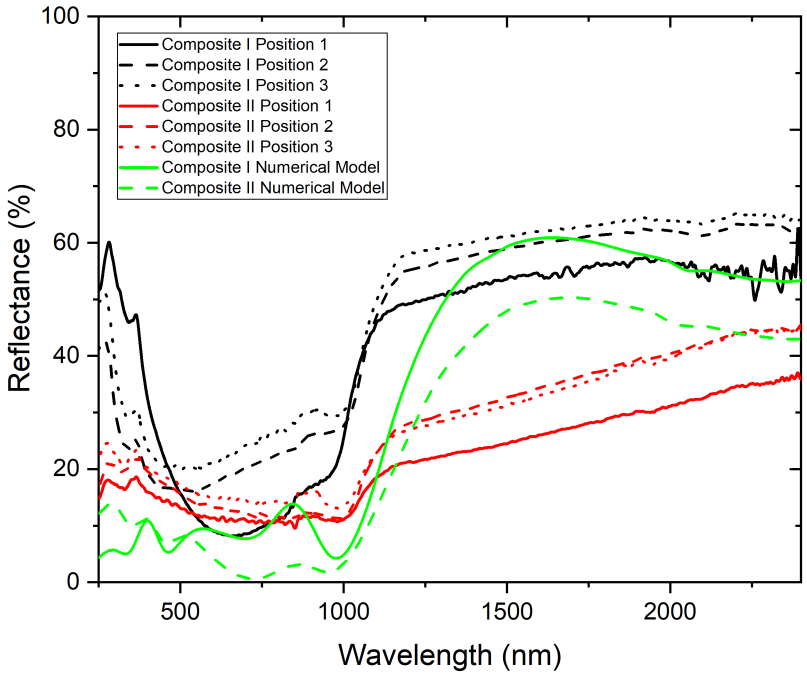

Figure 5.21: Comparison of reflectance (experimental) of composite I and II each at three different positions along with the numerical macro-models corresponding composite I and II.

5.2.5 Comparison of reflectance of the metamaterial (final SSCs) prepared experimentally and numerical macro model corresponding to the metamaterial.

For computing the reflectance of the entire SSCs, an omega structure was added on top of the numerically prepared composite model. For this purpose two layer composite was modelled by placing it on top of a Si wafer, with penetration of the wave only upto one λ. The thickness for layer 1 and 2 is taken from the XPS calculations 5.1.2 for both composite I and II. The omega structure with calculated dimensions (as shown in figure 4.4) is laid on top of the composite. The maximum element size for meshing the omega structure and the composite was taken as $\lambda/5$. The figure 5.22(a) shows a numerically constructed model for a metamaterial. Figure 5.22(b) shows the computed reflectance for metamaterial I and II corresponding to the model shown in figure 5.22(a).

After the composite II was converted into the metamaterial II experimentally, the reflectance of the metamaterial II was measured with UV-Visible spectrometer. It is seen clearly in the graph in the figure 5.23 that after the conversion of composite II to metamaterial II, the trend of reflectance throughout the spectrum is still the same. It was hypothesized that the addition of omega structure on the composite would enhance the filter at 1μm leading to the curve close to an ideal selective reflectance as depicted by

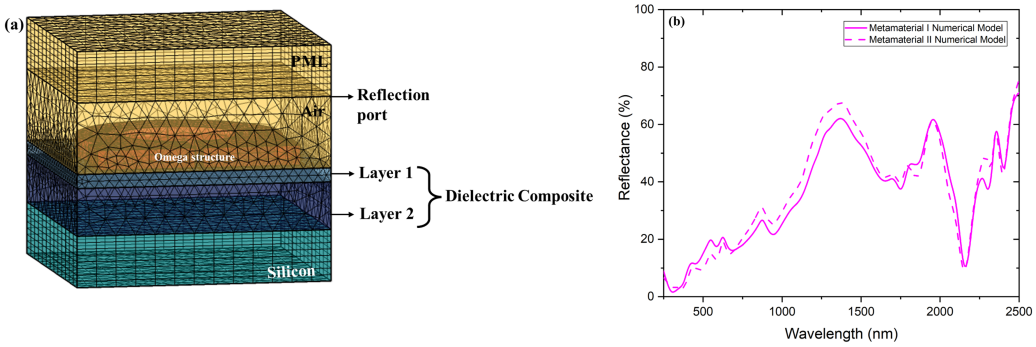

Figure 5.22: (a) Figure showing the constructed metamaterial (by addition of mega structure on top of the composite). (b) Reflectance obtained from the numerical macromodel I and II, corresponding to the experimentally synthesized model.

the blue curve in the figure 2.4.

Figure 5.23 shows a comparison of reflectance of composite II at three different positions along with reflectance of metamaterial II. The reflectance of the metamaterial II is same as the reflectance of composite II. It is explained in the section 5.1.1 of the this chapter, that only $8,000,000$ omegas were good out of total $16,000,000$ omegas, which makes only 50% good omegas in the patterned $5\text{mm} * 5\text{mm}$ area. Due to such low number of good omegas in the matrix, the resonance created is not sufficient to enhance the filter present at 1μm. The large number of bad omegas present had no gap between their arms that led to the LCR circuit with the absence of capacitance. Also, from the graph in the figure 5.21, it is understood well that composite II (red curves) under-performed compared to composite I (black curves). And hence addition of omega patterns on top of composite II did not work well. **Note that the experimental study of reflectance was only done for metamaterial II.**

The graph in the figure 5.24 below shows a comparison of reflectance between numerically and experimentally developed metamaterials, along with numerically obtained reflectance of the composites. The purple bold curve in the graph below shows the reflectance for metamaterial I obtained numerically, and the purple dashed curve in the graph below shows the reflectance for metamaterial II obtained numerically. The blue curve depicts the reflectance of the metamaterial II obtained experimentally. According to the hypothesis made, both the purple curves should have reflectance close to the reflectance of the two green curves in the visible region of the spectrum, a sharp filter at 1μm, and reflectance more than the reflectance of the green curves in the IR region of the spectrum. This way we could achieve a trend close to that of an ideal selective reflectance. It was proved numerically in chapter 4 in figure 4.5(b) that the addition of omega to the composite does improve its filter and thus reflectance in the IR spectrum, but the addition of omega to the composites achieved experimentally as ineffective. It is clear from the graph 5.24 that the metamaterial II (blue curve, experimentally obtained) under-performed due to the reasons mentioned above. But the reflectance from the purple curves (numerically

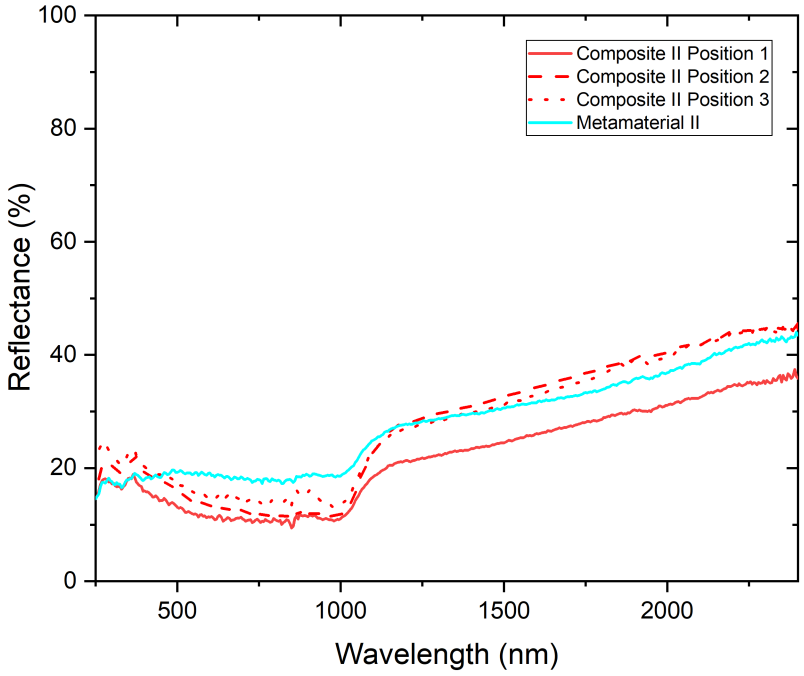

Figure 5.23: Comparison of reflectance of composite II at three different positions along with reflectance of metamaterial II.

obtained) is also underachieved, though their function was to enhance the local field via plasmonic resonance which would have direct effect on the reflectance. The reflectance in the visible region rose considerably high, suppressing the filter at 1μm, and then in the IR spectrum there are two valleys, one near 1750nm and the other deeper one at around 2150nm, reducing its performance.

According to the investigation done the performance for the metamaterial I numerical model and metamaterial II numerical model is such because the dimensions of the omega used as a resonator were only optimized for the composite dielectric with 20% $TiN - AlN$ matrix. The composite used for this study had a presence of 47% Al_2O_3 and 9.5% TiN in composite I, and 61% Al_2O_3 and 16.5% TiN in composite II, which is very different than the composition of the optimized composite. When we considered an ideal scenario of 20%$TiN - AlN$ composite and metamaterial in the figure 4.5(b), it was observed that the addition of omega did enhance the filter of the 20%$TiN - AlN$composite.

5.2.6 Thermal Stability test of the composites

An investigation on the thermal stability of the prepared composites I and II was carried out. The thermal stability test of the two types of designed composite was investigated by exposing the composite I and II in the furnace for constant 12hours with a symmetric test.

Visual check can be very important to inspect sample degradation. It is possible to

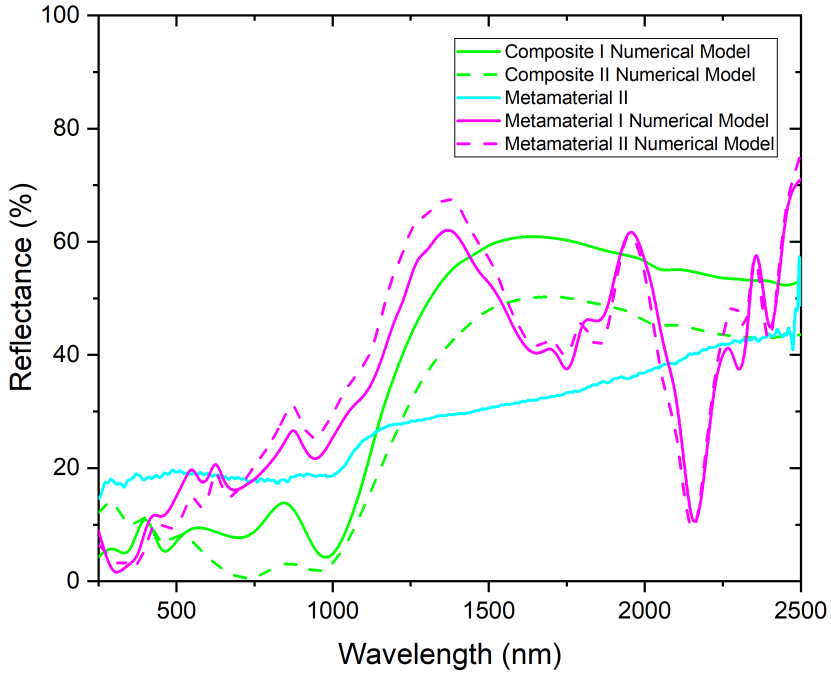

Figure 5.24: Comparison of reflectance between numerically and experimentally developed metamaterials I and II, along with numerically obtained reflectance of the composites I and II.

identify surface cracks, delamination of coatings and extreme color change of the coatings via visual inspection. Thus, after each heating step, it became useful to validate the integrity of the sample. Samples of composite I and II after annealing at 800°C and 1000°C for 12hours constantly were visually same like as-prepared samples. The surface cracks were not visible, delamination of the coating did not occur and the change of color did not take place.

After the samples had passed the visual check, the stability of the films was further tested through their performance by reflectance through UV-Visible Spectrophotometer. For this purpose *Perkin Elmer Lambda 750 Spectrophotometer was used.* Figure 5.25(i) shows the comparison of reflectance of composite I (as prepared), annealed at 800°C for 12hours, and annealed at 1000°C for 12hours. Figure 5.25 (ii) shows the comparison of reflectance of composite II (as prepared), annealed at 800°C for 12hours, and annealed at 1000°C for 12hours.

In both the graphs of figure 5.25, we see that the samples annealed at 800°C and 1000°C lost about 10 of reflectance in the visible region of the spectrum, whereas the same samples gain about 10 reflectance in IR spectrum, with respect to the ideal curve for solar absorber. It is hard to comment here, if the samples for composite I and II annealed at 800°C and at 1000°C show better or poor performance, because considering figure 5.21 we see that there is change in reflectance at two different positions for the

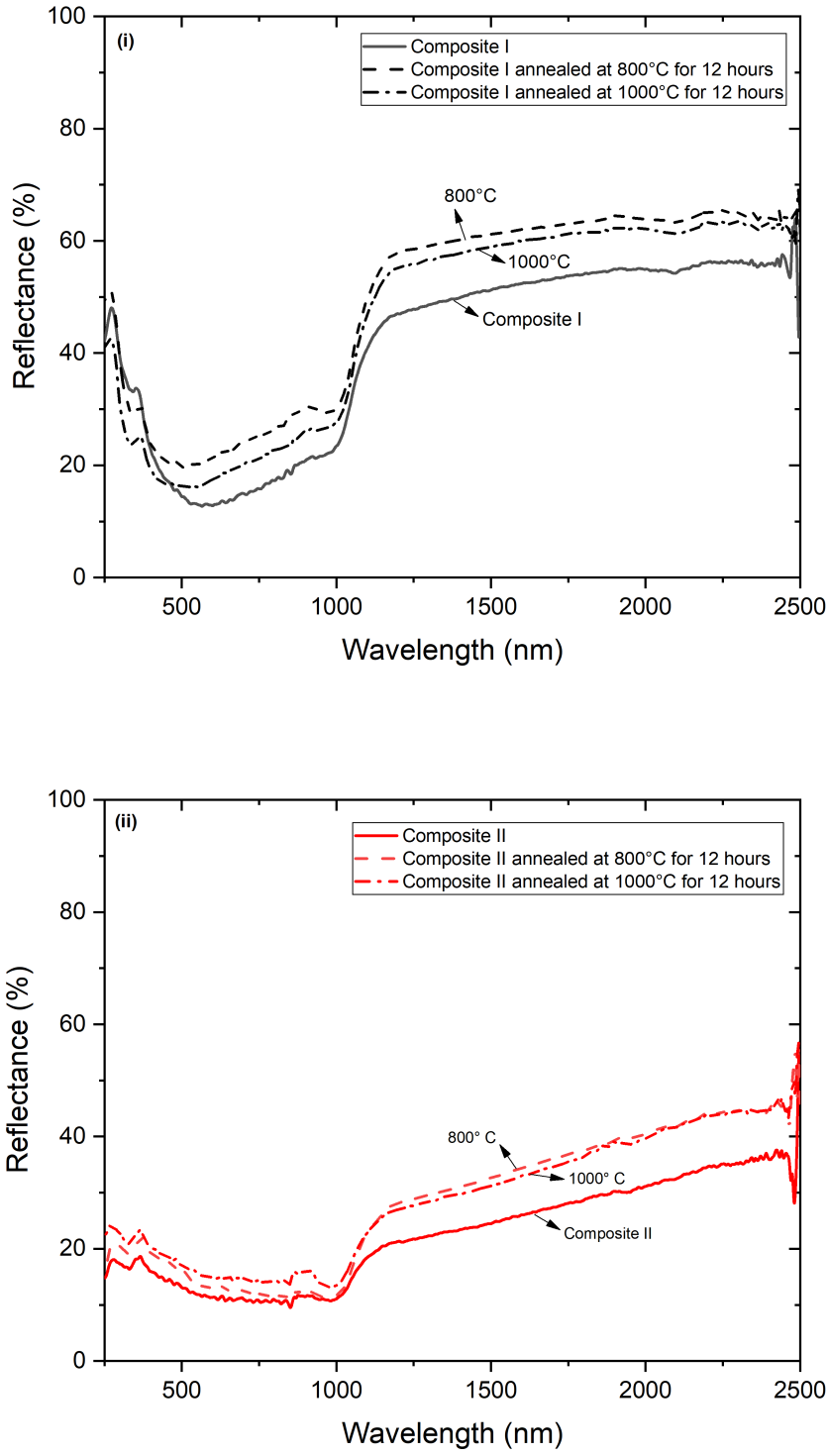

Figure 5.25: Thermal stability test done at 800°C and 1000°C in vacuum for 12hours for composite I and composite II.

same composite. This difference in reflectance at different positions in composite I and II is due to the inhomogeneous distribution of TiN NPs in the composite. This is explained in the subsection 5.2.4 above. Talking about the thermal stability, it is worth noting that even after annealing composite I and II at 800°C and 1000°C, both the composites I and II are stable. The reflectance for composite I and II did not change significantly after heat treatment up to 1000°C.

The high thermal stability of the of both the composites comprising of multilayer cermet is attributed to several factors. The interdiffusion between AlN/TiN and TiN/AlN is expected to be very low up to 1000°C because of high melting points of AlN and TiN, high activation energies and their stable microstructures.

Chapter 6

Conclusion and Outlook

The present thesis addresses an unconventional design of new solar selective coatings (SSCs) for application at elevated temperature aiming to enhance the performance of the concentrating solar power (CSP) plants. In particular three new materials were proved as promising materials for SSCs. A systemized methodology to design, synthesize and characterize was adopted, and thus proposed in this work.

The first approach is based on designing the SSCs which included the designing of different components present in the SSCs. The different components in the SSCs includes the dielectric matrix that would contain nanoparticle inclusions with a specific diameter, and were distributed in the matrix in a controlled volume fraction. For better performance of the composite, the distribution of TiN NPs and deposition of AlN thin film was done several times to make it a multilayer composite. An array of omega shaped resonator is integrated on top of the multilayer composite that comprises of the nanoparticles embedded in the dielectric matrix, making the composite a metamaterial. These nanocomposite materials were selected as their blend of optical and thermo-mechanical properties. These materials proved to have adjustable solar selective properties along with high-temperature resistance that makes them captivating candidates for SSCs. Based on the literature survey the best selected materials for nanoparticles inclusions is TiN, dielectric matrix is AlN and resonator is Pt. Optical simulation with wave optics module of COMSOL Multiphysics resulted in an appropriate approach to expedite the selection of materials for each component of the SSCs. With the purpose of achieving a sharp filter, the *vf* of the TiN nanoparticles in the nanocomposite and the diameter (D) of the (TiN) nanoparticles were optimized for a stack of composed nanocomposite with an average thickness of 300nm with AlN(20nm thickness of each layer)/ TiN(20nm diameter)/ *vf* of TiNin the composite (20%), and for the metamaterial with specific dimensions of omega. These parameters were retrieved by simulating the designs of the nanoscale model and the macro model. The dimensions of omega were retrieved by a method called Proper Orthogonal Decomposition (POD) and Machine learning (ML) algorithm based on neural network (NN). It was proved numerically that the addition of omega structure to the composite enhances the filter characteristics and improves the reflectance in the IR spectrum. Throughout

the work presented in the thesis, the composite and the metamaterial were optimized separately for a clear difference and understanding in their optical properties. All through the thesis, optimization of optical performance was done for two types of composites, one prepared with commercial prepared TiN powders, and the other with commercially prepared TiN dispersions. The synthesis of the nanocomposites was done in two phases combining a wet-chemical and thin film deposition method. The entire synthesis process for the two composites was the same, except the different types of TiN (TiN powder and TiN dispersions) used in the composite. The composite prepared with dry TiN powders is referred to as composite I and the composite prepared with TiN dispersions is referred as composite II. Later (Pt) omega structures were added on top of the composite via e-beam lithography (This part of the experimental section was done in Institute Lafayette, Metz, France). Note that the addition of omega structures was only possible on composite II, as a consequence of time constraint. Being a challenging technology, dose optimization for such complicated rough structures with e-beam lithography took more than expected time. Thus, the thesis presents only the experimental synthesis of metamaterial II.

The two experimentally prepared composites was investigated using characterization techniques including the morphological, compositional analysis, and optical characterizations for composites and metamaterial separately. At first the morphological characterization was done by FIB-SEM demonstrating the nanostructure of the two composites, including the arrangement of nanoparticles in the matrix and their thicknesses. To begin with the investigation, the very first layer of deposition of TiN NPs was analysed with SEM and the software ImageJ, and despite manual control, we were able to achieve nearly 20of the TiN distribution. The second, third and fourth layer of TiN distribution, that actually makes the third, fifth and seventh layer in the composite did not include nearly 20 TiNdistribution but less. It was observed that the two composites had very rough structure with thickness of composite I (average thickness $\simeq$250nm) less than the thickness of composite II (average thickness $\simeq$350nm). For the metamaterial II, it was observed that only half the omegas had an opening present between the two arms. For the rest of the omegas, the arms were connected to each other forming closed omegas. For the composition analysis, XPS is utilized. The XPS analysis is done only for composite I and II. It was observed that other than TiN and AlN, $Al_2O_3$was also present in the two composites. Thus, for the simplification and better understanding of the two composites, the composites were divided into two layers, The upper layer 1 and the lower layer 2. In composite I, layer 1 had 64.5%AlN and 35.5%Al_2O_3 with thickness 22nm, and layer 2 had 9.5%TiN, 46.2%AlNand 47.4%$Al_2O_3$with thickness 278nm. In composite II, layer 1 had 64.5%AlN and 35.5%$Al_2O_3$with thickness 68nm, and layer 2 had 16.5%TiN, 22.4%AlNand 61%Al_2O_3 with thickness 232nm. Later an impedance spectroscopy measurement was made to test the conducting behaviour of composite I and II.

After dividing the two composites into two layers, the same was done for a numerical model, in order to achieve a numerical model imitating the experimentally prepared

model. Doing so gave us a clear and reliable opportunity for comparing the optical constants n and k of numerically constructed composite models with the experimentally prepared composites. The optical constants n and k were retrieved via S-parameters numerically and via spectroscopic ellipsometer experimentally. The optical constants n and k for the numerically constructed composites were in close proximity with the experimentally prepared composites. This gave us a clear indication for similar optical performance (reflectance) for the numerically and experimentally prepared composites. For the comparison of reflectance, different positions were tested for both composites I and II via UV-Vis spectrophotometer. The curves were in close comparison to each other for composite I with a presence of a clear filter near 1μm. This highlights that composite I samples were reproducible in terms of synthesis and reflectance curves. Comparing the optical performance of experimentally synthesized composite I and II, composite I was proved superior. It is also worth noting that we were able to achieve similar performance of composite I numerically and experimentally, despite such challenging tasks of controlled distribution of 20%TiN NPs distribution and such complicated structure of the composite.

A numerical model was prepared mimicking the experimentally prepared metamaterial. The reflectance for both experimentally prepared and numerically constructed metamaterial model was compared. The reflectance achieved for numerically prepared metamaterial I and II was not as hypothesized. The only reason we could envisage was that the omega structure with the dimensions that we currently used was not optimized for these composites that we achieved experimentally. The reflectance for metamaterial II was the same as the reflectance for composite II. The addition of added Pt omega structures refrained from enhancing the filter of the composite II due to the presence of huge number of bad omegas in the metamaterial.

The thermal stability test for composite I and II was made at 800°C and 1000°C. The composites were subjected to high temperature in the furnace for 12hours in Ar air flow. Even after 12hours of continuous heating, composite I and II neither show any change in their appearance nor in their optical performance. They were proved stable at 1000°C.

6.1 Future Scope

Here I present a list of recommendations for future actions for further optimization of SSCs described in this thesis:

- In order to improve the quality of SSCs (after the addition of omega structures) , further experimental studies should be carried out to achieve composite with 20 vf of TiN in AlN.
- To reduce the amount of Al_2O_3 in the composite, a trial should be made to synthesize the composite in one phase i.e., preparation of TiN NPs in the ALD reactor followed by AlN deposition.

- A numerical optimization should be done for the integration of omega structures on top of composites that were achieved experimentally in this work.
- More experimental work is needed to be carried out for the optimization of quality of omega structures by e-beam lithography, where the correct dose is to be optimized according to the surface properties on which the omega is to be patterned.
- After improving the quality of omega a similar metamaterial I (integration of omega structures on top of the composite I) should be prepared experimentally for the measurement of reflectance in order to enhance the filter characteristic of the SSCs.
- Thermal stability test for both metamaterials I and II should be carried out at to check their effectiveness for SSCs.

Bibliography

[1] Albarbar and Arar. Performance Assessment and Improvement of Central Receivers Used for Solar Thermal Plants. *Energies*, 12(16):3079, aug 2019.

[2] Swapnil S. Salvi, Vishal Bhalla, Robert A. Taylor, Vikrant Khullar, Todd P. Otanicar, Patrick E. Phelan, and Himanshu Tyagi. Technological Advances to Maximize Solar Collector Energy Output: A Review. *Journal of Electronic Packaging*, 140(4), oct 2018.

[3] Shuxi Zhao. *Spectrally Selective SolarAbsorbing Coatings Prepared by dcMagnetron SputteringÃ*^{2}. $PhDthesis, UppsalaUniversitet$, 2007.

[4] Alex Gansen. Multiscale Modelling of Anisotropic Composite Media for EMC applications. *PhD thesis, Luxembourg Institute of Science and Technology, 2017.*

[5] J. W. Tester. EnergyâProduction, consumption and consequences: JL Helm,(Editor) National Academy Press Washington, DC. 1990. viii+ 296 pp. *Elsevier, 1992.*

[6] E. G. Peake. Energy policies, politics and prices: US energy: overview of the trends, statistics, supply and consumption. *Nova Science Publishers, Inc., 2010.*

[7] U. S. Energy Information Administration. International Energy Outlook. With Projections to 2040. US Energy Information Administration*, 2011.*

[8] B. P. Energy Outlook. BP Energy Outlook 2035. British Petroleum. http://www.bp.com/content/dam/bp/pdf/Energy-economics/Energy-Outlook/$Energy_{O}utlook_{2}035_{b}ooklet, January2014$.

[9] U. S. Energy Information Administration. Levelized Cost and Levelized Avoided Cost of New Generation Resources in the Annual Energy Outlook 2014, Annual Energy Outlook 2014. http://www.eia.gov/forecasts/aeo/$electricity_{g}eneration.cfm.Technicalreport, U.S.EnergyInforn$

[10] H. Z. Tabor. Surfaces for Collectors of Solar Radiation. United States patent Office, April 1964.

[11] Jun Li. Scaling up concentrating solar thermal technology in China. Renewable and Sustainable Energy Reviews*, 13(8):2051–2060, 2009.*

[12] Ruchi Shukla, K. Sumathy, Phillip Erickson, and Jiawei Gong. Recent advances in the solar water heating systems: A review. Renewable and Sustainable Energy Reviews*, 19:173–190, 2013.*

[13] Tomislav M. Pavlović, Ivana S. Radonji, Dragana D. Milosavljevi, and Lana S. Panti. A review of concentrating solar power plants in the world and their potential use in Serbia. Renewable and Sustainable Energy Reviews*, 16(6):3891–3902, 2012.*

[14] Pascal De Laquil, David Kearney, Michael Geyer, and Richard Diver. Solar-thermal electric technology*, volume 213. Island Press Washington, DC, 1993.*

[15]

[16] Pekka Alitalo and Sergei Tretyakov. Electromagnetic cloaking with metamaterials. Materials today*, 12(3):22–29, 2009.*

[17] K. Guven, E. Saenz, R. Gonzalo, Ekmel Ozbay, and S. Tretyakov. Electromagnetic cloaking with canonical spiral inclusions. New Journal of Physics*, 10(11):115037, 2008.*

[18] Michael Selvanayagam and George V. Eleftheriades. Experimental demonstration of active electromagnetic cloaking. Physical review X*, 3(4):041011, 2013.*

[19] S. A. Tretyakov and A. A. Sochava. Proposed composite material for nonreflecting shields and antenna radomes. Electronics Letters*, 29(12):1048–1049, 1993.*

[20] S. A. Tretyakov and A. A. Sochava. Novel uniaxial bianisotropic materials: Reflection and transmission in planar structures. Progress In Electromagnetics Research*, 9:157–179, 1994.*

[21] Sergey L. Prosvirnin and Nikolay I. Zheludev. Analysis of polarization transformations by a planar chiral array of complex-shaped particles. Journal of Optics A: Pure and Applied Optics*, 11(7):074002, 2009.*

[22] V. S. Butylkin and G. A. Kraftmakher. Passbands of bianisotropic and waveguide bianisotropic metamaterials based on planar double split rings. Journal of Communications Technology and Electronics*, 53(1):1–14, 2008.*

[23] V. S. Butylkin and G. A. Kraftmakher. Nonreciprocal effects in propagation of microwaves along a waveguide structure formed from a ferrite plate and a lattice of resonant elements. Journal of Communications Technology and Electronics*, 54(7):775–782, 2009.*

[24] R. Yang, Y. J. Xie, X. F. Li, and J. Jiang. Slow wave propagation in nonradiative dielectric waveguides with bianisotropic split ring resonator metamaterials. Infrared physics & technology*, 51(6):555–558, 2008.*

[25] Yang Hao and Raj Mittra. FDTD modeling of metamaterials: Theory and applications. *Artech house, 2008.*

[26] On Group-Velocity. *London Mathematical Society, 1904.*

[27] S. Anantha Ramakrishna and Tomasz M. Grzegorczyk. Physics and applications of negative refractive index materials. *CRC press, 2008.*

[28] John B. Pendry, Anthony J. Holden, David J. Robbins, and W. J. Stewart. Magnetism from conductors and enhanced nonlinear phenomena. IEEE transactions on microwave theory and techniques*, 47(11):2075–2084, 1999.*

[29] David R. Smith, Willie J. Padilla, D. C. Vier, Syrus C. Nemat-Nasser, and Seldon Schultz. Composite medium with simultaneously negative permeability and permittivity. Physical review letters*, 84(18):4184, 2000.*

[30] Umran S. Inan and Robert A. Marshall. Numerical electromagnetics: the FDTD method. *Cambridge University Press, 2011.*

[31] Constantine A. Balanis. Wave propagation and polarization. Advanced Engineering Electromagnetics*, pages 136–137, 1989.*

[32] E. Hecht. Optics. 4th edn Addison-Wesley. Reading, Mass*, 2002.*

[33] Sune Svanberg. Atomic and molecular spectroscopy: basic aspects and practical applications*, volume 6. Springer Science & Business Media, 2012.*

[34] Edgar Bright Wilson, John Courtney Decius, and Paul C. Cross. Molecular vibrations: the theory of infrared and Raman vibrational spectra. *Courier Corporation, 1980.*

[35] A. Wokaun. B. Schrader: Infrared and Raman Spectroscopy - Methods and Applications. VCH, Weinheim, 1995, DM 298,-, ISBN 3-527-26446-9. Berichte der Bunsengesellschaft fÃŒr physikalische Chemie*, 100(7):1268–1268, jul 1996.*

[36] M. Planck. The theory of heat radiation, English transition of Theorie der WÃ€rmestrahlung, 2nd eition (1913). *Dover Publications, New York, 1959.*

[37] Frank J. Blatt. Roots of the Quantum Theory in Modern Physics*, page 71. McGraw-Hill, Inc. New York, 1991.*

[38] J. C. McVeigh. Sun power: An introduction to the applications of solar energy*, pages 11–21. Pergamon Press, Oxford, 1977.*

[39] ASTM. ASTM G173: Standard Tables for Reference Solar Spectral Irradiance at Air Mass 1.5:Direct Normal and Hemispherical for a 37 Degree Tilted Surface. Technical report, US, 2008.

[40] William A. Beckman John A. Duffie. Solar Engineering of Thermal Processes*, chapter Flat -plate Collector, pages 236–321. John Wiley Sons, Inc., New jersey, 2013.*

[41] B. K. Gupta O. P. Agnihotri. Solar Selective Surfaces*, page 88. Wiley-Interscience publication, New York, 1981.*

[42] E. Wackelgard and G. Hultmark. Industrially sputtered solar absorber surface. SOLAR ENERGY MATERIALS AND SOLAR CELLS*, 54(1-4):165–170, 1998. Addresses: Wackelgard E, Univ Uppsala, Dept Mat Sci, Box 534, S-75121 Uppsala, Sweden. Univ Uppsala, Dept Mat Sci, S-75121 Uppsala, Sweden. Teknotern Energi, S-43634 Askim, Sweden.*

[43] European Standard, EN 673, Thermal insulation of glazing calculation rules for determining the steady "U" value (thermal transmittance) of glazing, 1998.

[44] Zhonghua Chen. Carbon Nanotube Spectrally Selective Solar Thermal Absorbers. 2016.

[45] Irene Heras Pérez. Multilayer solar selective coatings for high temperature solar applications: From concept to design. 2016.

[46] Ke Zhang, Lei Hao, Miao Du, Jing Mi, Ji-Ning Wang, and Jian-ping Meng. A review on thermal stability and high temperature induced ageing mechanisms of solar absorber coatings. Renewable and Sustainable Energy Reviews*, 67:1282–1299, 2017.*

[47] Bahaa E. A. Saleh and Malvin Carl Teich. Fundamentals of photonics*. John Wiley & sons, 2019.*

[48] Wendell T. Hill III and Chi H. Lee. Light-Matter interaction: Atoms and molecules in external fields and nonlinear optics*, volume 2. John Wiley & Sons, 2006.*

[49] Bernardo Garcıa Olmedo. Fundamentos de electromagnetismo*. 2006.*

[50] W. J. Plieth and K. Naegele. Kramers-Kronig analysis for the determination of the optical constants of thin surface films: I. Theory. Surface Science*, 50(1):53–63, 1975.*

[51] M. Fox. Classical propagation. Optical Properties of Solids, Oxford University Press Inc., New York*, pages 25–48, 2001.*

[52] Lixing Dou and Abdel R. Sebak. 3D FDTD method for arbitrary anisotropic materials. Microwave and Optical Technology Letters*, 48(10):2083–2090, 2006.*

[53] Adrian Doicu. Null-field method to electromagnetic scattering from uniaxial anisotropic particles. Optics communications*, 218(1-3):11–17, 2003.*

[54] *Vladimir Schmidt and Thomas Wriedt. T-matrix method for biaxial anisotropic particles.* Journal of Quantitative Spectroscopy and Radiative Transfer, *110(14-16):1392–1397, 2009.*

[55] *Laszlo Solymar and Ekaterina Shamonina.* Waves in metamaterials. *Oxford University Press, 2009.*

[56] *Viktor G. Veselago.* The electrodynamics of substances with simultaneously negative values of epsilon and mu, *volume 10(4):509-514. 1968.*

[57] *Erik Lier, Douglas H. Werner, Clinton P. Scarborough, Qi Wu, and Jeremy A. Bossard. An octave-bandwidth negligible-loss radiofrequency metamaterial.* Nature materials, *10(3):216–222, 2011.*

[58] *Th Koschny, M. Kafesaki, E. N. Economou, and C. M. Soukoulis. Effective medium theory of left-handed materials.* Physical review letters, *93(10):107402, 2004.*

[59] *Dagang Wu, Rui Qiang, J. Chen, Ce Liu, Marina Koledintseva, J. Drewniak, and Bruce Archambeault. Numerical Modeling of Periodic Composite Media for Electromagnetic Shielding Application. In* 2007 IEEE International Symposium on Electromagnetic Compatibility. *IEEE, jul 2007.*

[60] *G. Katumba and A. Forbes. Carbon-in-silica composite selective solar absorbers: a determination of composition and dielectric properties. In* Optical Modeling and Measurements for Solar Energy Systems III, *volume 7410, page 74100G. International Society for Optics and Photonics, 2009.*

[61] *J. C. Maxwell Garnett. Colours in metal glasses, in metallic films, and in metallic solutions. II.* Philosophical Transactions of the Royal Society of London Series A, *205:237–288, 1906.*

[62] *D. A. G. Bruggeman. Berechnung verschiedener physikalischer Konstanten von heterogenen Substanzen. I. DielektrizitÃ€tskonstanten und LeitfÃ€higkeiten der MischkÃ¶rper aus isotropen Substanzen.* Annalen der Physik, *416(7):636–664, 1935.*

[63] *Yuyi Yang.* The study of nanostructured solar selective coatings. *PhD thesis, University of York, 2012.*

[64] *H. Angus Macleod and H. Angus Macleod.* Thin-film optical filters. *CRC press, 2010.*

[65] *Hemant Kumar Raut, V. Anand Ganesh, A. Sreekumaran Nair, and Seeram Ramakrishna. Anti-reflective coatings: A critical, in-depth review.* Energy & Environmental Science, *4(10):3779–3804, 2011.*

[66] *Han Haitjema. Spectrally selective tinoxide and indiumoxide coatings. 1989.*

[67] Nikhar Khanna, Mohamed El Hachemi, Ruben Sevilla, Oubay Hassan, Kenneth Morgan, Emanuele Barborini, and Salim Belouettar. Multi-physical modelling, design optimization and manufacturing of a composite dielectric solar absorber. Composites Part C: Open Access*, 8:100282, aug 2022.*

[68] B. O. Seraphin. Topics in Applied Physics. Vol. 31. Solar Energy Conversion. Solid State Physics Aspects. Springer-Verlag, xiii+ 336, 24 x 16 cm, illustrated(DM 98. 00*, 1979.*

[69] E. Randich and D. D. Allred. Chemically vapor-deposited ZrB2 as a selective solar absorber. Thin Solid Films*, 83(4):393–398, 1981.*

[70] John A. Thornton and James L. Lamb. Thermal stability studies of sputter-deposited multilayer selective absorber coatings. Thin Solid Films*, 96(2):175–183, 1982.*

[71] R. N. Schmidt and K. C. Park. High-temperature space-stable selective solar absorber coatings. Applied Optics*, 4(8):917–925, 1965.*

[72] G. A. Niklasson and C. G. Granqvist. Selectively solar-absorbing surface coatings: optical properties and degradation. pages 70–105, 1991.

[73] Shuxi Zhao. Spectrally selective solar absorbing coatings prepared by dc magnetron sputtering*. PhD thesis, Acta Universitatis Upsaliensis, 2007.*

[74] Tuquabo Tesfamichael. Characterization of selective solar absorbers : experimental and theoretical modeling*. Acta Universitatis Upsaliensis, Uppsala, 2000.*

[75] G. L. Harding and M. R. Lake. Sputter etched metal solar selective absorbing surfaces for high temperature thermal collectors. Solar Energy Materials*, 5(4):445–464, 1981.*

[76] Richard B. Stephens and George D. Cody. Optical reflectance and transmission of a textured surface. Thin Solid Films*, 45(1):19–29, 1977.*

[77] J. J. Cuomo, J. F. Ziegler, and J. M. Woodall. A new concept for solar energy thermal conversion. Applied Physics Letters*, 26(10):557–559, 1975.*

[78] Cheryl E. Kennedy. Review of mid-to high-temperature solar selective absorber materials. Technical report, National Renewable Energy Lab., Golden, CO.(US), 2002.

[79] Liang Wu, Junhua Gao, Zhimin Liu, Lingyan Liang, Fei Xia, and Hongtao Cao. Thermal aging characteristics of CrNxOy solar selective absorber coating for flat plate solar thermal collector applications. Solar energy materials and solar cells*, 114:186–191, 2013.*

[80] Feng Cao, Daniel Kraemer, Tianyi Sun, Yucheng Lan, Gang Chen, and Zhifeng Ren. Enhanced thermal stability of W-Ni-Al2O3 cermet-based spectrally selective solar absorbers with tungsten infrared reflectors. Advanced Energy Materials*, 5(2):1401042, 2015.*

[81] *M. Kotilainen, M. Honkanen, K. Mizohata, and P. Vuoristo. Influence of temperature-induced copper diffusion on degradation of selective chromium oxynitride solar absorber coatings.* Solar Energy Materials and Solar Cells*, 145:323–332, 2016.*

[82] *Xiaoyu Wang, Junhua Gao, Haibo Hu, Hongliang Zhang, Lingyan Liang, Kashif Javaid, Fei Zhuge, Hongtao Cao, and Le Wang. High-temperature tolerance in WTi-Al2O3 cermet-based solar selective absorbing coatings with low thermal emissivity.* Nano Energy*, 37:232–241, 2017.*

[83] *Glen E. McDonald. Spectral reflectance properties of black chrome for use as a solar selective coating.* Solar Energy*, 17(2):119–122, 1975.*

[84] *I. T. Ritchie, S. K. Sharma, J. Valignat, and J. Spitz. Thermal degradation of chromium black solar selective absorbers.* Solar Energy Materials*, 2(2):167–176, 1979.*

[85] *R. B. Pettit, R. R. Sowell, and I. J. Hall. Black chrome solar selective coatings optimized for high temperature applications.* Solar Energy Materials*, 7(2):153–170, 1982.*

[86] *John C. C. Fan and Steven A. Spura. Selective black absorbers using rf-sputtered Cr2O3/Cr cermet films.* Applied Physics Letters*, 30(10):511–513, 1977.*

[87] *V. Teixeira, E. Sousa, M. F. Costa, C. Nunes, L. Rosa, M. J. Carvalho, M. Collares-Pereira, E. Roman, and J. Gago. Spectrally selective composite coatings of Cr–Cr2O3 and Mo–Al2O3 for solar energy applications.* Thin solid films*, 392(2):320–326, 2001.*

[88] *C. Nunes, V. Teixeira, M. L. Prates, N. P. Barradas, and A. D. Sequeira. Graded selective coatings based on chromium and titanium oxynitride.* Thin Solid Films*, 442(1-2):173–178, 2003.*

[89] *Y. Yin and R. E. Collins. Optimization and analysis of solar selective surfaces with continuous and multilayer profiles.* Journal of applied physics*, 77(12):6485–6491, 1995.*

[90] *S. N. Kumar, L. K. Malhotra, and K. L. Chopra. Nickel pigmented anodized aluminium as solar selective absorbers.* Solar Energy Materials*, 7(4):439–452, 1983.*

[91] *Harold G. Craighead and R. A. Buhrman. Optical properties of selectively absorbing Ni/Al2O3 composite films.* Applied Physics Letters*, 31(7):423–425, 1977.*

[92] *T. Stephen Sathiaraj, R. Thangaraj, H. Al Sharbaty, M. Bhatnagar, and O. P. Agnihotri. Ni-Al2O3 selective cermet coatings for photothermal conversion up to 500 C.* Thin Solid Films*, 190(2):241–254, 1990.*

[93] *Zhaofeng Li, Koray Aydin, and Ekmel Ozbay. Retrieval of effective parameters for bianisotropic metamaterials with omega shaped metallic inclusions.* Photonics and Nanostructures-Fundamentals and Applications*, 10(3):329–336, 2012.*

[94] *G. A. Niklasson and C. G. Granqvist. Surfaces for selective absorption of solar energy: an annotated bibliography 1955–1981.* Journal of Materials science*, 18(12):3475–3534, 1983.*

[95] *Harish Barshilia, Prashant Kumar, K. S. Rajam, and Arup Biswas. Structure and optical properties of AgâAl2O3 nanocermet solar selective coatings prepared using unbalanced magnetron sputtering.* Solar Energy Materials and Solar Cells*, 95:1707–1715, 07 2011.*

[96] *Du Xinkang, Wang Cong, Wang Tianmin, Zhou Long, Chen Buliang, and Ru Ning.* Microstructure and spectral selectivity of MoâAl2O3 solar selective absorbing coatings after annealing*, volume 2008.*

[97] *A. Antonaia, A. Castaldo, M. L. Addonizio, and S. Esposito. Stability of W-Al2O3 cermet based solar coating for receiver tube operating at high temperature.* Solar Energy Materials and Solar Cells*, 94(10):1604–1611, 2010.*

[98] *H. G. Craighead, R. E. Howard, J. E. Sweeney, and R. A. Buhrman. Gradedâindex PtâAl2O3 composite solar absorbers.* Applied Physics Letters*, 39(1):29–31, 1981.*

[99] *Qi Chu Zhang. Direct current magnetron sputtered WâAlN cermet solar absorber films.* Journal of Vacuum Science & Technology A*, 15(6):2842–2846, 1997.*

[100] *Qi Chu Zhang and Y. G. Shen. High performance WâAlN cermet solar coatings designed by modelling calculations and deposited by DC magnetron sputtering.* Solar Energy Materials and Solar Cells*, 81(1):25–37, 2004.*

[101] *Zhang Qi Chu. Stainless-steelâAlN cermet selective surfaces deposited by direct current magnetron sputtering technology.* Solar Energy Materials and Solar Cells*, 52(1):95–106, 1998.*

[102] *Qi Chu Zhang, K. Zhao, B. C. Zhang, L. F. Wang, Z. L. Shen, D. Q. Lu, D. L. Xie, Z. J. Zhou, and B. F. Li. A cylindrical magnetron sputtering system for depositing metalâaluminium nitride cermet solar coatings onto batches of tubes.* Journal of Vacuum Science & Technology A*, 16(2):628–632, 1998.*

[103] *Masato Nishimura and Takashi Ishiguro. Solar Selective Absorber Coating Composed of Aluminum and Nitrogen with High Performance Induced by Surface Roughness.* Japanese Journal of Applied Physics*, 43(2):757–761, feb 2004.*

[104] *F. Garnich and E. Sailer. CuîžSiO2/Cu-cermet selective absorbers for solar photothermal conversion.* Solar Energy Materials*, 20(1):81–89, 1990.*

[105] *Qi Chu Zhang and David R. Mills. New cermet film structures with much improved selectivity for solar thermal applications.* Applied Physics Letters, *60(5):545–547, 1992.*

[106] *M. Okuyama, K. Furusawa, and Y. Hamakawa. Ni cermet selective absorbers for solar photothermal conversion.* Solar Energy, *22(6):479–482, 1979.*

[107] *Monica Lira-Cantu, Angel Morales, Alex Brustenga, and Pedro GÃ³mez – Romero.Electrochemicaldepositionofblacknickelsolarabsorbercoatingsonstainlesssteel AISI*316 685 – −694, 052005.

[108] *S. Esposito, A. Antonaia, M. L. Addonizio, and S. Aprea. Fabrication and optimisation of highly efficient cermet-based spectrally selective coatings for high operating temperature.* Thin Solid Films, *517(21):6000–6006, 2009.*

[109] *Jian Wang, Baocheng Wei, Qirui Wei, and Dejie Li. Optical property and thermal stability of Mo/MoâSiO2/SiO2 solar-selective coating prepared by magnetron sputtering.* physica status solidi (a), *208(3):664–667, 2011.*

[110] *O. P. Agnihotri, B. K. Gupta, A. K. Agarwal, and V. P. Bhatnagar. Solar selective black molybdenum coatings by chemical conversion.* Thin Solid Films, *109(3):193–200, 1983.*

[111] *Qi Chu Zhang, M. S. Hadavi, K. D. Lee, and Y. G. Shen. ZrâZrO2 cermet solar coatings designed by modelling calculations and deposited by dc magnetron sputtering.* Journal of Physics D: Applied Physics, *2003.*

[112] *Rei-Cheng Juang, Yung-Chin Yeh, Bing-Hung Chang, Wen-Chieh Chen, and Tsair-Wang Chung. Preparation of solar selective absorbing coatings by magnetron sputtering from a single stainless steel target.* Thin Solid Films, *518(19):5501–5504, 2010.*

[113] *Harry A. Atwater and Albert Polman. Plasmonics for improved photovoltaic devices.* Materials for sustainable energy: a collection of peer-reviewed research and review articles from Nature Publishing Group, *pages 1–11, 2011.*

[114] *Feiliang Chen, Shao-Wei Wang, Xingxing Liu, Ruonan Ji, Liming Yu, Xiaoshuang Chen, and Wei Lu. High performance colored selective absorbers for architecturally integrated solar applications.* Journal of Materials Chemistry A, *3(14):7353–7360, 2015.*

[115] *Lin Zhou, Yingling Tan, Jingyang Wang, Weichao Xu, Ye Yuan, Wenshan Cai, Shining Zhu, and Jia Zhu. 3D self-assembly of aluminium nanoparticles for plasmon-enhanced solar desalination.* Nature Photonics, *10(6):393–398, 2016.*

[116] *Lin Zhou, Yingling Tan, Dengxin Ji, Bin Zhu, Pei Zhang, Jun Xu, Qiaoqiang Gan, Zongfu Yu, and Jia Zhu. Self-assembly of highly efficient, broadband plasmonic absorbers for solar steam generation.* Science advances, *2(4):e1501227, 2016.*

[117] *Oara Neumann, Alexander S. Urban, Jared Day, Surbhi Lal, Peter Nordlander, and Naomi J. Halas. Solar vapor generation enabled by nanoparticles.* ACS nano, *7(1):42–49, 2013.*

[118] *Hao Wang, Vijay Prasad Sivan, Arnan Mitchell, Gary Rosengarten, Patrick Phelan, and Liping Wang. Highly efficient selective metamaterial absorber for high-temperature solar thermal energy harvesting.* Solar Energy Materials and Solar Cells, *137:235–242, 2015.*

[119] *Sunwoo Han, Ju-Hyeon Shin, Pil-Hoon Jung, Heon Lee, and Bong Jae Lee. Broadband solar thermal absorber based on optical metamaterials for high-temperature applications.* Advanced Optical Materials, *4(8):1265–1273, 2016.*

[120] *Eva Céspedes, Men Wirz, J. A. Sánchez-García, Laura Alvarez-Fraga, R. Escobar-Galindo, and C. Prieto. Novel Mo–Si3N4 based selective coating for high temperature concentrating solar power applications.* Solar energy materials and solar cells, *122:217–225, 2014.*

[121] *Chenglong Wan, Yinglung Ho, S. Nunez-Sanchez, Lifeng Chen, Martin Lopez-Garcia, Jon Pugh, Bofeng Zhu, P. Selvaraj, T. Mallick, S. Senthilarasu, et al. A selective metasurface absorber with an amorphous carbon interlayer for solar thermal applications.* Nano Energy, *26:392–397, 2016.*

[122] *Wei Li, Urcan Guler, Nathaniel Kinsey, Gururaj V. Naik, Alexandra Boltasseva, Jianguo Guan, Vladimir M. Shalaev, and Alexander V. Kildishev. Refractory plasmonics with titanium nitride: broadband metamaterial absorber.* Advanced Materials, *26(47):7959–7965, 2014.*

[123] *Pengfei Li, Baoan Liu, Yizhou Ni, Kaiyang Kevin Liew, Jeff Sze, Shuo Chen, and Sheng Shen. Large-Scale Nanophotonic Solar Selective Absorbers for High-Efficiency Solar Thermal Energy Conversion.* Advanced Materials, *27(31):4585–4591, jul 2015.*

[124] *Hao Wang and Liping Wang. Perfect selective metamaterial solar absorbers.* Optics Express, *21(S6):A1078, nov 2013.*

[125] *Feng Cao, Kenneth McEnaney, Gang Chen, and Zhifeng Ren. A review of cermet-based spectrally selective solar absorbers.* Energy & Environmental Science, *7(5):1615–1627, 2014.*

[126] *Ping Song, Yongxin Wu, Lei Wang, Ying Sun, Yuping Ning, Yilin Zhang, Beibei Dai, Eric Tomasella, Angélique Bousquet, and Cong Wang. The investigation of*

thermal stability of Al/NbMoN/NbMoON/SiO2 solar selective absorbing coating. Solar Energy Materials and Solar Cells, *171:253–257, 2017.*

[127] John B. Pendry, David Schurig, and David R. Smith. Controlling electromagnetic fields. science, *312(5781):1780–1782, 2006.*

[128] Naomi J. Halas, Surbhi Lal, Wei-Shun Chang, Stephan Link, and Peter Nordlander. Plasmons in strongly coupled metallic nanostructures. Chemical reviews, *111(6):3913–3961, 2011.*

[129] Craig F. Bohren and Donald R. Huffman. Absorption and Scattering of Light by Small Particles. *Wiley, apr 1998.*

[130] Stefan A. Maier et al. Plasmonics: fundamentals and applications, *volume 1. Springer, 2007.*

[131] XianGang Luo. Principles of electromagnetic waves in metasurfaces. Science China Physics, Mechanics & Astronomy, *58(9):1–18, 2015.*

[132] Haofei Shi, Changtao Wang, Chunlei Du, Xiangang Luo, Xiaochun Dong, and Hongtao Gao. Beam manipulating by metallic nano-slits with variant widths. Optics express, *13(18):6815–6820, 2005.*

[133] David F. P. Pile, Takeshi Ogawa, Dmitri K. Gramotnev, Y. Matsuzaki, Kristy C. Vernon, K. Yamaguchi, Toshihiro Okamoto, Masanobu Haraguchi, and Masuo Fukui. Two-dimensionally localized modes of a nanoscale gap plasmon waveguide. Applied Physics Letters, *87(26):261114, 2005.*

[134] C. F. Bohren and D. R. Huffman. Absorption and Scattering of Light by Small Particles (Wiley-Interscience, New York) . 1983.

[135] Traci R. Jensen, Michelle L. Duval, K. Lance Kelly, Anne A. Lazarides, George C. Schatz, and Richard P. Van Duyne. Nanosphere lithography: effect of the external dielectric medium on the surface plasmon resonance spectrum of a periodic array of silver nanoparticles. The Journal of Physical Chemistry B, *103(45):9846–9853, 1999.*

[136] Yang Li, Dezhao Li, Cheng Chi, and Baoling Huang. Achieving strong field enhancement and light absorption simultaneously with plasmonic nanoantennas exploiting film-coupled triangular nanodisks. The Journal of Physical Chemistry C, *121(30):16481–16490, 2017.*

[137] Benjamin J. Wiley, Sang Hyuk Im, Zhi-Yuan Li, Joeseph McLellan, Andrew Siekkinen, and Younan Xia. Maneuvering the surface plasmon resonance of silver nanostructures through shape-controlled synthesis, 2006.

[138] Yu Luo, Dang Yuan Lei, Stefan A. Maier, and J. B. Pendry. Broadband light harvesting nanostructures robust to edge bluntness. Physical review letters, *108(2):023901, 2012.*

[139] Alex Gansen. Multiscale Modelling of Anisotropic Composite Media for EMC Applicaions. *PhD thesis, Swansea University, 2017.*

[140] Koray Aydin, Zhaofeng Li, M. Hudlička, S. A. Tretyakov, and Ekmel Ozbay. Transmission characteristics of bianisotropic metamaterials based on omega shaped metallic inclusions. New Journal of Physics, *9(9):326, 2007.*

[141] Koray Aydin, Zhaofeng Li, Serafettin Bilge, and Ekmel Ozbay. Experimental and numerical study of omega type bianisotropic metamaterials combined with a negative permittivity medium. Photonics and Nanostructures-Fundamentals and Applications, *6(1):116–121, 2008.*

[142] Moritz Striebel, JÓ§rg Wrachtrup, and Ilja Gerhardt. Absorption and Extinction Cross Sections and Photon Streamlines in the Optical Near-field. Scientific Reports, *7(1), nov 2017.*

[143] Urcan Guler, Alexandra Boltasseva, and Vladimir M. Shalaev. Refractory plasmonics. Science, *344(6181):263–264, 2014.*

[144] Urcan Guler, Alexander V. Kildishev, Alexandra Boltasseva, and Vladimir M. Shalaev. Plasmonics on the slope of enlightenment: the role of transition metal nitrides. Faraday discussions, *178:71–86, 2015.*

[145] Urcan Guler, Vladimir M. Shalaev, and Alexandra Boltasseva. Nanoparticle plasmonics: going practical with transition metal nitrides. Materials Today, *18(4):227–237, 2015.*

[146] Gururaj V. Naik, Jongbum Kim, and Alexandra Boltasseva. Oxides and nitrides as alternative plasmonic materials in the optical range. Optical materials express, *1(6):1090–1099, 2011.*

[147] P. Motamedi and K. Cadien. Structural and optical characterization of low-temperature ALD crystalline AlN. Journal of Crystal Growth, *421:45–52, 2015.*

[148] H. Jensen, G. N. Pedersen, G. Sørensen, et al. Effect of reactive gas mass flow on the composition and structure of AIN films deposited by reactive sputtering. Thin solid films, *230(2):121–127, 1993.*

[149] Sebastian Goerke, Mario Ziegler, Andreas Ihring, Jan Dellith, Andreas Undisz, Marco Diegel, Solveig Anders, Uwe Huebner, Markus Rettenmayr, and Hans-Georg Meyer. Atomic layer deposition of AlN for thin membranes using trimethylaluminum and H2/N2 plasma. Applied Surface Science, *338:35–41, 2015.*

[150] *Chih-Yuan Lin and Fu-Hsing Lu. Oxidation behavior of AlN films at high temperature under controlled atmosphere.* Journal of the European Ceramic Society, *28(3):691–698, 2008.*

[151] *F. Wang, Rongrong Zhang, X. Q. Xiu, D. Q. Lu, S. L. Gu, B. Shen, Y. Shi, and Y. D. Zheng. Study of dry oxidation of aluminum nitride on Si (111) substrate grown by metalorganic chemical vapor deposition.* Surface Review and Letters, *10(04):625–628, 2003.*

[152] *Sundar Kunwar, Mao Sui, Puran Pandey, Zenan Gu, Sanchaya Pandit, and Jihoon Lee. Improved configuration and LSPR response of platinum nanoparticles via enhanced solid state dewetting of In-Pt bilayers.* Scientific reports, *9(1):1–14, 2019.*

[153] *Igor Zoric, Michael Zach, Bengt Kasemo, and Christoph Langhammer. Gold, platinum, and aluminum nanodisk plasmons: material independence, subradiance, and damping mechanisms.* ACS nano, *5(4):2535–2546, 2011.*

[154] *Nikhil K. Ponon, Daniel J. R. Appleby, Erhan Arac, P. J. King, Srinivas Ganti, Kelvin S. K. Kwa, and Anthony O'Neill. Effect of deposition conditions and post deposition anneal on reactively sputtered titanium nitride thin films.* Thin Solid Films, *578:31–37, 2015.*

[155] *Tobias Krekeler, Surya S. Rout, Gnanavel V. Krishnamurthy, Michael Störmer, Mahima Arya, Ankita Ganguly, Duncan S. Sutherland, Sergey I. Bozhevolnyi, Martin Ritter, Kjeld Pedersen, et al. Unprecedented thermal stability of plasmonic titanium nitride films up to 1400Â° C.* Advanced Optical Materials, *9(16):2100323, 2021.*

[156] *Chunhong Gong, Jiwei Zhang, Chao Yan, Xiaoqiang Cheng, Jingwei Zhang, Laigui Yu, Zhensheng Jin, and Zhijun Zhang. Synthesis and microwave electromagnetic properties of nanosized titanium nitride.* Journal of Materials Chemistry, *22(8):3370–3376, 2012.*

[157] *W. Tsai, M. Delfino, J. A. Fair, and D. Hodul. Temperature dependence of the electrical resistivity of reactively sputtered TiN films.* Journal of applied physics, *73(9):4462–4467, 1993.*

[158] *S. Tripura Sundari, R. Ramaseshan, Feby Jose, S. Dash, and A. K. Tyagi. Investigation of temperature dependent dielectric constant of a sputtered TiN thin film by spectroscopic ellipsometry.* Journal of applied physics, *115(3):033516, 2014.*

[159] *V. Moraes, H. Riedl, R. Rachbauer, S. Kolozsvári, M. Ikeda, L. Prochaska, S. Paschen, and P. H. Mayrhofer. Thermal conductivity and mechanical properties of AlN-based thin films.* Journal of Applied Physics, *119(22):225304, 2016.*

[160] *Keltouma Aït Aïssa, Omar Elmazria, Pascal Boulet, Thierry Aubert, Ouadra Legrani, and Denis Mangin. Investigations of AlN thin film crystalline properties in a wide temperature range by in situ X-ray diffraction measurements: Correlation with AlN/Sapphire-based SAW structure performance.* IEEE Transactions on Ultrasonics, Ferroelectrics, and Frequency Control*, 62(7):1397–1402, 2015.*

[161] *F. Ansart, H. Ganda, R. Saporte, and J. P. Traverse. Study of the oxidation of aluminium nitride coatings at high temperature.* Thin Solid Films*, 260(1):38–46, 1995.*

[162] *C. Labatut, D. Kharchi, B. Aspar, F. Sibieude, and B. Armas. An in-situ study of the oxidation of AlN layers fabricated by LPCVD using X-ray diffraction.* Journal of the European Ceramic Society*, 13(4):339–344, 1994.*

[163] *M. Rauber, F. Muench, M. E. Toimil Molares, and W. Ensinger. Thermal stability of electrodeposited platinum nanowires and morphological transformations at elevated temperatures.* IOPScience*, 2012.*

[164] *Gesa Beck, Christoph Bachmann, Rita Bretzler, and Ralf Kmeth. Thermal stability of platinum, palladium and silver films on yttrium-stabilised zirconia.* Thin Solid Films*, 573:164–175, dec 2014.*

[165] *Zhehan Ying, Jiangyong Diao, Shi Wang, Xiangbin Cai, Yuan Cai, Hongyang Liu, and Ning Wang. Revealing high temperature stability of platinum nanocatalysts deposited on graphene oxide by in-situ TEM.* Materials Characterization*, 170:110706, dec 2020.*

[166] *Akbar Samadi, Henrik Klingberg, Liselotte Jauffred, Andreas Kjær, Poul Martin Bendix, and Lene B. Oddershede. Platinum nanoparticles: a non-toxic, effective and thermally stable alternative plasmonic material for cancer therapy and bioengineering.* Nanoscale*, 10(19):9097–9107, 2018.*

[167] *Alexander H. D. Cheng and Daisy T. Cheng. Heritage and early history of the boundary element method.* Engineering analysis with boundary elements*, 29(3):268–302, 2005.*

[168] *Richard Courant, Kurt Friedrichs, and Hans Lewy. Über die partiellen Differenzengleichungen der mathematischen Physik.* Mathematische annalen*, 100(1):32–74, 1928.*

[169] *von S. Gerschgorin. Fehlerabschätzung für das Differenzenverfahren zur Lösung partieller Differentialgleichungen.* ZAMM-Journal of Applied Mathematics and Mechanics/Zeitschrift für Angewandte Mathematik und Mechanik*, 10(4):373–382, 1930.*

[170] George G. O'Brien, Morton A. Hyman, and Sidney Kaplan. *A study of the numerical solution of partial differential equations.* Journal of Mathematics and Physics, *29(1-4):223–251, 1950.*

[171] Fritz John. *On integration of parabolic equations by difference methods.* Fritz John Collected Papers, *2:13, 1985.*

[172] Kane Yee. *Numerical solution of initial boundary value problems involving Maxwell's equations in isotropic media.* IEEE Transactions on antennas and propagation, *14(3):302–307, 1966.*

[173] Allen Taflove, Susan C. Hagness, and Melinda Piket-May. *Computational electromagnetics: the finite-difference time-domain method.* The Electrical Engineering Handbook, *3, 2005.*

[174] Niel K. Madsen and Richard W. Ziolkowski. *A three-dimensional modified finite volume technique for Maxwell's equations.* Electromagnetics, *10(1-2):147–161, 1990.*

[175] Vijaya Shankar, Alireza H. Mohammadian, and William F. Hall. *A time-domain, finite-volume treatment for the Maxwell equations.* Electromagnetics, *10(1-2):127–145, 1990.*

[176] Kane S. Yee and Jei S. Chen. *Conformal hybrid finite difference time domain and finite volume time domain.* IEEE transactions on antennas and propagation, *42(10):1450–1455, 1994.*

[177] Kane S. Yee and Jei S. Chen. *The finite-difference time-domain (FDTD) and the finite-volume time-domain (FVTD) methods in solving Maxwell's equations.* IEEE Transactions on Antennas and Propagation, *45(3):354–363, 1997.*

[178] Mohamed El Hachemi, Oubay Hassan, Kenneth Morgan, David Rowse, and Nigel Weatherill. *A low–order unstructured–mesh approach for computational electromagnetics in the time domain.* Philosophical Transactions of the Royal Society of London. Series A: Mathematical, Physical and Engineering Sciences, *362(1816):445–469, 2004.*

[179] Nigel P. Weatherill and Oubay Hassan. *Efficient three-dimensional Delaunay triangulation with automatic point creation and imposed boundary constraints.* International journal for numerical methods in engineering, *37(12):2005–2039, 1994.*

[180] Kenneth Morgan, Oubay Hassan, and Jaime Peraire. *An unstructured grid algorithm for the solution of Maxwell's equations in the time domain.* International journal for numerical methods in fluids, *19(9):849–863, 1994.*

[181] Yangwei Wu, Weifeng Zheng, Limei Lin, Yan Qu, and Fachun Lai. Colored solar selective absorbing coatings with metal Ti and dielectric AlN multilayer structure. Solar energy materials and solar cells*, 115:145–150, 2013.*

[182] Atasi Dan, Kamanio Chattopadhyay, Harish C. Barshilia, and Bikramjit Basu. Colored selective absorber coating with excellent durability. Thin Solid Films*, 620:17–22, 2016.*

[183] Er-Tao Hu, Shuai Guo, Tong Gu, Kai-Yan Zang, Hua-Tian Tu, Qing-Yuan Cai, Ke-Han Yu, Wei Wei, Yu-Xiang Zheng, Song-You Wang, et al. High efficient and wide-angle solar absorption with a multilayered metal-dielectric film structure. Vacuum*, 146:194–199, 2017.*

[184] Ming-Hui Liu, Er-Tao Hu, Yuan Yao, Kai-Yan Zang, Ning He, Jing Li, Yu-Xiang Zheng, Song-You Wang, Osamu Yoshie, YangPak Lee, et al. High efficiency of photon-to-heat conversion with a 6-layered metal/dielectric film structure in the 250-1200 nm wavelength region. Optics express*, 22(107):A1843–A1852, 2014.*

[185] L. E. R. Petersson and J. M. Jin. Analysis of Periodic Structures via a Time-Domain Finite-Element Formulation With a Floquet ABC. IEEE Transactions on Antennas and Propagation*, 54(3):933–944, mar 2006.*

[186] Surya Samukham, C. P. Vyasarayani, and Gangadharan Raju. Implicit Floquet analysis for parametric instabilities in a variable angle tow composite panel. Composite Structures*, 233:111637, feb 2020.*

[187] M. Bilokur, A. R. Gentle, M. D. Arnold, M. B. Cortie, and G. B. Smith. High temperature optically stable spectrally-selective Ti1xAlxN-based multilayer coating for concentrated solar thermal applications. Solar Energy Materials and Solar Cells*, 200:109964, sep 2019.*

[188] Miao Du, Xiaopeng Liu, Lei Hao, Xiaojing Wang, Jing Mi, Lijun Jiang, and Qinghe Yu. Microstructure and thermal stability of Al/Ti0.5Al0.5N/Ti0.25Al0.75N/AlN solar selective coating. Solar Energy Materials and Solar Cells*, 111:49–56, apr 2013.*

[189] Micheal Gozin. Development of Modified Titanium Nitride Nanoparticles asPotential Contrast Material for Photoacoustic Imaging. Technical report, 2014.

[190] Markus Bosund, Timo Sajavaara, Mikko Laitinen, Teppo Huhtio, Matti Putkonen, Veli-Matti Airaksinen, and Harri Lipsanen. Properties of AlN grown by plasma enhanced atomic layer deposition. Applied Surface Science*, 257(17):7827–7830, 2011.*

[191] Xinye Liu, Sasangan Ramanathan, Eddie Lee, and Thomas E. Seidel. Atomic layer deposition of aluminum nitride thin films from trimethyl aluminum (TMA) and ammonia. MRS Online Proceedings Library (OPL)*, 811, 2004.*

[192] *Ville Miikkulainen, Markku Leskelä, Mikko Ritala, and Riikka L. Puurunen. Crystallinity of inorganic films grown by atomic layer deposition: Overview and general trends.* Journal of Applied Physics, *113(2):2, 2013.*

[193] *S. C. Tjong and Haydn Chen. Nanocrystalline materials and coatings.* Materials Science and Engineering: R. Reports, *45(1-2):1–88, September 2004.*

[194] *Angelo Taglietti, Carla Renata Arciola, Agnese D'Agostino, Giacomo Dacarro, Lucio Montanaro, Davide Campoccia, Lucia Cucca, Marco Vercellino, Alessandro Poggi, Piersandro Pallavicini, et al. Antibiofilm activity of a monolayer of silver nanoparticles anchored to an amino-silanized glass surface.* Biomaterials, *35(6):1779–1788, 2014.*

[195] *Jacob Sagiv. Organized monolayers by adsorption. 1. Formation and structure of oleophobic mixed monolayers on solid surfaces.* J. Am. Chem. Soc., *102:92–98, January 1980.*

[196] *K. Bierbaum, M. Kinzler, C. Woll, M. Grunze, G. Hahner, S. Heid, and F. Effenberger.* Adhesion Science and Technology: Proceedings of the International Adhesion Symposium, Japan 1994 . *Gardon and Breach Science Publishers, 1995.*

[197] *Atul N. Parikh, David L. Allara, Issam Ben Azouz, and Francis Rondelez. An intrinsic relationship between molecular structure in self-assembled n-alkylsiloxane monolayers and deposition temperature.* The Journal of Physical Chemistry, *98(31):7577–7590, 1994.*

[198] *Tai Nguyen, Noureddine Adjeroud, Sebastjan Glinsek, Yves Fleming, Jérôme Guillot, Patrick Grysan, and Jérôme Polesel-Maris. A film-texture driven piezoelectricity of AlN thin films grown at low temperatures by plasma-enhanced atomic layer deposition.* APL Materials, *8(7):071101, 2020.*

[199] *B. Baur, G. Steinhoff, J. Hernando, O. Purrucker, M. Tanaka, B. Nickel, M. Stutzmann, and M. Eickhoff. Chemical functionalization of GaN and AlN surfaces.* Applied Physics Letters, *87(26):263901, 2005.*

[200] *P. H. Lissberger. Ellipsometry and polarised light.* Nature, *269(5625):270–270, sep 1977.*

[201] *R. Yusoh, M. Horprathum, P. Eiamchai, P. Chindaudom, and K. Aiempanakit. Determination of Optical and Physical Properties of ZrO2 Films by Spectroscopic Ellipsometry.* Procedia Engineering, *32:745–751, 2012.*

[202] *Brian L. Diffey. Sources and measurement of ultraviolet radiation.* Methods, *28(1):4–13, sep 2002.*

[203] R. Gampp, P. Oelhafen, P. Gantenbein, S. Brunold, and U. Frei. Accelerated aging tests of chromium containing amorphous hydrogenated carbon coatings for solar collectors. Solar Energy Materials and Solar Cells*, 54(1-4):369–377, jul 1998.*

[204] B. Carlsson, K. MÃ¶ller, M. KÃ¶hl, U. Frei, and S. Brunold. Qualification test procedure for solar absorber surface durability. Solar Energy Materials and Solar Cells*, 61(3):255–275, mar 2000.*

[205] B. Carlsson, K. MÃ¶ller, M. KÃ¶hl, M. Heck, S. Brunold, U. Frei, J.-C. Marechal, and G. Jorgensen. The applicability of accelerated life testing for assessment of service life of solar thermal components. Solar Energy Materials and Solar Cells*, 84(1-4):255–274, oct 2004.*

[206] M. KÃ¶hl, M. Heck, S. Brunold, U. Frei, B. Carlsson, and K. MÃ¶ller. Advanced procedure for the assessment of the lifetime of solar absorber coatings. Solar Energy Materials and Solar Cells*, 84(1-4):275–289, oct 2004.*

[207] 27.160 - Solar energy engineering, May 2014.

[208] Bo Carlsson, K. Moeller, Ulrich Frei, and Michael Koehl. &lttitle&gtAccelerated life testing of solar absorber coatings&lt/title&gt. In Volker Wittwer, Claes G. Granqvist, and Carl M. Lampert, editors, SPIE Proceedings*. SPIE, sep 1994.*

[209] H. M. Liao, R. N. S. Sodhi, and T. W. Coyle. Surface composition of AlN powders studied by x-ray photoelectron spectroscopy and bremsstrahlung-excited Auger electron spectroscopy. Journal of Vacuum Science &amp Technology A: Vacuum, Surfaces, and Films*, 11(5):2681–2686, sep 1993.*

[210] MANUEL GARCÍA MÉNDEZ, SANTOS MORALES RODRÍGUEZ, SADASIVAN SHAJI, BINDU KRISHNAN, and PASCUAL BARTOLO PÉREZ. STRUCTURAL PROPERTIES OF fontAlN/font FILMS WITH OXYGEN CONTENT DEPOSITED BY REACTIVE MAGNETRON SPUTTERING: XRD AND XPS CHARACTERIZATION. Surface Review and Letters*, 18(01n02):23–31, feb 2011.*

[211] Feby Jose, R. Ramaseshan, S. Dash, S. Bera, A. K. Tyagi, and Baldev Raj. Response of magnetron sputtered AlN films to controlled atmosphere annealing. Journal of Physics D: Applied Physics*, 43(7):075304, feb 2010.*

[212] Yongheng Zhang. Characterization of as-received hydrophobic treated AlN powder using XPS. Journal of Materials Science Letters*, 21(20):1603–1605, 2002.*

[213] P. Motamedi and K. Cadien. XPS analysis of AlN thin films deposited by plasma enhanced atomic layer deposition. Applied Surface Science*, 315:104–109, oct 2014.*

[214] E. N. Kabachkov, E. N. Kurkin, N. N. Vershinin, I. L. Balikhin, V. I. Berestenko, A. Michtchenko, and Y. M. Shulga. Pt Supported on Plasma-Chemical Titanium Nitride for Efficient Room-Temperature CO Oxidation, 2019.

[215] Jung Bo Yoo, Hyo Jin Yoo, Hyuk Joon Jung, Han Sol Kim, Sora Bang, Jongmyung Choi, Hoyoung Suh, Ji-Hyun Lee, Jin-Gyu Kim, and Nam Hwi Hur. Titanium oxynitride microspheres with the rock-salt structure for use as visible-light photocatalysts. Journal of Materials Chemistry A*, 4(3):869–876, 2016.*

[216] Mustafa Alevli, Cagla Ozgit, Inci Donmez, and Necmi Biyikli. Structural properties of AlN films deposited by plasma-enhanced atomic layer deposition at different growth temperatures. physica status solidi (a)*, 209(2):266–271, nov 2011.*

[217] Oh Hyun Kim, Dojun Kim, and Tim Anderson. Atomic layer deposition of GaN using GaCl3 and NH3. Journal of Vacuum Science &amp Technology A: Vacuum, Surfaces, and Films*, 27(4):923–928, jul 2009.*

[218] Thermo Fisher Scientific Inc. https://www.jp.xpssimplified.com/elements/nitrogen.php, 2013.

[219] G. Ranga Rao and D. D. Sarma. SYSTEMATICS IN THE O 1s CORE-LEVEL SPECTRA IN TRANSITION METAL OXIDES, fontLaMO/fontsub3/sub (M = V, Cr, Mn, Fe, Co AND Ni). Modern Physics Letters B*, 04(04):277–282, feb 1990.*

[220] A. U. Alam, M. M. R. Howlader, and M. J. Deen. Oxygen Plasma and Humidity Dependent Surface Analysis of Silicon, Silicon Dioxide and Glass for Direct Wafer Bonding. ECS Journal of Solid State Science and Technology*, 2(12):P515–P523, 2013.*

[221] A. M. Nicolson and G. F. Ross. Measurement of the intrinsic properties of materials by time-domain techniques. IEEE Transactions on instrumentation and measurement*, 19(4):377–382, 1970.*

[222] William B. Weir. Automatic measurement of complex dielectric constant and permeability at microwave frequencies. Proceedings of the IEEE*, 62(1):33–36, 1974.*

[223] Kuek Chee Yaw. Measurement of dielectric material properties. Application Note. Rohde & Schwarz*, pages 1–35, 2012.*

[224] Vasundara V. Varadan and Ruyen Ro. Unique retrieval of complex permittivity and permeability of dispersive materials from reflection and transmitted fields by enforcing causality. IEEE transactions on Microwave Theory and Techniques*, 55(10):2224–2230, 2007.*

[225] Chandra R. Bhat. Simulation estimation of mixed discrete choice models using randomized and scrambled Halton sequences. Transportation Research Part B: Methodological*, 37(9):837–855, nov 2003.*

Annex

Retrieval of optical constants from S-Parameters *The equations used for the retrieval of optical parameters from* $[S_{ij}]$ *are described below. We assume a reverse media where* $[S_{ij}]$=$[S_{11}, S_{21}]$.

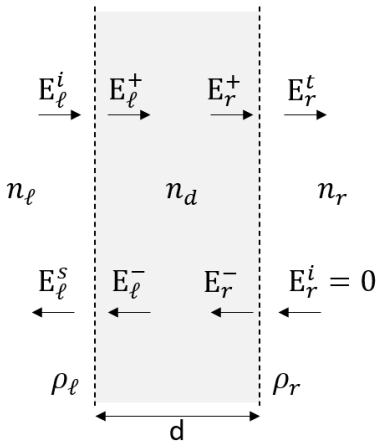

Figure 6.1: Sketch showing the electric fields components of wave propagating from left to right passing through the dielectric slab of thickness d.

The Figure 6.1 shows field components propagating from left to right through the dielectric slab . Subscript "ℓ" denotes left, while "r" denotes right superscript "i, s, t," denotes respectively incident, scattered and transmitted, while "+, -" are respectively the forward propagating and backward propagating components inside the dielectric. ρ_ℓ *and* ρ_r *are the elementary reflection coefficients respectively at the left and right interfaces. by considering* $\mathrm{n}_\ell = \mathrm{n}_\mathrm{r} = \mathrm{n}$ *we have.*

$$\rho_\ell = -\rho_\mathrm{r} = \frac{\mathrm{n} - \mathrm{n}_\mathrm{d}}{\mathrm{n} + \mathrm{n}_\mathrm{d}} \tag{6.1}$$

The relationship between field component through the interfaces is handled in a straightforward way using the matching matrices in equations 6.2 6.4 and the propagation matrix in equation 6.3.

$$\begin{bmatrix} \mathrm{E}_\ell^\mathrm{i} \\ \mathrm{E}_\ell^\mathrm{s} \end{bmatrix} = \frac{1}{\rho_\ell + 1} \begin{bmatrix} 1 & \rho_\ell \\ \rho_\ell & 1 \end{bmatrix} \begin{bmatrix} \mathrm{E}_\ell^+ \\ \mathrm{E}_\ell^- \end{bmatrix} \tag{6.2}$$

$$\begin{bmatrix} \mathrm{E}_\ell^+ \\ \mathrm{E}_\ell^- \end{bmatrix} = \begin{bmatrix} \mathrm{e}^{\mathrm{j}\tilde{\mathrm{k}}\mathrm{d}} & 0 \\ 0 & \mathrm{e}^{-\mathrm{j}\tilde{\mathrm{k}}\mathrm{d}} \end{bmatrix} \begin{bmatrix} E_\mathrm{r}^+ \\ E_\mathrm{r}^- \end{bmatrix} \tag{6.3}$$

$$\begin{bmatrix} \mathrm{E}_\mathrm{r}^+ \\ \mathrm{E}_\mathrm{r}^- \end{bmatrix} = \frac{1}{\rho_\mathrm{r} + 1} \begin{bmatrix} 1 & \rho_\mathrm{r} \\ \rho_\mathrm{r} & 1 \end{bmatrix} \begin{bmatrix} \mathrm{E}_\mathrm{r}^\mathrm{t} \\ 0 \end{bmatrix} \tag{6.4}$$

From the previous equations we workout the relationship between left and right components as:

$$\mathrm{E}_{\ell}^{\mathrm{i}} = \frac{1}{(\rho_{\ell}+1)(\rho_{\ell}+1)} \left(\mathrm{e}^{\mathrm{j}\tilde{\mathrm{k}}\mathrm{d}} + \rho_{\ell}\rho_{\mathrm{r}}\mathrm{e}^{-\mathrm{j}\tilde{\mathrm{k}}\mathrm{d}}\right) \mathrm{E}_{\mathrm{r}}^{\mathrm{t}} \tag{6.5}$$

$$\mathrm{E}_{\ell}^{\mathrm{s}} = \frac{1}{(\rho_{\ell}+1)(\rho_{\ell}+1)} \left(\rho_{\ell}\mathrm{e}^{\mathrm{j}\tilde{\mathrm{k}}\mathrm{d}} + \rho_{\mathrm{r}}\mathrm{e}^{-\mathrm{j}\tilde{\mathrm{k}}\mathrm{d}}\right) \mathrm{E}_{\mathrm{r}}^{\mathrm{t}} \tag{6.6}$$

This leads to determine the scattering parameters as:

$$\mathrm{S}_{11} = \frac{\mathrm{E}_{\ell}^{\mathrm{r}}}{\mathrm{E}_{\ell}^{\mathrm{i}}} = \frac{\rho_{\ell} + \rho_{\mathrm{r}}\mathrm{e}^{-\mathrm{j}2\tilde{\mathrm{k}}\mathrm{d}}}{1 + \rho_{\mathrm{r}}\rho_{\ell}\mathrm{e}^{-\mathrm{j}2\tilde{\mathrm{k}}\mathrm{d}}} \tag{6.7}$$

$$\mathrm{S}_{21} = \frac{\mathrm{E}_{\mathrm{r}}^{\mathrm{t}}}{\mathrm{E}_{\ell}^{\mathrm{i}}} = \frac{(1+\rho_{\ell})\,(1+\rho_{\mathrm{r}})\,\mathrm{e}^{-\mathrm{j}\tilde{\mathrm{k}}\mathrm{d}}}{1 + \rho_{\mathrm{r}}\rho_{\ell}\mathrm{e}^{-\mathrm{j}2\tilde{\mathrm{k}}\mathrm{d}}} \tag{6.8}$$

if we set the media on left is the same as the right:

$$\phi = \mathrm{e}^{-\mathrm{j}\tilde{\mathrm{k}}\mathrm{d}}\ ,\ \rho_{\ell} = -\rho_{\mathrm{r}} = \rho \tag{6.9}$$

we derive quantities Γand ρ as:

$$\rho = \zeta + \sqrt{\zeta^2 - 1}\ ,\ \zeta = \frac{\mathrm{S}_{11}^2 - \mathrm{S}_{21}^2 + 1}{2\mathrm{S}_{11}} \tag{6.10}$$

$$\Gamma = \frac{\mathrm{S}_{11} + \mathrm{S}_{21} - \rho}{1 - (\mathrm{S}_{11} + \mathrm{S}_{21})\rho} \tag{6.11}$$

finally we derive the complex refractive index of the slab:

$$\tilde{\mathrm{n}_{\mathrm{d}}} = \frac{2\pi\mathrm{m} - \phi}{\mathrm{k}_0\mathrm{d}} + \mathrm{j}\frac{\ln \mid \Gamma \mid}{\mathrm{k}_0\mathrm{d}} \tag{6.12}$$

the coefficient "m" in equation 6.12 is the branch order to unwrap the inverse tangent function.

Calculation of optical properties from S parameters using the python script Nicolson and Ross[221] in 1970 and Weir[222] in 1974 developed a method used for the extraction of dielectric properties for the material from S-parameters, called Nicholson-Ross-Weir (NRW) algorithm. Currently, a lot of varied methods are used to extract these material parameters, and an agreeable overview along with their examples and limitations is found in Rohde and Schwarz application note[223].

The phase shift function T and the interface reflection coefficient Γ are given by

$$\Gamma = \frac{(\eta - \eta_0)}{(\eta + \eta_0)} = \frac{\mathrm{z}_{\mathrm{in}} - 1}{\mathrm{z}_{\mathrm{in}} + 1} \tag{6.13}$$

$$\mathrm{T} = \mathrm{e}^{-\gamma\mathrm{d}} \tag{6.14}$$

where $\mathrm{z}_{\mathrm{in}} = \frac{\eta}{\eta_0}$ is the normalized characteristic impedance, $\eta = \sqrt{\mu/\epsilon}$ is the impedance

of the sample, $\eta_0 = \sqrt{\mu_0/\epsilon_0}$ is the free space impedance and γ is the propagation constant of the sample.

$$\gamma = \gamma_0\sqrt{\epsilon\mu} = \alpha + \mathrm{i}\beta \tag{6.15}$$

$$z_{in} = \sqrt{\frac{\mu_\mathrm{r}}{\epsilon_\mathrm{r}}} \tag{6.16}$$

where, $\gamma_0 = \mathrm{i}2\pi/\lambda_0 = \mathrm{i}\omega/\mathrm{c}_0$ is the propagation constant of the free space, λ_0 is the wavelength of the free space, ω is the angular frequency and $c_0$is the speed of light in free space. Also, α is the attenuation factor and β is the phase factor.

From equations 6.7 and 6.8, Γ is derived as

$$\Gamma = \mathrm{K} \pm \sqrt{\mathrm{K}^2 - 1} \tag{6.17}$$

where

$$K = \frac{\mathrm{S}_{11}^2 - \mathrm{S}_{21}^2 + 1}{2\mathrm{S}_{11}} \tag{6.18}$$

$$T = \frac{\mathrm{S}_{11} - \mathrm{S}_{21} + \Gamma}{1 - (\mathrm{S}_{11} + \mathrm{S}_{21})\,\Gamma} \tag{6.19}$$

Equation 6.17 chooses the plus or the minus sign such that $\mid \Gamma \mid < 1$.

Rewriting equation 6.14 generates

$$\gamma = \ln\left(\frac{1}{\mathrm{T}}\right)/\mathrm{d} \tag{6.20}$$

Bear in mind that T is a complex number, that leads to multiple values of γ , and can be written as

$$\mathrm{T} = \mid \mathrm{T} \mid \mathrm{e}^{\mathrm{i}\phi} \tag{6.21}$$

where ϕ is the phase that leads to

$$\gamma = \ln\left(\frac{1}{\mathrm{T}}\right)/\mathrm{d} + \mathrm{i}\left(\frac{2\pi\mathrm{m} - \phi}{\mathrm{d}}\right) \tag{6.22}$$

$$= -\frac{\ln(\mid \mathrm{T} \mid)}{\mathrm{d}} + \mathrm{i}\left(\frac{2\pi\mathrm{m} - \phi}{\mathrm{d}}\right) \tag{6.23}$$

$$= \alpha + i\beta \tag{6.24}$$

where $m = 0, \pm1, \pm2, ...$

This shows that in comparison to the real part of γ, the imaginary part does not have a single value.

Equations 6.13 and 6.16, leads to

$$\sqrt{\frac{\mu_r}{\epsilon_r}} = \frac{(1+\Gamma)}{(1-\Gamma)} \tag{6.25}$$

From equation 6.15 and 6.25 the following is obtained:

$$\epsilon_{\mathrm{r}} = \frac{\gamma}{\gamma_0}\left(\frac{1-\Gamma}{1+\Gamma}\right) = \frac{\gamma}{i\omega z_{\mathrm{in}}} \tag{6.26}$$

$$\mu_{\mathrm{r}} = \frac{\gamma}{\gamma_0}\left(\frac{1+\Gamma}{1-\Gamma}\right) = \frac{\gamma z_{\mathrm{in}}}{i\omega} \tag{6.27}$$

Due to numerous values of the imaginary parts of $\gamma, \epsilon_r$and $\mu_r$which are not unique, this becomes a problem for the thick samples.

Now, the phase constant β corresponds to the imaginary part of γ and

$$\beta = \frac{2\pi}{\lambda} \tag{6.28}$$

where $\lambda$is the wavelength of the sample material. From equation 6.22 and 6.28, we get

$$\frac{\mathrm{d}}{\lambda} = \mathrm{m} - \frac{\phi}{2\pi} \tag{6.29}$$

When m = 0 and $-2\pi < \phi < 0$,d/$\lambda$is between 0 to 1. If the thickness of the sample is smaller than λ, then the values of ϵ and μ are unique and correspond to m = 0. The vagueness for this method occurs if d > λ. To determine m in such cases, the solution can be obtained by applying Kramer-Kronig relations to the wavenumber[224].

Retrieval of the dimensions of Omega structure

- 360 snapshots also called training files are well dispersed in 5-dimentional space design. These snapshots were generated based on a method called Halton sequence[225] that occupies the whole design space.
- Second, a COMSOL simulation was run with unit cell of omega for each of the snapshot, completing a total of 360 snapshots.
- 5 values from each snapshot are calculated. These 5 values are not included in the 360 snapshots.
- Then scattering parameters S_{11} and S_{21} were calculated for all 360 snapshots.
- Proper Orthogonal Decomposition (POD) and Machine learning (ML) algorithm based on neural network (NN) was used to get the i.e, reduce order solution f, the error difference $|\ \mathrm{f} - \mathrm{f}^*\ |$is calculated to check the convergence. f^* is the full order numerical solution (x_1,x_2,x_3,x_4, x_5). The error for the each case is computed as

$$err = \left(\frac{\int_{0.25}^{2.5}(\mathrm{f}(\lambda) - \mathrm{f}^*(\lambda))^2 \mathrm{d}\lambda}{\int_{0.25}^{2.5}(\mathrm{f}^*(\lambda))^2 \mathrm{d}\lambda}\right) \tag{6.30}$$

where f denotes the reduced order approximation of the real and the imaginary part of one of the components of the S-parameters and f*denoted the full order solution.

POD results and influence of the number of training cases

nTr	err($R(S_{11})$)	err($T(S_{11})$)	err($R(S_{21})$)	err($T(S_{21})$)
45	0.1243	0.4587	0.1267	0.1697
90	0.1045	0.3087	0.1452	0.1195
180	0.0501	0.1672	0.0854	0.0867
360	0.0345	0.1068	0.0240	0.0247

Table 6.1: Maximum error of the POD predictions as a function of the number of training cases.

Predictions

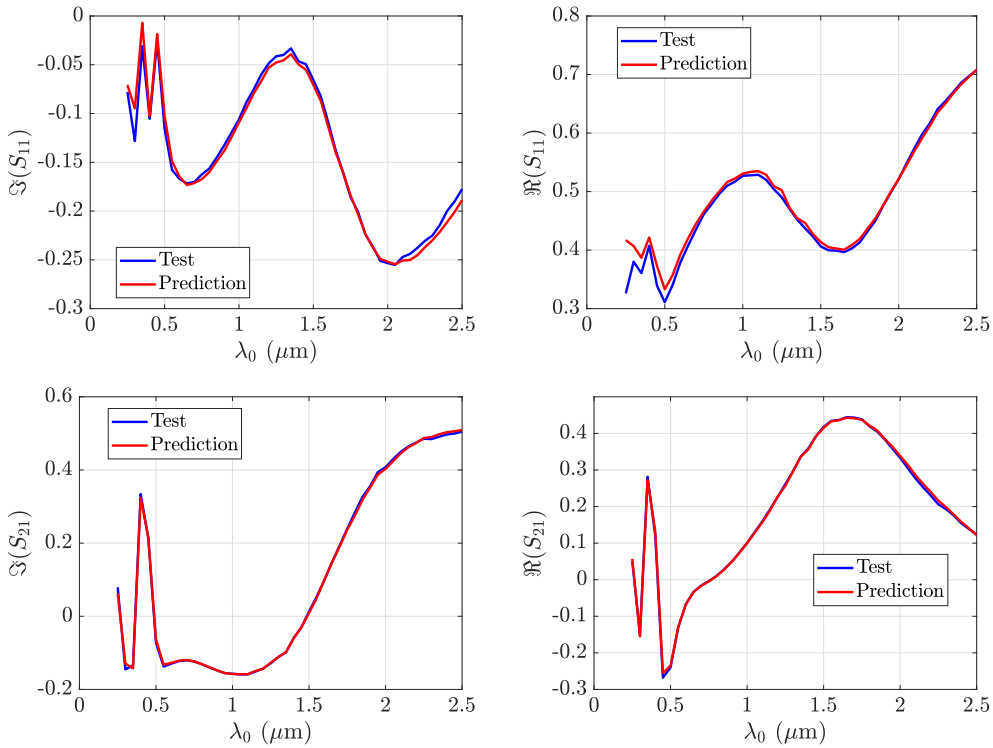

Figure 6.2: Comparison of the test and predicted results of one of the points chosen by POD.

NN results and influence of the number of training cases

nTr	err($R(S_{11})$)	err($T(S_{11})$)	err($R(S_{21})$)	err($T(S_{21})$)
45	0.0680	0.3146	0.0597	0.0963
90	0.0805	0.2992	0.0466	0.0509
180	0.0272	0.0984	0.0504	0.0393
360	0.0221	0.0531	0.0276	0.0187

Table 6.2: Maximum error of the NN predictions as a function of the number of training cases.

Predictions

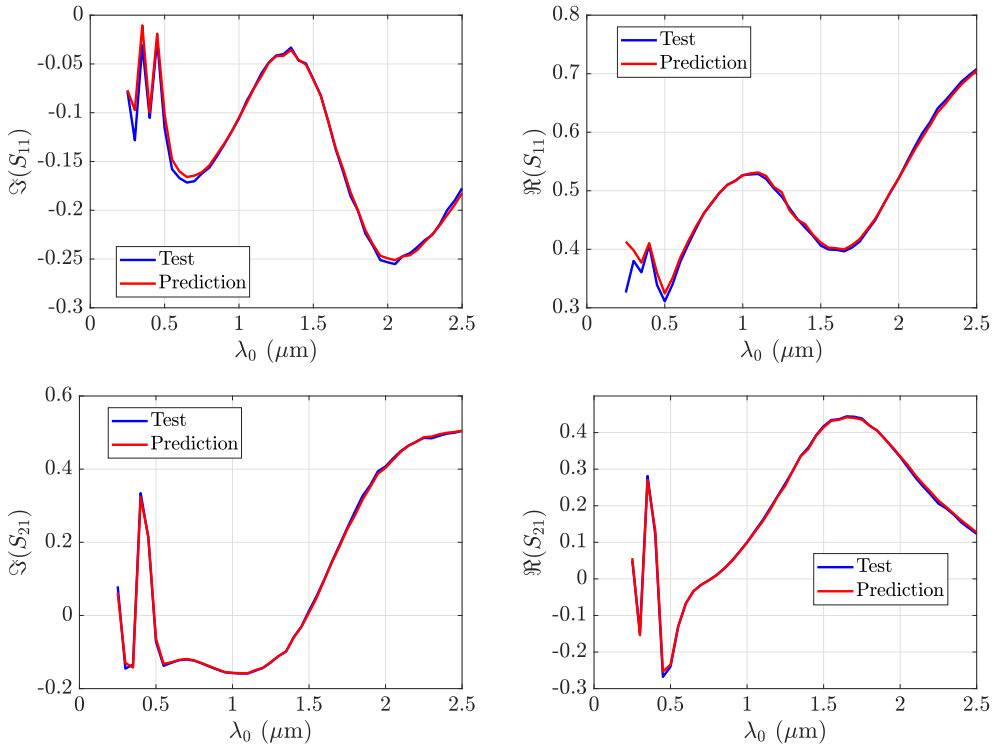

Figure 6.3: Comparison of the test and predicted results of one of the points chosen by NN.

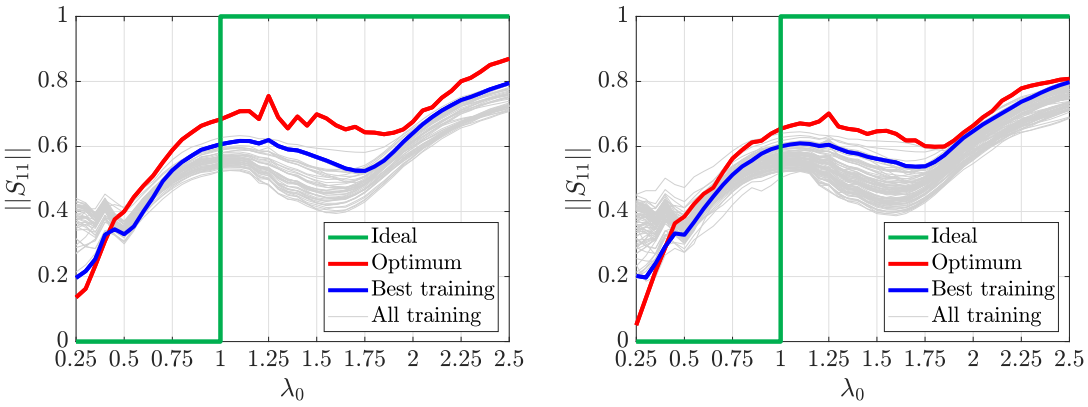

(a) nTr=45

(b) nTr=90

(c) nTr=180

(d) nTr=360

Figure 6.4: Results of the optimisation study with a single objective function using different number of training cases.